JETP Letters, Vol. 72, No. 4, 2000, pp. 157–159. Translated from Pis'ma v Zhurnal Éksperimental'noĭ i Teoreticheskoĭ Fiziki, Vol. 72, No. 4, 2000, pp. 229–232.

Anomalous Extensive Air Showers of Ultrahigh Energies and Their Arrival Directions

A. A. Mikhaĭlov and E. S. Nikiforova

Institute of Cosmophysical Research and Aeronomy, Yakut Research Center, Siberian Division, Russian Academy of Sciences, pr. Lenina 31, Yakutsk, 677891 Russia

Received July 4, 2000

Extensive air showers (EASs) of energy above 8×10^{18} eV observed from 1974 to 1995 on the Yakutsk EAS array are analyzed. Showers without muonic component are found. From the arrival directions of these showers, two clusters were found, one of which coincides, within the error bars, with a pulsar in the Milky Way Galaxy.

PACS numbers: 98.70.Sa; 95.85.Ry

Theoretical calculations [1] predict that primary cosmic γ rays produce anomalously small numbers of nuclear active particles and muons. At a γ-ray energy of 10^{15} eV, the expected flux density $\rho_\mu^\gamma(r)$ of muons with energies above 10 GeV at a distance of r from the shower axis is less than 1/30 of the muon flux densities $\rho_\mu^{Zp}(r)$ from the ordinary showers induced by nuclei and protons [2]; i.e.,

$$\rho_\mu^\gamma(r)/\rho_\mu^{Zp}(r) < 1/30.$$

The 6×10^{16} eV data from the EAS array of the Moscow State University indicated that the ratio of the number of γ-ray showers including an anomalously small muon content to the number of showers with normal muon content is less than 2×10^{-4} [3].

Analyzing the Yakutsk EAS data, we found showers, which we call anomalous showers, free of the muon components. Unfortunately, we have no information on whether or not they are produced by γ rays of extremely high energies. Having no clear notion of the origin of these showers, we decided to consider their distribution over the celestial sphere.

At present, the Yakutsk EAS array consists of 49 ground-based scintillation detectors with an area of 214 m^2 plus 5 underground muon detectors with an area of 100 m^2 and having the detection threshold $E > 1.0 \sec\theta$ GeV, where θ is the zenith angle of the shower arrival. The array is about 12 km^2.

In this study, the EASs detected on the Yakutsk EAS array from 1974 to 1995 were analyzed. We considered 596 showers of energies above 0.8×10^{19} eV with zenith angles <60° and the axes falling within the array perimeter. Twenty of these showers had energies $>4 \times 10^{19}$ eV. The energy and the arrival direction of a primary EAS-inducing particle were determined within an accuracy of ~30% and ~3%, respectively. The overall detection time interval was divided into individual time intervals of 6 h. Time intervals when the muon detectors were inoperative were excluded from the analysis. When the muon detectors were in operation, we selected the showers with zero muon component. For zero readings of the muon detectors, the probability that none of the particles fell within the detectors was estimated as $P = \Pi \exp(-\rho_i S_i)$, where ρ_i are the expected densities and S_i is the area of the ith detector. A shower for which this probability was $P > 10^{-4}$ was excluded from consideration. With such a procedure, 14 of the 596 showers were selected. Above the energy 4×10^{19} eV, there was no shower without muons. The number of anomalous showers was ~3% of the number of showers with normal muon content.

Time of arrival, energy, and coordinates of the showers forming doublets

Cluster no.	Date	Energy, E, eV	Declination and right ascension, deg		Galactic latitude and longitude, deg	
1	17.2.1981	7.7	63.7	30.6	2.2	131.1
1	25.12.1984	8.3	58.1	33.8	–2.6	134.3
2	17.5.1984	9.8	42.2	100.3	16.7	173.6
2	23.10.1986	18.6	45.0	101.5	18.5	171.3

0021-3640/00/7204-0157$20.00

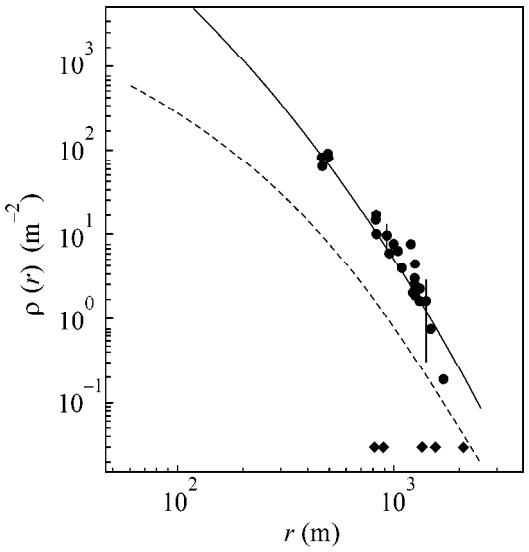

Fig. 1. The densities ρ(*r*) (circles, measured, and solid line, expected) of electron–photon and (rhombuses and dashed line) muonic components as functions of the distance from the shower axis. The muonic component is zero at all five points of muon observation.

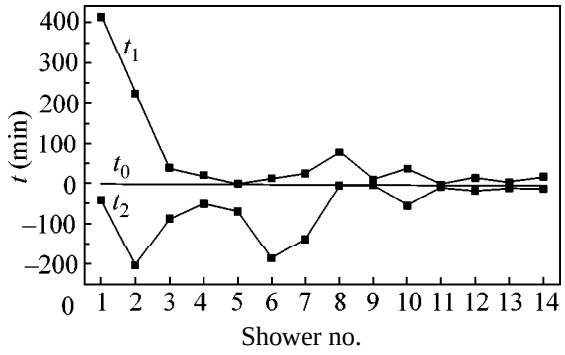

Fig. 2. Relative times (in min) of arrival of the showers involving muons: (t_1) before and (t_2) after the arrival time t_0 of a shower without muons.

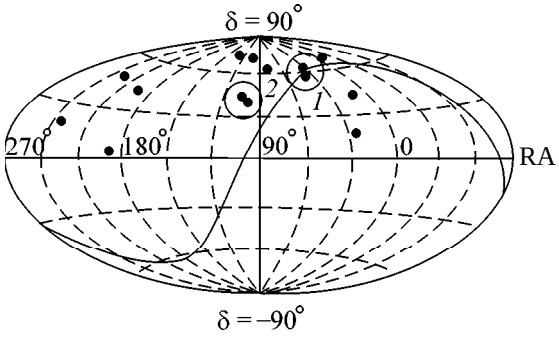

Fig. 3. The map (solid circles) of arrival directions of the anomalous showers in equatorial coordinates, inclination δ, and right ascension RA. The doublets *1* and *2* are shown by large circles.

For one of the 14 selected anomalous showers, Fig. 1 shows the observed densities of (circles) electron–photon and (rhombuses) muonic components as functions of the distance from the shower axis. The muonic component is zero at all five points of muon observation. The probability that none of the particles falls within the muon detectors is ~ 10^{-37}. The solid and dashed lines are the spatial distribution functions for the electron–photon and muonic components, respectively, for a given energy and arrival direction of the shower [4].

Figure 2 displays the relative times (in min) of arrival of the muon-involving showers arriving before and after the showers without muons. In particular, 8 min before the shower considered above and marked by number 13 in Fig. 2 (Fig. 1), a 2×10^{17} eV shower had arrived and one detector recorded muons; 9 min after the shower considered in Fig. 1, a 1.4×10^{18} eV shower arrived and three detectors recorded muons. These figures demonstrate that there are ultrahigh-energy showers without the muonic components.

Figure 3 shows (solid circles) a map of arrival directions for the anomalous showers in equatorial coordinates (declination δ and right ascension RA). Note that the Yakutsk EAS array observes only the north side, corresponding to the declinations $\delta > 2°$, of the celestial sphere. We did not find any correlation between the arrival directions of the 14 anomalous showers and pulsars [5]. However, two doublets are observed in the shower distributions (see Fig. 3 and table). The first doublet is located at a distance of less than 4° from the PSR 0154+61° pulsar. In the second doublet, the showers are spaced at 3°; the probability of two showers being accidentally placed at a distance of 1.5° from the point with coordinates $\delta = 43.5°$ and RA = 101° is $P \sim 10^{-5}$ for a uniform distribution of primary radiation. Such a low probability gives grounds to believe that the second doublet is also induced by a point pulsar source. It is likely that not all pulsars have been observed as yet. The probability of two showers being accidentally situated at a distance of 4° from the PSR 0154+61° pulsar is $P \sim 1.3 \times 10^{-3}$. The probability of a joint observation of two doublets—one within a range of 4° around the PSR 0154+61° pulsar and the other within the same range around the point with the coordinates $\delta = 43.5°$ and RA = 101° is $P \sim 6 \times 10^{-7}$. The first doublet is in the galactic plane and the second one, within a range of 20° from the galactic plane. This is likely due to the fact that the particles with energies below 4×10^{19} are of galactic origin [6].

Note that the flux of ordinary showers with energies ~10^{19} eV within the range $r < 6°$ around the direction of the above-indicated PSR 0154+61° pulsar exhibits a 3.5σ excess over that expected for isotropic distribution [6]. The characteristics of a pulsar PSR 0154+61°: distance 0.7 kpc, period 2.351653 sec, age 2×10^5 yr.

The flux of the anomalous showers from the PSR 0154+61° pulsar is ~10^{-19} cm^{-2} s^{-1}.

In summary, showers without muonic component >1 GeV were observed in the ultrahigh-energy range. The arrival directions of some showers are closely correlated: two doublets were found. The position of the two doublets at low galactic latitudes and correlation of one of them with a pulsar are likely due to the fact that cosmic rays with energies of up to 4×10^{19} eV are generated in pulsars [6].

This work was supported by the Russian Foundation for Basic Research, project no. 00-02-16325.

REFERENCES

1. R. Maze and A. Zawadski, Nuovo Cimento **17**, 625 (1960).
2. G. B. Khristiansen, G. V. Kulikov, and Yu. A. Fomin, *Ultrahigh-Energy Cosmic Radiation* (Atomizdat, Moscow, 1975).
3. V. I. Solov'eva, Dissertation (Institute of Physics, Academy of Sciences of USSR, 1965).
4. A. V. Glushkov, I. T. Makarov, E. S. Nikiforova, *et al.*, Astropart. Phys. **4**, 15 (1995).
5. A. G. Line and F. Graham-Smith, *Pulsar Astronomy* (Cambridge Univ. Press, Cambridge, 1990).
6. A. A. Mikhailov, in *Proceedings of the 26th International Cosmic Ray Conference, Salt Lake City, 1999*, Vol. 3, p. 268.

Translated by R. Tyapaev

JETP Letters, Vol. 72, No. 4, 2000, pp. 160–162. Translated from Pis'ma v Zhurnal Éksperimental'noĭ i Teoreticheskoĭ Fiziki, Vol. 72, No. 4, 2000, pp. 233–235.

Arrival Directions and Chemical Composition of Ultrahigh-Energy Cosmic Rays

A. A. Mikhaĭlov

Institute of Cosmophysical Research and Aeronomy, Yakut Research Center, Siberian Division, Russian Academy of Sciences, pr. Lenina 31, Yakutsk, 677891 Russia

e-mail: mikhailov@sci.yakutia.ru

Received July 4, 2000

Chemical composition of ultrahigh-energy cosmic rays is estimated through the reliably determined (both experimentally and theoretically) distribution of the number of showers in the galactic latitude. Experimental data at energies of ~10^{19} eV agree with the theoretical calculations, provided that cosmic rays involve predominantly heavy nuclei. An enhanced flux of cosmic rays from the galactic plane is detected at energies of ~10^{19} eV. © *2000 MAIK "Nauka/Interperiodica".*

PACS numbers: 98.70.Sa

Using model calculations of the *NN* and πN interactions at ultrahigh energies, the chemical composition was estimated through the depth of the maximum of the shower development from the data obtained on the Yakutsk array for extensive air showers (EASs) and indicated that protons dominate in the primary radiation at 10^{18}–10^{19} eV [1]. Similar estimations of the chemical composition from the Fly's Eye EAS array data [2] at an energy of ~10^{19} eV demonstrated that the fraction of protons is ~ 90%. Applying an upgraded model of the interaction of particles to an analysis of the maximum of shower development detected on the Fly's Eye array, Wolfendale and Wibig [3] concluded that cosmic rays with energies up to 3×10^{18} eV are composed of heavy nuclei and that the fraction of heavy nuclei is no less than 50% for energies above 3×10^{18} eV. Thus, these works exhibit contradictions in estimating the chemical composition of cosmic rays with ultrahigh energies through the maximum of shower development, because such an estimation requires the extrapolation of some characteristics of the *NN* and πN interactions from low to ultrahigh energies. In this study, the chemical composition of the cosmic rays are alternatively estimated through the observed and expected distributions of the numbers of showers in the galactic latitude.

As was shown in [4], cosmic rays of energies up to 4×10^{19} eV are most likely of galactic origin. For this reason, the arrival directions are analyzed for the $(0.8–4) \times 10^{19}$ eV EASs detected on the Yakutsk array during 1974–1995. Data are presented by the arrival directions of 576 showers with zenith angles <60° and axes falling within the array perimeter. The average energy of the showers is equal to 1.3×10^{19} eV.

The expected number of showers from a given galactic latitude is determined in the model calculations of particle paths in the assumed magnetic field of the Milky Way Galaxy.

This work uses a disk magnetic-field model proposed in [5] and based on the determination of the measure of Faraday rotation of the radio emissions from pulsars. The dominant component of the magnetic field is the azimuthal component with a magnitude of ~2 μG, while the radial and *z* components of the field are an order of magnitude smaller. Along with the regular component of the field, there is an irregular component with a magnitude from 0 to 5 μG and typical dimension of 100 pc. The direction of the irregular component is distributed randomly. The radius and half-height of the disk are 15 and 0.4 kpc, respectively.

As in [6], the existence of an extensive magnetic field beyond the disk, in the galactic halo, is assumed. This field has both regular and irregular components. The basic azimuthal regular component of the magnetic field in the galactic halo is $\sim 1 \exp(|z| - 0.4)/5$ kpc)] μG. The irregular component has a magnitude from 0 to 1.5 μG and a characteristic size of 500 pc. Its direction is also distributed randomly. The radius and half-height of the halo are 15 and 5 kpc, respectively.

The following two cases of the distribution of cosmic-ray sources are considered: (i) the sources are distributed uniformly over the entire disk and (ii) the sources are pulsars in the disk (as was shown in [7] and in other works, cosmic rays most likely originate from pulsars). The distribution of pulsars over the radius *r* and height *z* of the galactic disk is described by the function

$$f(r, z) = f_1(r) f_2(z),$$

0021-3640/00/7204-0160$20.00

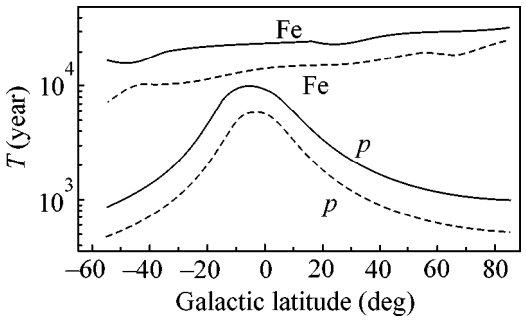

Fig. 1. The length of paths (the expected intensity) of (*p*) protons and (Fe) iron nuclei with energies 1.3×10^{19} eV in the galactic disk. The solid lines correspond to the sources uniformly distributed over the entire disk, and the dashed lines are for the pulsar sources.

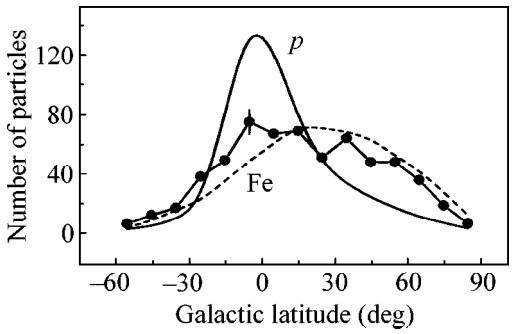

Fig. 2. The galactic-latitude dependence of the numbers of showers: (circles connected by the line) observed and expected from (solid curve) protons and (dashed curve) iron nuclei.

where $f_1(r) = (1 - \exp(r^2/8))\exp(-r^2/100)$ and $f_2(z) = 1/0.46\exp(-|z|/0.23)$. The function $f_1(r)$ is found by approximating the observed pulsar distribution over the radius r [8] while the function $f_2(z)$ is taken from [8].

In the above model of the galactic magnetic field, the expected numbers of showers from a given galactic latitude are determined through calculating the antiparticle paths from the Earth. The antiparticle paths are calculated up to their exit beyond the halo and correspond to the paths of positively charged particles from the sources. The flux of expected particles in a given direction is proportional to the path length of the antiparticles in the source region and to the density of the sources. The paths of antiparticles, i.e., antiprotons, are considered for energies 5×10^{17} and 1.3×10^{19} eV. Antiproton energies of 1.3×10^{19} and 5×10^{17} eV correspond to the average energy of the showers under consideration and to the generation of showers by proton and iron nuclei, respectively.

The lengths of the particle paths in the galactic disk or the expected intensities of the particles are plotted in Fig. 1 as functions of the galactic latitude *b*. The solid line displays the lengths of the particle paths for the case where the cosmic-ray sources are distributed over the entire disk, and the dashed line corresponds to the case of pulsar sources. Independently of the assumed sources, the anisotropy is expected to be equal to 100% and a few percent for primary radiation consisting of protons and iron nuclei, respectively. Note that a similar conclusion was obtained in [9] for other models of the galactic magnetic field. An increase in the halo dimension up to 30–100 kpc with a field magnitude of ~1 μG virtually does not change the results [10, 11].

The observed distribution of the showers in the galactic latitude *b* is obtained from the data from the Yakutsk EAS array and is plotted in Fig. 2 along with the expected number of showers from primary radiation consisting of (*p*) protons and (Fe) iron nuclei. The expected number of showers is obtained from the expected intensity (Fig. 1), taking into account the exposure of the Yakutsk EAS array on the celestial sphere, and is normalized to the observed number of showers. After normalization, the expected number of showers from both protons and iron nuclei coincide with each other for both cases of the source distribution. A comparison of the observed and expected distributions of showers in the galactic latitude using the χ^2 method indicates that the fraction of iron nuclei in the primary radiation at 10^{19} eV should be no less than 80%.

Note that the above-considered showers exhibit an enhanced flux of particles from the galactic plane at latitudes $|b| < 3°$: 59 showers are observed, compared to 34.4 expected in the case of the isotropic primary radiation; i.e., the observed number exceeds the expected number by 4.2σ. This enhanced flux of particles with energies of $\sim 10^{19}$ eV is apparently related to the fact that cosmic rays with energies of up to 4×10^{19} eV are most likely of galactic origin and are generated in pulsars [7]. The estimation of the chemical composition of the primary radiation through the arrival direction of showers demonstrates that cosmic rays at an energy of $\sim 10^{19}$ eV consist predominantly of iron nuclei whose fraction is ≥80%.

This work was supported by the Russian Foundation for Basic Research, project no. 00-02-16325.

REFERENCES

1. B. N. Afanasiev, M. N. Dyakonov, V. P. Egorova, *et al.*, in *Proceedings of the International Symposium "Extremely High Energy Cosmic Rays," Institute for Cosmic Ray Research, Tokyo, 1966*, p. 32.
2. D. J. Birg, S. C. Corbato, H. Y. Dai, *et al.*, Phys. Rev. Lett. **71**, 4301 (1993).
3. A. W. Wolfendale and T. Wibig, in *Proceedings of the 26th International Cosmic Ray Conference, Salt Lake City, 1999*, Vol. 3, p. 248.

4. N. N. Efimov, A. A. Mikhailov, and A. D. Krasilnikov, in *Proceedings of the 21st International Cosmic Ray Conference, Adelaide, 1990*, Vol. 2, p. 64.

5. R. J. Rand and S. R. Kulkarni, Astrophys. J. **343**, 760 (1989).

6. V. S. Berezinsky, A. A. Mikhailov, and S. I. Syrovatskii, in *Proceedings of the 16th International Cosmic Ray Conference, Kyoto, 1979*, Vol. 2, p. 86.

7. A. A. Mikhailov, in *Proceedings of the 26th International Cosmic Ray Conference, Salt Lake City, 1999*, Vol. 3, p. 268.

8. R. Manchester and J. Taylor, *Pulsar* (Freeman, San Francisco, 1977).

9. M. Giller, J. L. Osborne, J. Wdowczyk, and M. Zelinska, J. Phys. G: Nucl. Part. Phys. **20**, 1649 (1994).

10. V. S. Berezinsky, S. I. Grigoryeva, A. A. Mikhailov, *et al.*, in *Proceedings of the ICRR International Symposium, Kofu, 1991*, p. 134.

11. R. Lampard, R. W. R. Clay, B. R. Dawson, and A. G. Smith, in *Proceedings of the 25th International Cosmic Ray Conference, Durban, 1997*, Vol. 4, p. 193.

Translated by R. Tyapaev

JETP Letters, Vol. 72, No. 4, 2000, pp. 163–165. Translated from Pis'ma v Zhurnal Éksperimental'noĭ i Teoreticheskoĭ Fiziki, Vol. 72, No. 4, 2000, pp. 236–239.

Constraints on the Decay Period of a Free Neutron from the Characteristics of Tritium Beta Decay

Yu. A. Akulov* and B. A. Mamyrin

Ioffe Physicotechnical Institute, Russian Academy of Sciences, Politekhnicheskaya ul. 26, St. Petersburg, 194021 Russia

** e-mail: akulov.mass@pop.ioffe.rssi.ru*

Received July 10, 2000

The reduced decay period of the triton, $(ft_{1/2})_T$ = (1129.6 ± 3) s, and the free-neutron decay period, $(t_{1/2})_n$ = (616.7 ± 2.7 ± 1.3) s, are determined from the experimental and theoretical values of the chemical shifts of atomic and molecular tritium. © *2000 MAIK "Nauka/Interperiodica".*

PACS numbers: 13.30.Ce; 14.20.Dh; 23.40.-s

For mixed allowed beta transitions, including the decays of tritium nuclei and free neutrons, the decay period $(t_{1/2})_{T,n}$ corresponding to the direct production of continuum electrons is expressed in terms of the nuclear transition matrix elements as [1]

$$(t_{1/2})_{T,n} = \frac{K/G_V^2}{f_{T,n}(E_0)(|M_V|^2_{T,n} + |M_A|^2_{T,n}G_A^2/G_V^2)}. \quad (1)$$

Here, G_V and G_A are, respectively, the vector and the axial weak interaction constants; M_V and M_A are, respectively, the vector and axial matrix elements of the beta-decay Hamiltonian; K is a constant; $f(E_0)$ is the phase-space integral for a continuum beta electron; and E_0 is the edge energy of the beta spectrum (the subscripts T and n correspond to the transitions $T \longrightarrow {}^3\mathrm{He}$ and $n \longrightarrow p$, respectively).

The matrix elements $|M_V|_n$, $|M_V|_T$, and $|M_A|_n$ for the transitions within the isospin doublets $1/2^+ \longrightarrow 1/2^+$ are exactly known (1, 1, and $\sqrt{3}$, respectively [1]), while the axial matrix element for a relatively simple tritium nucleus can be calculated using different models of the nucleon wave functions and the intranuclear potential shape, allowing the neutron decay period to be derived from Eq. (1) using the data on triton beta decay. The main errors in this method of estimating $(t_{1/2})_n$ come from the variations in experimental values of the decay period in different tritium compositions because of the effect of electron surroundings of triton on the process of beta-electron formation. Three reaction channels are distinguished for beta decay in the tritium atomic and molecular systems: (i) the direct production of a continuum electron; (ii) the production of a continuum electron via replacing the orbital electrons by a beta electron; and (iii) decay into the bound states, i.e., the formation of a beta electron at one of the shells of a daughter atom. An appreciable fraction of beta electrons is produced with wavelengths typical of atomic electronic systems, because the energy released in triton beta decay is relatively small. This renders the final-state interaction of beta electrons with the orbital electrons and electron holes efficient, leading to deviations (called chemical shifts) of the experimental decay periods from the $(t_{1/2})_T$ value and making the calculation of the reduced triton decay period $(ft_{1/2})_T$ with an accuracy corresponding to the accuracy of the other parameters in Eq. (1) impossible without the introduction of corrections for the chemical shifts.

Intensive theoretical analyses of the atomic effects in the high-energy component of the tritium beta spectrum were particularly stimulated by interest in the problem of neutrino mass and gave, for a number of atomic and molecular systems T, T^-, T_2, CH_3T, etc. [2–5], beta-spectrum edge energy shifts ΔE_0 due to orbital rearrangement caused by the emission of beta electrons and a sudden increase in the nuclear charge. For a wide class of tritium compositions, this makes it possible to determine, through changing E_0 to $E_0 + \Delta E_0$ in the phase-space integral, the decay-rate variations induced by a change in the momentum phase-space domain available for beta electrons. At the same time, the effect of nucleus charge screening by orbital electrons, the exchange effect, and the effect of decay into bound states on the decay rate were analyzed only for triton decay in the tritium atom and in the T^+ and T^- ions, where the final-state electron ensemble has simple configurations: ns^1 in the ${}^3\mathrm{He}^+$ ion and $1s^2$, $2s^2$, ns^1ms^1 in the neutral helium atom. Therefore, a complete set of theoretical values for the chemical shifts of decay periods was obtained only for atomic ions and free tritium atoms. This means that the free-triton decay period in Eq. (1) can only be calculated using the experimentally determined decay period for atomic tritium.

A direct measurement of the decay period of atomic tritium requires solution of a complicated problem of stabilizing hydrogen atoms during time intervals

comparable with the decay period. This is also the reason that hinders the experimental determination of the decay periods for the T^+ and T^- ions. An alternative approach to the experimental determination of the beta-decay time characteristics in unstable atomic and molecular systems is to carry out experiments on measuring the difference in the decay rates of tritium nuclei in two compositions, for one of which the decay period can be measured. In [6], we reported the result of such an experiment, where the helium differential method [7] was used to obtain $\Delta t_{1/2} = (t_{1/2})_m - (t_{1/2})_a = (0.0316 \pm 0.0055)$ yr for the difference between the values for molecular and atomic tritium. A weighted average of two of the most recent and most consistent estimates [8, 9] for the decay period of molecular tritium is $\langle t_{1/2}\rangle_m = (12.296 \pm 0.017)$ yr, and, therefore, $(t_{1/2})_a = (12.264 \pm 0.018)$ yr. Since $(t_{1/2})_m$ and $\Delta t_{1/2}$ were determined by methods taking into account all beta-decay channels, the resulting $(t_{1/2})_a$ value corresponds to the total decay probability; i.e., it takes into account both the processes leading to the formation of continuum electrons and the decay into bound states. In this case, to determine $(t_{1/2})_T$, the $(t_{1/2})_a$ value should be corrected for decay into the bound states, for the excitation of an *s* electron in the $^3He^+$ ion (0.50%), for screening of the nuclear charge in the $^3He^+$ ion (–0.41%), and for the exchange effect (0.15%). It is appropriate to estimate the correction for decay into bound states at (0.62 ± 0.07)%, which is the average of the results obtained in [3, 10–12]; other corrections were theoretically obtained in [3]. The result is $(t_{1/2})_T = 12.264(1 + 0.0086) = (12.369 \pm 0.020)$ yr.

The mass difference (18529 ± 2) eV + m_ec^2 between the tritium and helium-3 nuclei was determined in [13] from the weighted mean of eleven independent measurements of the corresponding atomic mass difference. Taking into account the recoil energy (~3.4 eV) of the helium nucleus, we obtain a value of $E_0 = (18525.6 \pm 2)$ eV for the edge energy of the beta spectrum for the decay of a free triton. Calculating the phase-space integral by the method that takes into account the Coulomb interaction of a beta electron with a nucleus of finite dimension and mass, as well as the exchange of virtual photons between the charged particles involved in beta decay (within an accuracy of radiation corrections on the order of α^2) [14], we obtain from the above-mentioned E_0 value that $f_T = (2.894 \pm 0.006) \times 10^{-6}$ and, therefore, $(ft_{1/2})_T = (1129.6 \pm 3)$ s.

From the ratio in Eq. (1) for the neutron and triton with the above-mentioned values of the nuclear matrix elements, the decay period $(t_{1/2})_n$ is expressed as

$$(t_{1/2})_n = \frac{(ft_{1/2})_T(1 + |M_A|_T^2 G_A^2/G_V^2)}{f_n(1 + 3G_A^2/G_V^2)}. \qquad (2)$$

With allowance made for the proton recoil energy, the value $m_nc^2 - m_pc^2 = (782333 \pm 6)$ eV + m_ec^2 [15] for the energy of the $n \longrightarrow p$ transition corresponds to the value $E_0 = (781582 \pm 6)$ eV. In this case, the phase-space integral determined by the method developed in [16], with inclusion, as in the case of f_T, of radiative corrections on the order of α and the finite dimensions and mass of a nucleus, takes the value $f_n = 1.71487 \pm 0.00015$.

Substituting the $K/G_V^2 = (6137.2 \pm 3.6)$ s value determined from the data on eight purely Fermi transitions [17] into the numerator in Eq. (1) for triton, we find that $X = |M_A|_T^2 G_A^2/G_V^2 = 4.4331$. At the same time, using the values $G_A/G_V = -1.267 \pm 0.0035$ [18] and $|M_A|_T = \sqrt{3}\,(0.962 \pm 0.002)$ calculated in [19], where five modifications of the intranuclear potential were considered, we obtain $X = 4.4568$. With $\langle X\rangle = 4.445 \pm 0.012$ and the above values of $(ft_{1/2})_T$, f_n and G_A/G_V, Eq. (2) yields $(t_{1/2})_n = (616.7 \pm 2.7 \pm 1.3)$ s. Here, the first error term corresponds to the statistical error (1σ) determined by the experimental error of $(ft_{1/2})_T$ and the error of calculating $|M_A|_T$, and the second error term is the systematic error due to uncertainty of the $\langle X\rangle$ quantity.

The estimate made above for the decay period corresponds to the neutron mean lifetime $t_n = (889.7 \pm 3.9 \pm 1.9)$ s with respect to beta decay. This result agrees well with the estimates obtained for t_n from the measurement of the neutron lifetime by the method of determining the decay exponent for ultracold neutrons confined in a gravitational trap, $t_n = (888.4 \pm 3.1 \pm 1.1)$ s [20], and by the method of counting decay events in a calibrated neutron beam, $t_n = (889.2 \pm 3.0 \pm 3.8)$ s [21]. This agreement indicates that the method reported in this work for estimating the neutron decay period is adequate and can be used for matching a number of mutually related parameters characterizing beta processes.

This work was supported by the Russian Foundation for Basic Research (project no. 97-03-393665) and the State Science and Technology Program "Fundamental Metrology," project no. 4.06.

REFERENCES

1. R. J. Blin-Stoyle, *Fundamental Interactions and the Nucleus* (North-Holland, Amsterdam, 1973; Mir, Moscow, 1976).
2. E. G. Drukarev, Phys. Rev. C **54**, 3277 (1996).
3. M. R. Harston and N. C. Pyper, Phys. Rev. A **48**, 268 (1993).
4. P. Froelich, B. Jeziorski, W. Kolos, *et al.*, Phys. Rev. Lett. **71**, 2871 (1993).
5. I. G. Kaplan, G. V. Smelov, and V. N. Smutnyi, Phys. Lett. B **161**, 389 (1985).
6. Yu. A. Akulov and B. A. Mamyrin, Pis'ma Zh. Éksp. Teor. Fiz. **68**, 167 (1998) [JETP Lett. **68**, 175 (1998)].

7. Yu. A. Akulov, B. A. Mamyrin, and P. M. Shikhaliev, Pis'ma Zh. Tekh. Fiz. **19** (18), 72 (1993) [Tech. Phys. Lett. **19**, 594 (1993)].
8. Yu. A. Akulov, B. A. Mamyrin, L. V. Khabarin, *et al.*, Pis'ma Zh. Tekh. Fiz. **14**, 940 (1988) [Sov. Tech. Phys. Lett. **14**, 416 (1988)].
9. B. Budick, J. Chen, and H. Lin, Phys. Rev. Lett. **67**, 2630 (1991).
10. P. M. Sherk, Phys. Rev. **75**, 789 (1949).
11. J. N. Bahcall, Phys. Rev. **124**, 495 (1961).
12. V. N. Tikhonov and F. E. Chukreev, Vopr. At. Nauki Tekh., Ser.: At. Materialoved., No. 1 (4), 12 (1980).
13. B. Budick, J. Chen, and H. Lin, Phys. Rev. Lett. **67**, 2626 (1991).
14. D. H. Wilkinson and B. E. F. Macefield, Nucl. Phys. A **232**, 58 (1974).
15. P. J. Mohr and B. N. Taylor, J. Phys. Chem. Ref. Data **28**, 1713 (1999).
16. D. H. Wilkinson, Nucl. Phys. A **377**, 474 (1982).
17. A. Sirlin and R. Zucchini, Phys. Rev. Lett. **57**, 1994 (1986).
18. Particle Data Group (C. Caso *et al.*), Eur. Phys. J. C **3**, 1 (1998).
19. T.-Y. Saito, Y. Wu, S. Ishikawa, and T. Sasakawa, Phys. Lett. B **242**, 12 (1990).
20. V. P. Alfimenkov, V. V. Nesvizhevskiĭ, A. P. Serebrov, *et al.*, Zh. Éksp. Teor. Fiz. **102**, 740 (1992) [Sov. Phys. JETP **75**, 405 (1992)].
21. J. Byrne, Europhys. Lett. **33**, 187 (1996).

Translated by R. Tyapaev

JETP Letters, Vol. 72, No. 4, 2000, pp. 166–170. Translated from Pis'ma v Zhurnal Éksperimental'noĭ i Teoreticheskoĭ Fiziki, Vol. 72, No. 4, 2000, pp. 240–245.

Resonance Structures in the $\Lambda\bar{\Lambda}$ System

B. V. Bolonkin†*, A. P. Bugorskiĭ, V. V. Vladimirskiĭ*, V. K. Grigor'ev*, A. P. Grishin†*, O. N. Erofeeva*, Yu. V. Katinov*, I. Ya. Korol'kov**, V. I. Lisin*, V. N. Luzin*, V. N. Nozdrachev*, V. V. Sokolovskiĭ*, ***, G. D. Tikhomirov*, and Yu. P. Shkurenko***

** Institute of Theoretical and Experimental Physics, ul. Bol'shaya Cheremushkinskaya 25, Moscow, 117259 Russia*

*** Institute of High Energy Physics, Protvino, Moscow region, 142284 Russia*

**** e-mail: sokolovsky@vxitep.itep.ru*

Received July 18, 2000

The results of studying the $\Lambda\bar{\Lambda}$ system produced in the reaction $\pi^- p \longrightarrow \Lambda\bar{\Lambda} n$ at a π^--meson energy of 40 GeV are reported. Experimental data (~2300 events) were obtained on the ITEP 6-meter spectrometer with a beam of the IHEP U-70 accelerator. The invariant-mass spectra for the events dominated by the singlet or triplet $\Lambda\bar{\Lambda}$ states were found to differ considerably from each other. The data give evidence for the existence of resonance states of the $\Lambda\bar{\Lambda}$ system in the mass regions near 2.3, 2.5, and 2.8 GeV. © *2000 MAIK "Nauka/Interperiodica".*

PACS numbers: 14.20.Jn; 13.85.Ni

Interest in the investigation of baryon–antibaryon states is mainly caused by the fact that these states can be produced in the decay of usual mesons, thus providing a natural opportunity to study resonance states with very large masses. A number of broad resonances were found in the $\bar{p}p$ system [1] and in the $\Lambda\bar{p}(\bar{\Lambda}p)$ systems with strangeness [2, 3]. The $\Lambda\bar{\Lambda}$ system is also of interest because it may contain states with hidden strangeness, e.g., $s\bar{s}$ states of the ϕ- and f_2'-meson type.

The $\Lambda\bar{\Lambda}$ system was previously studied in [4–7]. In each experiment, no more than 100 events were detected, which gave no possibility of analyzing in detail the properties of the $\Lambda\bar{\Lambda}$ system. Our previous studies were carried out on ~300-event statistics and gave some evidence for the existence of a resonance structure in the $\Lambda\bar{\Lambda}$ system [8–11].

Recently, the $\Lambda\bar{\Lambda}$ system was studied with considerably larger statistics in the Z_0-boson decay and $\bar{p}p$ interactions [12, 13]. However, these works were devoted to studying the quantum and polarization characteristics of this system and gave no evidence of the resonance structures.

Experimental data were obtained on the ITEP 6-meter magnetic spark spectrometer [14] with a beam of 40-GeV ϕ-mesons from the IHEP U-70 accelerator. A system of trigger counters surrounding a liquid-hydrogen target allowed the detection of the processes accompanied by emission of neutral strange particles. The characteristics of the spectrometer and the results obtained for the K_SK_S system were reported in [15].

In this work, the production of pairs of Λ and $\bar{\Lambda}$ hyperons was analyzed on statistics of 2308 events detected in five exposures. These events are generated mainly in the "elastic" reaction

$$\pi^- p \longrightarrow \Lambda\bar{\Lambda} n, \quad \Lambda \longrightarrow p\pi^-, \quad \bar{\Lambda} \longrightarrow \bar{p}\pi^+. \qquad (1)$$

The contribution of the "inelastic" channel

$$\pi^- p \longrightarrow \Lambda\bar{\Lambda} X^0, \qquad (2)$$

where X^0 is a neutral system with zero strangeness and mass larger than the neutron mass, is ~30%. The experimental sensitivity was ~70 events/nb.

The events with hyperon production were identified on the basis of χ^2 values fitting the neutral V^0 events to the hypotheses of γ, K_S^0, Λ, and $\bar{\Lambda}$ particles. For the cases where χ^2 values for different hypotheses were close, we took into account, in addition to χ^2, the probability of a given decay length to occur and the *a priori* probabilities of the K_S and Λ ($\bar{\Lambda}$) fluxes (the cross section for the production of a pair of K_S mesons is approximately an order of magnitude greater than the cross section for the production of the $\Lambda\bar{\Lambda}$ system). The events were analyzed using standard selection criteria: minimum distance between the Λ and $\bar{\Lambda}$ paths; disposition of event vertices in the target region; track displacement; and the number of points in the tracks.

† Deceased.

0021-3640/00/7204-0166$20.00 © 2000 MAIK "Nauka/Interperiodica"

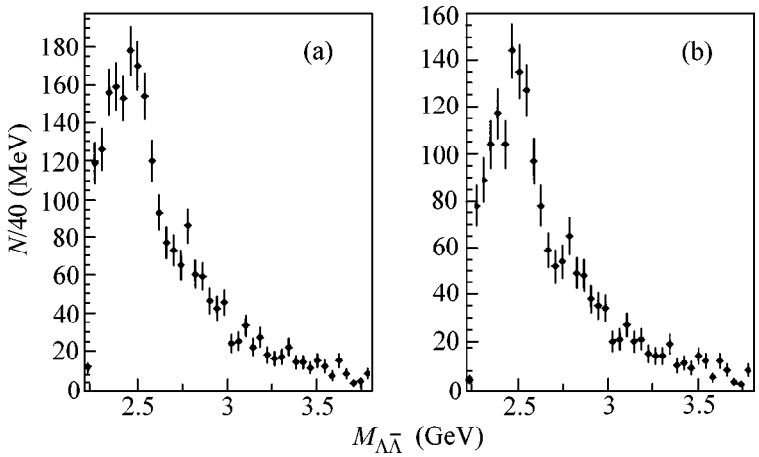

Fig. 1. Invariant-mass distributions for the $\Lambda\bar{\Lambda}$ events: (a) overall statistics and (b) events of reaction (1).

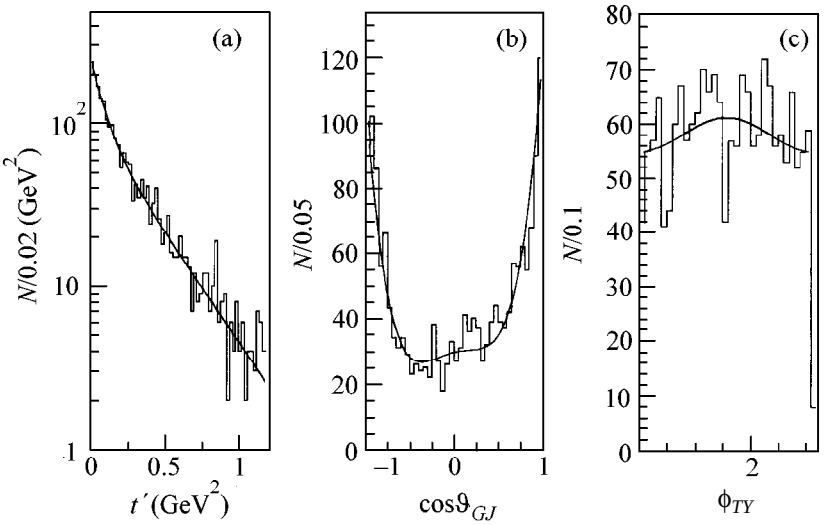

Fig. 2. Distributions of the $\Lambda\bar{\Lambda}$ events over (a) the transferred momentum t', (b) cosθ_{GJ}, and (c) azimuthal angle ϕ_{TY}. The lines are described in the text.

For some events, K_S and Λ were identified unambiguously, resulting in a background generated by pairs of K_S-mesons. To suppress this background, the invariant masses of both forks were calculated on the assumption that they decay into π-mesons. The events for which both masses fell within the K_S-meson mass range (497 ± 12 MeV) were rejected. As a result, $10 \pm 2\%$ of the events were lost. Nevertheless, the final samples of reactions (1) and (2) contained a $12 \pm 3\%$ background. This background was estimated from the number of $2V^0$ events fitted to the $\Lambda\Lambda$ and $\bar{\Lambda}\bar{\Lambda}$ pairs forbidden by the conservation laws in the experimental topology.

The geometric acceptance function of the spectrometer was calculated by the Monte Carlo method, taking into account the positions of the track detectors, target, scintillation counters of the trigger, and the magnetic field topography. The acceptance was found to be a smooth function and, for this reason, was not taken into account in further analysis.

Figure 1 shows the spectra of invariant masses of the $\Lambda\bar{\Lambda}$ system: (a) the total spectrum for reactions (1) and (2) and (b) the spectrum of the events selected for reaction (1). It is seen that the spectra differ only slightly from each other, so that all events were used in further analysis.

There is a sharp near-threshold rise which can be assigned to the resonances in this region and to the kinematic effect. A maximum at 2.5 GeV and a shoulder near 2.8 GeV may also be manifestations of the resonance structures. In our previous work [10], evidence was obtained for the existence of either resonances or sets of close resonances in these mass regions.

Table

$\Lambda\bar{\Lambda}$ mass range, GeV	t' region, GeV^2	K	ε	S
2.23–2.43	all t'	–1.62 ± 0.58	0.66 ± 0.15	0(1)
	<0.12	–0.02 ± 0.82		
	>0.12	–2.13 ± 0.79		
2.43–2.63	all t'	0.57 ± 0.51	0.11 ± 0.13	1(0)
	<0.12	0.33 ± 0.74		
	>0.12	0.88 ± 0.70		
2.63–2.91	all t'	1.06 ± 0.63	–0.02 ± 0.16	1
	<0.12	1.84 ± 0.90		
	>0.12	0.34 ± 0.88		
2.23–3.83	all t'	0.65 ± 0.30	0.09 ± 0.08	1(0)
	<0.12	0.88 ± 0.44		
	>0.12	0.45 ± 0.40		

Figure 2 demonstrates the distribution over the 4-momentum $t' = |t - t_{\min}|$ transferred from the incident pion to the system under study and the angular distributions for the overall spectrum of invariant masses of the $\Lambda\bar{\Lambda}$ system. The t' distribution (Fig. 2a) is approximated well by the sum of two exponential functions, $dN/dt' = a_1\exp(-b_1t') + a_2\exp(-b_2t')$, with $b_1 = 12.3 \pm 2.4$ GeV^{-2} and $b_2 = 3.11 \pm 0.24$ GeV^{-2}. This indicates that, in addition to a one-pion exchange (OPE), exchanges with other particles (B, a_1, a_2, ρ) take place. The distribution over the cosine of the Gottfried–Jackson angle $\cos\theta_{GJ}$ (Fig. 2b) is reproduced well by the S, P_0, and D_0 waves with SP_0 interference. Inclusion of additional amplitudes did not improve the description. However, the contribution of waves with higher angular momenta in some mass intervals was not improbable. The distribution in Fig. 2c in the Treiman–Yang angle ϕ_{TY} is virtually isotropic and satisfactorily described by the function $F(\phi) = a + b\cos2\phi$ with the normalized constants $a = 1.0 \pm 0.25$ and $b = 0.07 \pm 0.35$. This indicates that the contribution from the nonzero projection of orbital angular momentum to the total spectrum is negligible.

Quantum numbers of the $\Lambda\bar{\Lambda}$ system. The $\Lambda\bar{\Lambda}$ system consisting of a fermion and an antifermion has spin $S = 0$ or 1; total angular momentum $\mathbf{J} = \mathbf{S} + \mathbf{L}$, where $\mathbf{L}$ is the orbital angular momentum; isospin $I = 0$; and negative intrinsic parity. The spatial parity is determined as $P = -(-1)^L = (-1)^{L+1}$, the charge parity as $C = (-1)^{L+S}$, and the combined PC parity depends on the spin S of the $\Lambda\bar{\Lambda}$ system. The singlet ($S = 0$) and triplet ($S = 1$) states have, respectively, opposite and identical signs of the P and C parities.

Spin correlations. Weak decays $\Lambda \longrightarrow p\pi^-$ and $\bar{\Lambda} \longrightarrow \bar{p}\pi^+$ provide information on the polarization and spin state of the $\Lambda\bar{\Lambda}$ system. The spin of the system is characterized by the coefficient of correlation $K = [9/(\alpha_\Lambda\alpha_{\bar{\Lambda}})]\overline{\cos\theta_{p\bar{p}}}$, where $\alpha_\Lambda = 0.647$ ($\alpha_{\bar{\Lambda}} = -0.647$) is the asymmetry parameter for the decay of the Λ hyperon ($\bar{\Lambda}$); $\theta_{p\bar{p}}$ is the angle between the directions of a proton and an antiproton from the decays of Λ and $\bar{\Lambda}$ in their CM frame, respectively; and the averaging is performed over events. For the triplet $S = 1$ and singlet $S = 0$ states, $K = 1$ and –3, respectively [5, 16, 17].

To the make specific features of the mass spectrum more pronounced (Fig. 1), the events were selected according to the sign of the coefficient K and to the magnitude t' of transferred momentum. The table presents the weighted mean K values for various mass intervals of the $\Lambda\bar{\Lambda}$ system, without selection and with two selections for t'. The fraction $\varepsilon = (1 - K)/4$ of the singlet state is also given. Note that $\varepsilon = 0.25$ for a statistical mixture of the singlet and triplet states. The last column contains the preferable spin states of the $\Lambda\bar{\Lambda}$ system, as determined from the whole statistics in the indicated mass interval.

Near-threshold region. Figures 3a and 3b demonstrate that the difference between the spectra of $\Lambda\bar{\Lambda}$ masses with the selection of transferred momenta is most pronounced in the 2.23–2.43 GeV range. A maximum is almost absent for small transferred momenta; conversely, a distinct signal is observed in this mass range at $t' > 0.12$ GeV^2. The negative value of the coefficient K indicates that this resonance is predominantly in the singlet spin state with unnatural spin parity. However, this range may also include a triplet state.

A considerable difference between the spectra in Figs. 3a and 3b is evidenced by the Kolmogorov–Smirnov goodness-of-fit test, whose value (2.3–2.5) ×

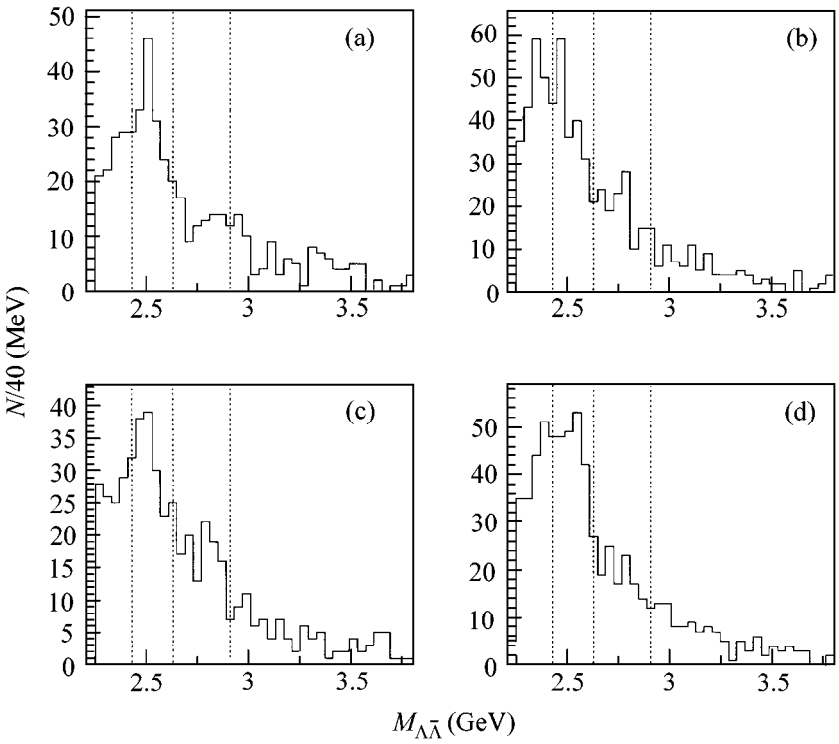

Fig. 3. Invariant-mass spectra for the $\Lambda\bar{\Lambda}$ events with various selection criteria for t' and the correlation coefficient K: (a) $t' < 0.12$ GeV^2 and $K < 0$, (b) $t' > 0.12$ GeV^2 and $K < 0$, (c) $t' < 0.12$ GeV^2 and $K > 0$, and (d) $t' > 0.12$ GeV^2 and $K > 0$. The vertical dashed lines indicate the limits of the invariant-mass ranges under consideration.

10^{-3} was determined for the mass spectrum range from the threshold to 3 GeV.

Region 2.43–2.63 GeV. Identification of the resonance features in this mass range of the $\Lambda\bar{\Lambda}$ system is not quite conclusive, because a maximum occurs in the range of small transferred momenta $t' < 0.12$ GeV^2 under the selections with correlation coefficients $K < 0$ and $K > 0$. A maximum in this mass range can be caused by the existence of a nonresonance phase space, together with one or two resonances differing in combined parity PC. This is also confirmed by the near-zero K value (table), which can be explained by a statistical mixture of the singlet and triplet states.

Region 2.63–2.91 GeV. The correlation coefficient K unambiguously points to the predominantly triplet $\Lambda\bar{\Lambda}$ state in this mass range. The plot in Fig. 3c exhibits the most pronounced maximum in the mass range near 2.8 GeV. In addition, this mass range is characterized by a strongly nonuniform distribution over the cosine of the Gottfried–Jackson angle, which can be attributed to the presence of waves with high orbital angular momenta. As to the distribution over the Treiman–Yang angle, it points to small values of the projection of orbital angular momentum in this mass range.

In conclusion, let us formulate the preliminary results of an analysis of the $\Lambda\bar{\Lambda}$ system.

The $\Lambda\bar{\Lambda}$ system is produced in the reaction $\pi^- p \longrightarrow \Lambda\bar{\Lambda} n$, predominantly in the triplet state. The singlet fraction, as determined for the entire mass spectrum, is 0.09 ± 0.08 (see table), in agreement with the CERN (LEAR) results [13], where the production of the $\Lambda\bar{\Lambda}$ system was examined in the $\bar{p}p$ interactions. The triplet states are mainly produced at $\Lambda\bar{\Lambda}$ masses above 2.4 GeV and at low transferred momenta $t' < 0.12$ GeV^2, which does not contradict the OPE dominance. In the near-threshold mass region, the $\Lambda\bar{\Lambda}$ system is predominantly produced in the singlet state; the singlet fraction here is 0.66 ± 0.15 and equals 0.78 ± 0.20 at $t' > 0.12$ GeV^2.

On the basis of the quantum characteristics of the $\Lambda\bar{\Lambda}$ system and regularities of its production, we gained evidence for the existence of resonance features in the invariant mass ranges near 2.3, 2.5, and 2.8 GeV.

Resonance meson states with masses above the threshold of production of the $\Lambda\bar{\Lambda}$ system were observed in some previous experiments. In particular, a

pseudoscalar resonance $\eta(2225)$ with a width of 150 MeV was observed in the $\phi\phi$ system produced in J/Ψ decay at the MARK III setup. The excess of the singlet $\Lambda\bar{\Lambda}$ state found in our analysis in the near-threshold region at high transferred momenta can be treated as a manifestation of the $\Lambda\bar{\Lambda}$ decay of this resonance or its analogue, the η' meson [production of the $0^+(0^{-+})$ states is allowed in the presence of the a_2 exchange]. The triplet component of the cross section in the near-threshold region is likely induced by the $f_2(2300)$ and $f_2(2340)$ resonances observed in the $\pi^- p \longrightarrow \phi\phi n$ reaction [19]. A maximum near 2.5 GeV can be attributed to $\Lambda\bar{\Lambda}$ decay of the $f_6(2510)$ resonance found in the $\pi^0\pi^0$ system [20]. The $\Lambda\bar{\Lambda}$ resonance states under study can also be treated as $s\bar{s}$ states belonging either to the leading ϕ–f_2' trajectory or to the daughter trajectories. An amplitude analysis of the $\Lambda\bar{\Lambda}$ system would clarify this situation, particularly as regards the discovery of resonance states with high (>6) angular momenta.

We are grateful to the staff of the ITEP 6-meter spectrometer and to the IHEP employees who provided the spectrometer operation in the beam from the U-70 accelerator.

This work was supported by the Russian Foundation for Basic Research, project no. 99-02-18540.

REFERENCES

1. M. Rozanska, W. Blum, H. Dietl, *et al.*, Nucl. Phys. B **162**, 505 (1980).
2. M. Baubillier, I. J. Bloodworth, G. J. Bossen, *et al.*, Nucl. Phys. B **183**, 1 (1981).
3. T. Armstrong, M. Baubillier, I. J. Bloodworth, *et al.*, Nucl. Phys. B **227**, 365 (1983).
4. W. Beusch, W. E. Fischer, M. Pepin, *et al.*, Phys. Lett. B **28**, 211 (1968).
5. W. E. Fischer, Nuovo Cimento A **62**, 17 (1969).
6. S. Lichtman, J. M. Bishop, N. N. Biswas, *et al.*, Nucl. Phys. B **105**, 229 (1976).
7. S. Anderson, Y. Kubota, M. Lattery, *et al.*, Preprint CLEO 96-19, 1997.
8. B. P. Barkov, B. V. Bolonkin, O. N. Baloshin, *et al.*, Yad. Fiz. **22**, 223 (1975) [Sov. J. Nucl. Phys. **22**, 113 (1975)].
9. O. N. Baloshin, B. P. Barkov, B. V. Bolonkin, *et al.*, Preprint No. 110, ITEF (Institute of Theoretical and Experimental Physics, Moscow, 1977).
10. O. N. Baloshin, B. P. Barkov, B. V. Bolonkin, *et al.*, Preprint No. 2, ITEF (Institute of Theoretical and Experimental Physics, Moscow, 1982).
11. B. V. Bolonkin, V. V. Vladimirskiĭ, Yu. P. Gorin, *et al.*, Preprint No. 149, ITEF (Institute of Theoretical and Experimental Physics, Moscow, 1989).
12. G. Alexander, J. Allison, N. Altekamp, *et al.*, Phys. Lett. B **384**, 377 (1996).
13. P. D. Barnes, G. Diebold, G. Franklin, *et al.*, Phys. Rev. C **54**, 1877 (1996).
14. B. V. Bolonkin, O. N. Baloshin, A. M. Blagorodov, *et al.*, Preprint No. 86, ITEF (Institute of Theoretical and Experimental Physics, Moscow, 1973).
15. B. V. Bolonkin, S. K. Bloschenko, V. V. Vladimirsky, *et al.*, Nucl. Phys. B **309**, 426 (1988).
16. F. Tabakin and R. A. Eisenstein, Phys. Rev. C **31**, 1857 (1985).
17. G. Alexander and H. G. Lipkin, Phys. Lett. B **352**, 162 (1995).
18. Z. Bai, G. T. Blaylock, T. Bolton, *et al.*, Phys. Rev. Lett. **65**, 1309 (1990).
19. A. Etkin, K. J. Foley, R. W. Hackenburg, *et al.*, Phys. Lett. B **201**, 568 (1988).
20. S. A. Sadovsky, Yad. Fiz. **57**, 1600 (1994) [Phys. At. Nucl. **57**, 1529 (1994)].

Translated by R. Tyapaev

JETP Letters, Vol. 72, No. 4, 2000, pp. 171–173. Translated from Pis'ma v Zhurnal Éksperimental'noĭ i Teoreticheskoĭ Fiziki, Vol. 72, No. 4, 2000, pp. 246–249.

Repopulation of Equidistant Levels by Two Coherent Resonant Phase-Shifted Electromagnetic Fields

D. F. Zaretskiĭ* and S. B. Sazonov

Russian Research Centre Kurchatov Institute, pl. Kurchatova 1, Moscow, 123182 Russia

** e-mail: zaretsky@imp.kiev.ru*

Received July 14, 2000

A new method of atomic and nuclear orientation and polarization is suggested. The method is based on the use of two coherent resonant phase-shifted monochromatic electromagnetic waves. It is demonstrated that a profound phase-shift-dependent level repopulation can be accomplished in a pulsed mode at room temperature. The possible application of this effect to quantum computers is briefly discussed. © *2000 MAIK "Nauka/Interperiodica".*

PACS numbers: 32.80.Bx; 71.70.Jp; 42.50.-p

At present, the methods of level repopulation induced in quantum systems by various electromagnetic waves are being extensively developed. These methods are suggested for use in solving numerous problems of applied quantum optics, e.g., the problem of lasing without inversion [1] or phase control of spontaneous emission [2], etc. These methods are usually associated with repopulation of the nonequidistant levels.

At the same time, the methods of atomic and nuclear polarization through optical pumping are well elaborated. However, the application of these methods is associated with a number of important restrictions: they are mainly used in the gas phase and imply relatively slow processes, for which the repopulation time is longer than the excited-state relaxation times; in addition, the atoms must possess electronic transitions in the optical range and, moreover, should not contain metastable states. To overcome these restrictions, we suggested and theoretically substantiated the method of fast repopulation of the nonequidistant atomic and nuclear levels through interaction with a bichromatic coherent resonant wave [3, 4].

However, in many cases, e.g., in the gas phase, the necessity may arise of polarizing atoms and nuclei containing equidistant Zeeman levels. In this work, a method is suggested for repopulating and polarizing such levels at room temperature with the use of two coherent resonant phase-shifted electromagnetic waves.

Let us consider a system of three ($I = 1$) equally populated Zeeman levels. The levels corresponding to spin projections +1, –1, and 0 are numbered 1, 2, and 3, respectively. Let the system be subjected simultaneously to two coherent waves having identical frequencies but shifted in phase relative to each other by a fixed value $\Delta_\varphi = \varphi_1 - \varphi_2$. Because the frequencies are identical, both fields simultaneously act on each of the transitions between the levels of the system.

The set of equations of the time-dependent perturbation theory for the probability amplitudes $a_i(t)$ in the resonant approximation has the form

$$\dot{a}_1 = -iWa_3, \quad \dot{a}_2 = -iW^*a_3, \qquad \dot{a}_3 = -iW^*a_1 - iWa_2. \tag{1}$$

Here, W is the matrix element of the operator of interaction with fields:

$$W = g_1 + g_2\exp(i\Delta_\varphi), \tag{2}$$

where $g_1 \sim H_1$ and $g_2 \sim H_2$ are the matrix elements for the transitions induced by the fields of strengths $H_{1,2}$. The matrix element W has the form

$$W = \Omega_0\exp(i\alpha/2), \qquad \Omega_0 = (g_1^2 + g_2^2 + 2g_1g_2\cos\Delta_\varphi)^{1/2}, \qquad \alpha = 2\arctan[g_2\sin\Delta_\varphi/(g_1 + g_2\cos\Delta_\varphi)]. \tag{3}$$

One can show that for identical g_i the phase α is equal to the phase difference Δ_φ between the waves. The level populations $a_{ii} = |a_i(t)|^2$ obtained from Eq. (1) with the use of Eq. (3) are

$$a_{11} = [1 - \sqrt{2}\sin X\sin(\alpha/2) - 1/2\sin^2 X\cos\alpha]/3,$$
$$a_{22} = [1 + \sqrt{2}\sin X\sin(\alpha/2) - 1/2\sin^2 X\cos\alpha]/3, \tag{4}$$
$$a_{33} = (1 + \sin^2 X\cos\alpha)/3.$$

Here, $X = \Omega t$, where $\Omega = \sqrt{2}\,\Omega_0$ is the level repopulation rate (Rabi frequency). It is essential that, in the case of interest, it depends not only on the field

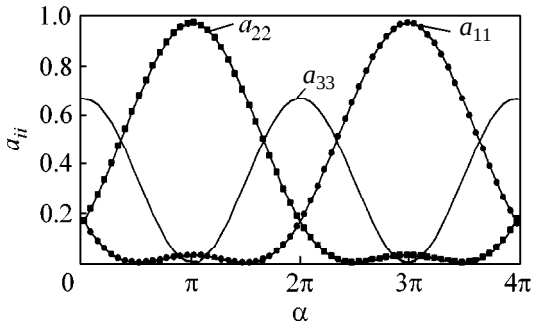

Fig. 1. Populations of the Zeeman levels of a particle with spin 1 as functions of phase difference α between the polarizing fields ($X = \pi/2$).

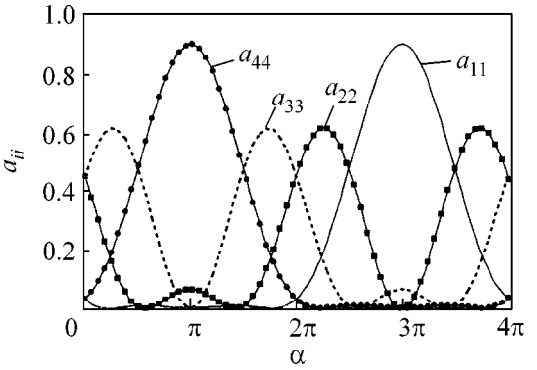

Fig. 2. Populations of the Zeeman levels of a particle with spin 3/2 as functions of phase difference α between the polarizing fields ($X = \pi/2$).

strengths, but also on the phase difference. One can see from Eq. (3) that at

$$\cos\Delta_\varphi = -(g_1^2 + g_2^2)/2g_1g_2 \qquad (5)$$

$\Omega_0 = 0$, so that the repopulation does not occur. Figure 1 shows the level populations as functions of α after the π/2 pulse ($X = \pi/2$). It follows from Eq. (4) that the pulses with a duration of a multiple of π do not repopulate the system. Interaction during a time period much longer than $1/\Omega$ brings about only the orientation of the system, with $a_{11} = a_{22} \neq a_{33}$. Note that a single resonant field ($\Delta_\varphi = 0$ and $g_1 = g_2$), although repopulates the three-level system, also leads only to its orientation. It is significant that the two analogous fields, when acting on a system of two equally populated levels, do not repopulate them at any α value and any pulse duration. As for the system of three equidistant levels, the π/2 pulses with phase shifts $\alpha = \pi$ and 3π can strongly polarize it (up to 97%, Fig. 1; the total population of the system is set equal to 1). However, it should be taken into account that the repopulation rate and, hence, the inverse duration of the π/2 pulse, depends on the phase shift and may be close to zero in our case. That is why one cannot obtain the highest possible polarization at $g_1 = g_2$ and $\Delta_\varphi = \pi$ and 3π, because then $\Omega_0 = 0$. Hence, to obtain strong polarization, one should slightly depart from these conditions. For $\alpha = 2\pi$, one also can induce only the orientation for any pulse duration.

The repopulation of a four-level system of Zeeman levels ($I = 3/2$) induced by an analogous two-phase field can be considered in a similar manner. In this case, the set of equations for the amplitudes is written as

$$\begin{aligned} \dot a_1 &= -i\sqrt{3}W^* a_2, \quad \dot a_2 = -i\sqrt{3}Wa_1 - i2W^* a_3, \\ \dot a_3 &= -i2Wa_2 + -i\sqrt{3}W^* a_4, \quad \dot a_4 = -i\sqrt{3}W^* a_3, \end{aligned} \qquad (6)$$

where W is the matrix element analogous to (2) but with elements g_i corresponding to spin 3/2. The levels with projections +3/2, +1/2, –1/2, and –3/2 are numbered 1, 2, 3, and 4, respectively. The characteristic equation corresponding to Eq. (6) yields two level repopulation rates: $\Omega_1 = 3\Omega_0$ and $\Omega_2 = \Omega_0$. The populations a_{ii} of the four-level system depend on time as follows:

$$\begin{aligned} a_{11} &= [1 - \sqrt{3}/2\sin^2(X)\cos\alpha \\ &- \sin(X)Y_1\sin(\alpha/2) + 1/4\sin^3(X)\sin(3\alpha/2)]/4; \\ a_{22} &= [1 + \sqrt{3}/2\sin^2(X)\cos\alpha \\ &- \sin(X)Y_2\sin(\alpha/2) - 3/4\sin^3(X)\sin(3\alpha/2)]/4; \\ a_{33} &= [1 + \sqrt{3}/2\sin^2(X)\cos\alpha \\ &+ \sin(X)Y_2\sin(\alpha/2) + 3/4\sin^3(X)\sin(3\alpha/2)]/4; \\ a_{44} &= [1 - \sqrt{3}/2\sin^2(X)\cos\alpha \\ &+ \sin(X)Y_1\sin(\alpha/2) - 1/4\sin^3(X)\sin(3\alpha/2)]/4; \\ Y_1 &= [\sqrt{3} + (3 - 2\sqrt{3})/4]\sin^2(X); \\ Y_2 &= [2 - \sqrt{3} + (6\sqrt{3} - 9)/4]\sin^2(X). \end{aligned} \qquad (7)$$

Here, $X = 2\Omega_0 t$ and the α value is also determined by Eq. (3). The a_{ii} values are shown in Fig. 2 as functions of α for $X = \pi/2$. One can see that at $\alpha = \pi$ the population a_{44} is as high as 93%, the population a_{22} is 6.7%, and the populations of levels 1 and 3 are virtually zero.

However, it should be noted that these calculations do not take into account the break in coherence of the level population process, e.g., as a result of atomic collisions in the gas. For instance, in gases with atomic density $\sim 10^{15}$ cm^{-3}, the collision time at room temperature may be as short as $\sim 10^{-4}$ s. The period of Rabi oscillations should not exceed this value. Since the oscillation period depends on the phase shift between the fields, account should be taken of these constraints when choosing Δ_φ.

It appears to us that the suggested method of polarization can find use in quantum computer design. The most important problems in this respect are a search for

a quantum system suitable for use as an information medium in quantum computations and the problem of initiating the initial state of this system. As known, a particle with spin 1/2 is one of the most important examples of such physical systems. The possibility of using particles with spin larger than 1/2 as elements of an information medium for quantum computers is substantiated in [5]. It is demonstrated above how can the initially uniformly populated levels of a particle with spin 3/2 be polarized by our method.

In summary, bichromatic waves [3, 4] and mutually phase-shifted monochromatic fields can be used for the efficient polarization of atoms and nuclei in both gaseous medium and impurity centers. The possibility of atoms and nuclei being polarized at room temperatures opens the door to the use of this method in quantum computer design, because this will allow the initial state of the elements of an information medium of a quantum computer to be created without using ultralow temperatures.

REFERENCES

1. O. Kocharovskaya, Phys. Rep. **219**, 175 (1992).
2. E. Paspalakis and P. L. Knight, Phys. Rev. Lett. **81** (2), 293 (1998).
3. D. F. Zaretsky and S. B. Sazonov, Laser Phys. **7** (3), 1 (1997).
4. D. F. Zaretskiĭ and S. B. Sazonov, Zh. Éksp. Teor. Fiz. **113**, 1181 (1998) [JETP **86**, 644 (1998)].
5. A. R. Kessel' and V. L. Ermakov, Zh. Éksp. Teor. Fiz. **117**, 517 (2000) [JETP **90**, 452 (2000)].

Translated by V. Sakun

JETP Letters, Vol. 72, No. 4, 2000, pp. 174–177. Translated from Pis'ma v Zhurnal Éksperimental'noĭ i Teoreticheskoĭ Fiziki, Vol. 72, No. 4, 2000, pp. 250–255.

Observation of the Coherence between the Plasma Density Fluctuations in the Core and at the Edge of the Plasma Column in the L-2M Stellarator

G. M. Batanov, L. V. Kolik, A. E. Petrov, K. A. Sarksyan, N. K. Kharchev, Yu. V. Khol'nov, and S. V. Shchepetov

Institute of General Physics, Russian Academy of Sciences, ul. Vavilova 38, Moscow, 117942 Russia
e-mail: sarksian@fpl.gpi.ru

Received July 3, 2000

Results are presented from the measurements of the radial coherence between the plasma density fluctuations in the core and at the edge of the plasma column in the L-2M stellarator. It is found that the radial coherence between these fluctuations is fairly high: the coherence coefficient attains a value of higher than 0.5 for the spectral wavelet components with frequencies lying in the range from several kilohertz to 30 kHz. The statistical characteristics of density fluctuations are also studied. It is shown that the power distribution function of the plasma density fluctuations in the plasma core differs from Gaussian. © *2000 MAIK "Nauka/Interperiodica".*

PACS numbers: 52.25.Gj; 52.55.Hc; 52.70.-m

1. The problem of the influence of turbulence on plasma transport and confinement in toroidal magnetic systems has recently attracted increased interest. Most of the effort in these studies is directed at clarifying the role of edge plasma turbulence in the global plasma processes, first of all, those occurring during the transitions to the improved confinement modes (the L–H transition and the formation of the internal transport barrier) [1]. A large number of papers are devoted to the recently found phenomenon of anomalous fast transport and the formation of coherent structures in the edge plasma [2]. In some experiments, attempts were made to simultaneously measure the plasma fluctuations both at the edge of the plasma column and in its deeper regions. [3, 4]. However, direct measurements of the radial coherence between the fluctuations of plasma parameters in the plasma core and at the plasma edge have not yet been carried out. At the same time, the importance of such measurements is evident, because the presence of radial coherence between the fluctuations in the core and at the edge of the plasma column or the absence of such coherence might indicate the cause of anomalous transport. The above gap in the experimental studies can be explained, to some extent, by the absence of both diagnostic techniques capable of simultaneously measuring spatially separated plasma fluctuations and relevant methods of spectral analysis.

The aim of this study was to measure the radial coherence between the plasma density fluctuations localized in the core and at the edge of the plasma column in the L-2M stellarator. For this purpose, different diagnostics were used. The plasma density fluctuations δn in the edge plasma were detected with movable probes (see [5] for details). The δn fluctuations in the plasma core were measured using a homodyne setup that recorded the heating gyrotron radiation scattered by density fluctuations. The setup detected the radiation arising from scattering of the ordinary component of high-power gyrotron radiation with the electric field $\mathbf{E}_{\text{ord}} \parallel \mathbf{B}$, where $\mathbf{B}$ is the stellarator toroidal magnetic field; this component results from splitting of the linearly polarized radiation at the plasma boundary. When analyzing experimental data, we used a modern method of wavelet analysis, which allowed us to obtain the information on the fluctuation spectra and the coherence of the spectral components with a high time resolution on the real-time scale [6].

2. The parameters of the L-2M stellarator are described in detail in [7]. The major torus radius is R = 100 cm, and the mean vacuum separatrix radius is r_s = 11.5 cm. The plasma was created and heated with a gyrotron operating at a frequency of f_0 = 75GHz ($\lambda_0 \approx$ 4 mm). Gyrotron radiation in the form of a Gaussian beam with extraordinary polarization ($\mathbf{E}_0 \perp \mathbf{B}$) was launched into the stellarator chamber.[1] The experiments were carried out at a power of 150–200 kW and pulse duration of 10–12 ms under the conditions of electron cyclotron resonance (ECR) at the second harmonic of the electron gyrofrequency ω_{He} ($\omega_0 = 2\omega_{\text{He}}$, where $\omega_0 = 2\pi f_0$). The plasma parameters in these experiments were the following: the mean plasma density was $n = (1–2) \times 10^{19}$ m^{-3}, the central electron tem-

[1] As was mentioned above, the same radiation was used for diagnostic purposes.

0021-3640/00/7204-0174$20.00

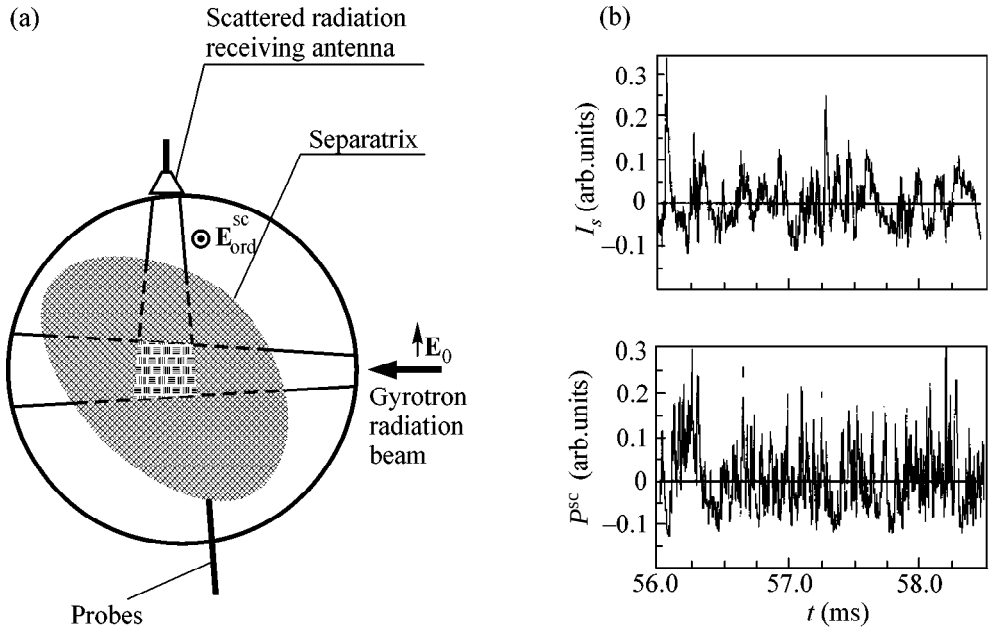

Fig. 1. (a) Arrangement of diagnostics in the poloidal cross section in which the gyrotron beam is launched. (b) Fluctuations of the probe-current signal I_s and scattering signal P^{sc}.

perature was $T_e(0) \sim 0.5$–0.7 keV, and the ion temperature was $T_i \sim 0.15$ keV. The working gas was hydrogen (H_2). Figure 1a schematically shows the arrangement of the diagnostics in the poloidal cross section of the stellarator chamber. A horn antenna that was positioned in the upper port received the ordinary component of the gyrotron radiation scattered at an angle of $\pi/2$ by the δn fluctuations localized in the central region of the plasma. This region (which is indicated in Fig. 1a by small squares) is the intersection region of the incident and scattered microwave beams. The diameter of the scattering region is $d = 5$ cm. For a wave number of gyrotron radiation $k_0 = 15$ cm^{-1}, the Bragg condition for scattering at an angle of $\pi/2$ is satisfied for the density fluctuations δn whose size corresponds to $k_{sc} = 20$ cm^{-1} ($\lambda_{sc} = 3$–4 mm). The signals from the movable probes, which measured the ion saturation current I_s, provided the information on the plasma density fluctuations, because $I_s \sim n$ and, consequently, $\delta I_s \sim \delta n$. The probes could be moved by 1.5–2 cm inside the separatrix. This corresponded to the relative radius $r/r_s = 0.85$–0.8 (here, r is the radial coordinate of the probe). The distance between the central region and the edge plasma was 5–7 cm. Figure 1b shows the typical fluctuations of the probe-current signal I_s and scattering signal P^{sc}. Both signals are bursty; the durations of the bursts and their fronts are different. When applying the wavelet method of spectral analysis, it makes sense to speak about the spectral characteristics of the bursts. In order to confirm that the scattering signal came from the central region, we applied a low vertical magnetic field B_v, which compensated the Shafranov shift of the magnetic axis. According to theoretical predictions, at $B_v = -(40$–$70)$ G, the stability region of ideal MHD modes in the plasma core becomes narrower and, consequently, the level of plasma fluctuations should increase [8]. At the same time, the applied field B_v should not significantly affect resistive ballooning modes, which determine the level of δn fluctuations in the edge plasma [4].

3. Let us consider the results of the wavelet analysis of fluctuation signals. Figure 2 demonstrates the wavelet spectra of the probe-current signal (Fig. 2a) and the scattering signal (Fig. 2b). Both signals were recorded for two values of the vertical field: $B_v = 0$ and –40 G. For $B_v = -40$ G, there is a significant (twofold or even higher) increase in the spectral density of the scattered-radiation fluctuations over the entire frequency range (Fig. 2b). Taking into account the above considerations, this increase confirms that the scattering occurs in the central region of the plasma column. At the same time, the difference between the spectra of the δn fluctuations detected by the probe in the edge plasma at both $B_v = 0$ and $B_v = -40$ G is usually insignificant. Thus, in Fig. 2a, the difference is seen only at frequencies higher than 300 kHz. However, in some shots with $B_v = -40$ G, we observed in edge plasma a significant change in the spectrum of δn fluctuations in a broader frequency range, which was noted earlier in [4]. It is likely that, under certain conditions, the instability in the plasma core can affect the edge plasma.

Let us now consider the results that should answer the principal question of whether there is a coherence between the spectral components of the scattering and probe-current signals, i.e., between the δn fluctuations

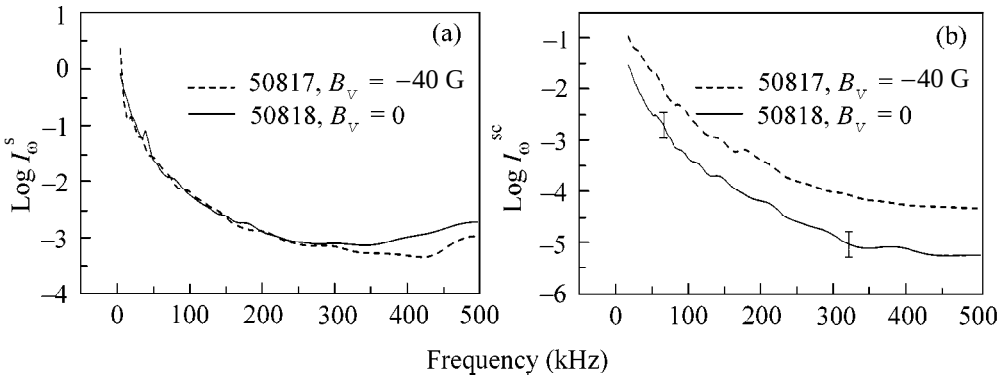

Fig. 2. Wavelet spectra of (a) the ion saturation current at the probe (r/r_s = 0.8) and (b) scattered gyrotron radiation.

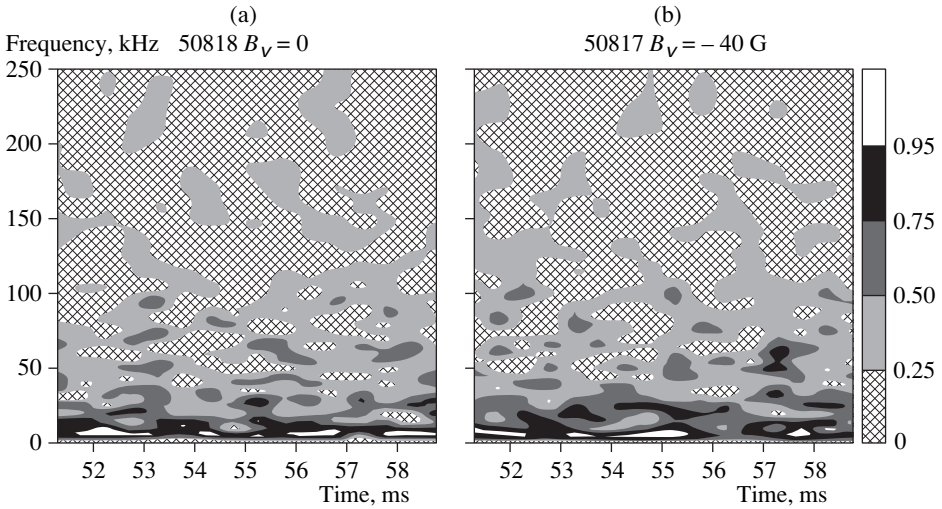

Fig. 3. Radial wavelet coherence between the fluctuations of the ion saturation current at the probe and scattered radiation for B_V = (a) 0 and (b) –40 G. The value of the coherence coefficient is shown by the shades of black and white.

in the central and peripheral regions of the plasma column, which are separated in the radial direction by several centimeters. Figure 3 shows the wavelet coherence spectra between the fluctuations of the scattering and probe-current signals for $B_V = 0$ (Fig. 3a) and $B_V = -40$ G (Fig. 3b). These spectra exhibit the following characteristic features: (i) The coherence coefficient K in the frequency range from several kilohertz to 100 kHz is fairly high. (ii) The higher values of the coherence coefficient ($K > 0.5$) correspond to the lower frequency components (<30 kHz). (iii) The time behavior of the coherence is bursty, which indicates the formation of temporal coherent structures. (iv) The applied vertical field does not change the coherence structure but significantly extends the coherence range toward higher frequencies.

Hence, we can state that there is a radial coherence between the plasma density fluctuations that are localized in the central and peripheral regions of the plasma column in the L-2M stellarator. The length of the coherence region is 5–7 cm.

Finally, we examine such a statistical characteristic of fluctuation signals as the power distribution function (PDF) of the δn fluctuations. Figure 4 shows the calculated PDF of the fluctuations of the scattering signal and the approximation of the PDF by a Gaussian distribution. It is seen that the PDF of the scattering signal differs significantly from Gaussian. First, the PDF of the scattering signal is asymmetric (the skewness is 0.9). Second, the fraction of large-amplitude fluctuations is significantly greater than for the Gaussian distribution (the kurtosis is 4.8). The PDF of fluctuations of the probe-current signal in the edge plasma is close to Gaussian, which was previously observed in [9].

4. Let us briefly summarize the results of the above experiments carried out in the L-2M stellarator:

(i) The use of a technique based on scattering of the heating gyrotron radiation by the plasma density fluctuations, together with the probe technique, has allowed

us to simultaneously measure the characteristics of density fluctuations both in the core and at the edge of the plasma column.

(ii) High radial coherence (with the coherence coefficient $K > 0.5$) between the spectral components of the plasma density fluctuations in the central and peripheral plasma regions separated by a distance of 5–7 cm has been found.

(iii) The radial-coherence coefficient is maximum for the frequency components lying in the range 5–30 kHz.

(iv) The PDF of the density fluctuations in the plasma core differs significantly from the equilibrium Gaussian distribution.

The question naturally arises as to what mechanism provides the high radial coherence of the plasma density fluctuations and how the fluctuations are structured in space and time. In this connection, we briefly consider which types of oscillations are unstable in the plasma core and at the plasma edge under our experimental conditions. At low plasma pressures p and $B_v = 0$, ideal MHD modes can develop in the plasma core. For $\bar{\beta} \geq 0.09\%$ (where $\bar{\beta} = 8\pi\bar{p}/B^2$ and the bar stands for averaging over the volume), as is the case in our experiments, these modes are stabilized due to the "self-stabilization" effect [8]. However, electrostatic drift modes can develop under these conditions. If the condition $\beta(L_s/L_p)^2 \ll 1$ (where L_s and L_p are the characteristic scale lengths of variations in the rotational transform and the plasma pressure, respectively) is satisfied (which is also typical of our experiments), then, for this type of instability, the role of magnetic field fluctuations is negligible. For $B_v = -40$ G, the instability of ideal MHD modes is a dominant source of turbulence in the plasma core, because these modes can be stabilized only at pressures substantially exceeding the pressures typical of our experimental conditions. At the plasma edge (i.e., for $r/r_s \geq 0.5$), turbulence is associated with the onset of resistive interchange modes, which have been thoroughly studied both theoretically and experimentally [5, 8]. In principle, we may suggest that the radial-coherence regions appear due to the coupling of unstable modes with different toroidal and poloidal numbers. As is seen from Figs. 2 and 3, whatever type of instability is dominant in the plasma core, the coherence and the structure of the coherence regions remain almost the same, although the fluctuation amplitude can vary significantly. However, the presence of such extended radial-coherence regions cannot be explained within the linear theory. All these facts apparently point to a unified nonlinear mechanism that provides the high radial coherence of the plasma density fluctuations during the onset of different types of instabilities in the plasma core. As for the specific type of structures that form the coherence regions, it is worth noting that, as was previously shown in [10], vortex structures can be formed in the plasma of the L-2M stellarator. This was also pointed out in [11]. We may suggest that, under our experimental conditions, vortex-type structures were also formed.

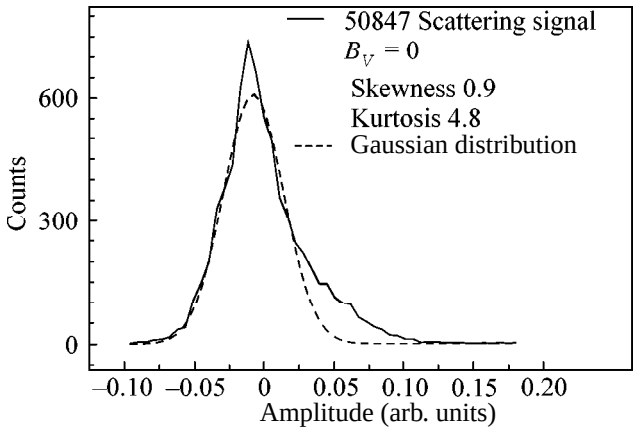

Fig. 4. PDF of fluctuations of the scattering signal.

We are grateful to the L-2M team for assistance in carrying out the experiments. This work was supported by the Russian foundation for Basic Research, project no. 00-02-17507.

REFERENCES

1. J. W. Connor, P. Burraffi, J. G. Cordey, *et al.*, Plasma Phys. Controlled Fusion **41**, 693 (1999).
2. C. Hidalgo, Plasma Phys. Controlled Fusion **37**, A53 (1995).
3. V. Antonni, M. Bagatin, R. Cavazzona, *et al.*, in *EU–US Transport Task Force Workshop, Goteborg, 1998*, p. 23.
4. D. K. Akulina, G. M. Batanov, M. S. Berezhetskiĭ, *et al.*, Fiz. Plazmy **26**, 3 (2000) [Plasma Phys. Rep. **26**, 1 (2000)].
5. G. M. Batanov, O. I. Fedyanin, N. K. Kharchev, *et al.*, Plasma Phys. Controlled Fusion **40**, 1241 (1998).
6. N. M. Astaf'eva, Usp. Fiz. Nauk **166**, 1145 (1996) [Phys. Usp. **39**, 1085 (1996)].
7. V. V. Abrakov, D. K. Akulina, E. D. Andryukhina, *et al.*, Nucl. Fusion **37**, 233 (1997).
8. L. M. Kovrizhnykh and S. V. Shchepetov, Fiz. Plazmy **6**, 976 (1980) [Sov. J. Plasma Phys. **6**, 533 (1980)].
9. N. K. Kharchev, N. N. Skvortsova, and K. A. Sarksian, J. Math. Sci. (2000) (in press).
10. G. M. Batanov, K. M. Likin, K. A. Sarksyan, and M. G. Shats, Fiz. Plazmy **19**, 1199 (1993) [Plasma Phys. Rep. **19**, 628 (1993)].
11. B. A. Carreras, B. van Milligen, C. Hidalgo, *et al.*, Phys. Rev. Lett. **83**, 3653 (1999).

Translated by N. Larionova

JETP Letters, Vol. 72, No. 4, 2000, pp. 178–181. Translated from Pis'ma v Zhurnal Éksperimental'noĭ i Teoreticheskoĭ Fiziki, Vol. 72, No. 4, 2000, pp. 256–260.

Light Absorption in Hydrogen Plasma on the Bound–Free and Free–Free Transitions of the H–H$^+$ System

V. S. Lebedev, L. P. Presnyakov, and I. I. Sobel'man

Lebedev Institute of Physics, Russian Academy of Sciences, Leninskiĭ pr. 53, Moscow, 117924 Russia

Received July 4, 2000

Radiative transitions in the proton–hydrogen atom system are theoretically analyzed over a wide range of wavelengths and temperatures of equilibrium hydrogen plasma. The light absorption at $T \sim 1500$–3500 K due to photodissociation and transitions in the H_2^+ ion continuum is shown to make a contribution that is comparable with the photoabsorption in the electron–hydrogen atom system near the maximum of the Planck distribution.

PACS numbers: 33.80.Gj; 52.25.-b

The study of radiative characteristics of a hydrogen plasma containing, apart from the H atoms and H_2 molecules, H^- and H_2^+ ions allows a detailed theoretical analysis and is of interest for numerous applications. It is known that the main contribution to the visible absorption by a quasi-equilibrium hydrogen plasma with temperature $T \approx 6000$ K (typical of the solar photosphere) comes from the negative hydrogen ion H^-, whose concentration is as small as $N_{H^-}/N_H \sim 10^{-8}$ of the concentration of the neutral hydrogen atom H(1*s*). In the infrared region below the threshold of the $H^-(1s^2 {}^1S) + \hbar\omega \longrightarrow H(1s) + e$ ($\lambda > \lambda_{H^-}^{th} = 1.64$ μm) process, photoabsorption is determined by the free– free transitions $H(1s) + e + \hbar\omega \longrightarrow H(1s) + e$. The photoabsorption coefficients for both processes are known with a high accuracy [1, 2]. The concentration $N_{H_2^+}$ of molecular ion H_2^+ at $T \sim 6000$–$10\,000$ K is of the same order as the concentration of H^- and becomes much higher than the latter with decreasing temperature ($T < 3000$ K).

Quantitative study of the bound–free and free–free radiative transitions in the H–H$^+$ system was first performed by Bates on the basis of the quasi-static theory of photoabsorption [3] and accurate calculations of the electronic terms [4] and oscillator strengths [5] for the $X^2\Sigma_g^+ \longrightarrow A^2\Sigma_u^+$ transition. The quantum-mechanical calculations [6, 7] of the photodissociation cross sections for the H_2^+ ion (without making allowance for the rotational excitation, $J = 0$) were aimed at analyzing the beam experiments rather than the radiative characteristics of the plasma. The presently available data suggest [8] that in an equilibrium hydrogen plasma with $T \sim 4500$–$10\,000$ K the integral contribution of photoabsorption by the H_2^+ ion is small (<7–10%) compared to that of the H^- ion.

It is shown in this work that absorption by the proton–hydrogen atom system in the wavelength range $\lambda \sim 1.6$–4 μm at temperatures $T \sim 1400$–3500 K is of the same order as, or even exceeds, absorption by the electron–hydrogen atom system. The calculations were carried out for the contributions of all rovibrational levels vJ of the H_2^+ ion to the cross sections and the coefficients of dissociative absorption (bound–free transitions):

$$H_2^+({}^2\Sigma_g^+) + \hbar\omega \longrightarrow H_2^+({}^2\Sigma_u^+) \longrightarrow H(1s) + H^+. \quad (1)$$

Similar calculations were carried out for the free–free transitions:

$$H(1s) + H^+ + \hbar\omega \longrightarrow H(1s) + H^+ \quad (2)$$

with changing the electronic state ${}^2\Sigma_g^+ \longrightarrow {}^2\Sigma_u^+$ of the H–H$^+$ quasimolecule.

The vJ-summarized coefficient of dissociative absorption at a frequency $k_T^{(1)}(\omega)$ [cm^{-1}] (proportional to the concentration $N_{H_2^+}$ of the molecular ions H_2^+) is expressed through the Boltzmann-averaged cross section $\sigma_T^{(1)}(\omega)$ [cm^2] for process (1) at a given plasma temperature:

$$k_T^{(1)}(\omega) = \sigma_T^{(1)}(\omega) N_{H_2^+},$$
$$\sigma_T^{(1)}(\omega) = \frac{1}{Z_{v.r}} \sum_{vJ} (2J+1) \sigma_{vJ}^{(1)}(\omega) e^{-\epsilon_{vJ}/kT}. \quad (3)$$

0021-3640/00/7204-0178$20.00

Here, $\sigma_{vJ}^{(1)}(\omega)$ is the partial cross section for photodissociation from the energy level ϵ_{vJ} and $Z_{v,r}$ is the rovibrational partition function of the H_2^+ ion in its ground electronic state $X^2\Sigma_g^+$.

In this work, the theoretical treatment of photoprocesses (1) and (2) is carried out on a unified basis of the theory of nonadiabatic transitions between the electronic states of a two-atomic system [9] in the approximation of a quasicontinuous spectrum of the rovibrational states vJ. Such an approach is justified, because the main contribution to the total absorption coefficient in the visible, infrared, and near-ultraviolet regions comes from the multitude of vJ states with large quantum numbers v and J. For a given frequency ω, the transitions occur in a narrow vicinity of the point R_ω where the potential energy curves for the initial $H_2^+(X^2\Sigma_g^+) + \hbar\omega$ and final $H_2^+(A^2\Sigma_u^+)$ states intersect, i.e., where the splitting between the even and odd terms of the molecular ion becomes equal to the photon energy, $U_u(R_\omega) - U_g(R_\omega) = \hbar\omega$. In the optical range, $R_\omega \gg R_e$, where $R_e = 1.058$ Å is the equilibrium internuclear distance in the ground $X^2\Sigma_g^+$ state. The slopes of the crossing potential curves $U_g(R)$ of the bound even and $U_u(R)$ of the repulsive odd terms have different signs. Depending on the value of ω, the R_ω point may occur either in the classically allowed ($R < a$) or in the classically forbidden ($R > a$) region with respect to the turning point $R = a$ at the $U_g(R)$ term.

The radial dipole-moment matrix elements between the wave functions of relative nuclear motion and the partial cross sections for the nonadiabatic transitions were calculated using the Landau–Lifshitz quantum formula [9]. The result is expressed in terms of the Airy functions and allows the evaluation of the contributions from both classical and nonclassical regions of proton motion. In the calculation of the Boltzmann-averaged photodissociation cross section $\sigma_T^{(1)}(\omega)$, the summation in Eq. (3) over the rovibrational levels vJ was replaced by integration over dv and dJ and accomplished by the method developed in [10]. The absorption coefficient in the continuous spectrum of the H_2^+ system was calculated by analogy with the bound–free transitions.

The absorption coefficient $k_T^{(2)}(\omega)$ [cm^{-1}] for process (2) is proportional to the product of the concentrations $N_H N_{H_2^+}$ of the H(1s) atoms and the protons H^+ in the free state. Since the total equilibrium concentration $N_{H_2^+}$ of the $H_2^+(X^2\Sigma_g^+)$ ions in Eq. (3) obeys the mass action law and, hence, can be expressed through $N_H N_{H^+}$, it is convenient to introduce the total absorption coefficient $k_T(\omega)$ for processes (1) and (2):

$$k_T(\omega) = k_T^{(1)}(\omega) + k_T^{(2)}(\omega) = \eta_T(\omega) N_H N_{H^+},$$
$$K_T(\omega) = k_T(\omega)[1 - e^{-\hbar\omega/kT}], \quad (4)$$

where $\eta_T(\omega)$ [cm^5] is the photoabsorption rate constant. The $K_T(\omega)$ quantity in Eq. (4) describes the absorption coefficient at a frequency ω with allowance made for the induced emission.

The total absorption coefficient $K_T(\omega)$ has the form

$$k_T(\omega) = 4\pi^3\alpha\left(\frac{\hbar^2}{m}\right)\frac{R_\omega^2 f_{ug}(R_\omega)}{\Delta F_{ug}(R_\omega)} \times \exp\left(-\frac{U_g(R_\omega)}{kT}\right)\Theta_T(\omega) N_H N_{H^+}. \quad (5)$$

In Eq. (5), $f_{ug}(R_\omega)$ is the oscillator strength of the electronic transition $^2\Sigma_g^+ \longrightarrow {}^2\Sigma_u^+$ at the internuclear separation R_ω; $\Delta F_{ug}(R_\omega) = |dU_u/dR - dU_g/dR|_{R = R_\omega}$ is the difference in the slopes of the potential curves for the bound U_g and the repulsive U_u terms of the H_2^+ ion correlating with the electronic states H(1s) + H^+ at $R \longrightarrow \infty$ [$U_g(\infty) = U_u(\infty) = 0$]; m is the electron mass; and $\alpha = e^2/\hbar c$ is the fine structure constant. The dimensionless factor $\Theta_T(\omega)$ accounts for the difference between the quasiclassical result [$\Theta_T^{WKB}(\omega) = 1$] and the quantum result allowing for the tunnel transitions and the true behavior of the transition probabilities near the classical turning points:

$$\Theta_T(\omega) = 2\sqrt{\pi}\int_{\beta_{min}}^{\infty} e^{-\beta} d\beta \int_0^{\infty} \Lambda_\xi^{1/2} \mathrm{Ai}^2[-\Lambda_\xi(\beta - \xi)] d\xi. \quad (6)$$

Here, Ai(x) is the Airy function; $\beta_{min} = -U_u(R_\omega)/kT < 0$; and Λ_ξ is expressed through the slopes of the even, $F_g^{(\xi)} = -d(U_g + \mathscr{E})/dR$, and the odd, $F_u^{(\xi)} = -d(U_u + \mathscr{E})/dR$, terms including the rotational energy $\mathscr{E} = \hbar^2 J^2/2\mu R^2$ of the H_2^+ ion (μ is its reduced mass) and through the difference ΔF_{ug} at the R_ω point:

$$\Lambda_\xi = \left(\frac{2\mu}{\hbar^2}\right)^{1/3} \frac{kT|\Delta F_{ug}(R_\omega)|^{2/3}}{\left|F_g^{(\xi)}(R_\omega) F_u^{(\xi)}(R_\omega)\right|^{2/3}},$$
$$\xi = \frac{\mathscr{E}(R_\omega)}{kT}. \quad (7)$$

At $\Theta_T(\omega) = 1$, Eq. (5) coincides with the quasiclassical result [3].

The calculated photodissociation cross sections $\sigma_T^{(1)}(\omega)$ of the H_2^+ ion are presented in Fig. 1 for differ-

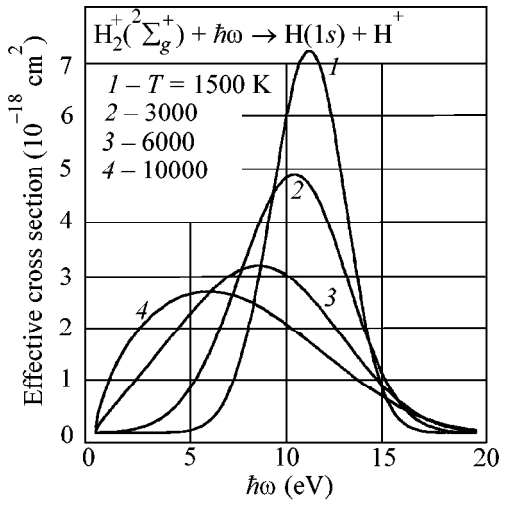

Fig. 1. Boltzmann-averaged H_2^+-photodissociation cross section $\sigma_T^{(1)}(\omega)$ as a function of photon energy $\hbar\omega$ at different temperatures.

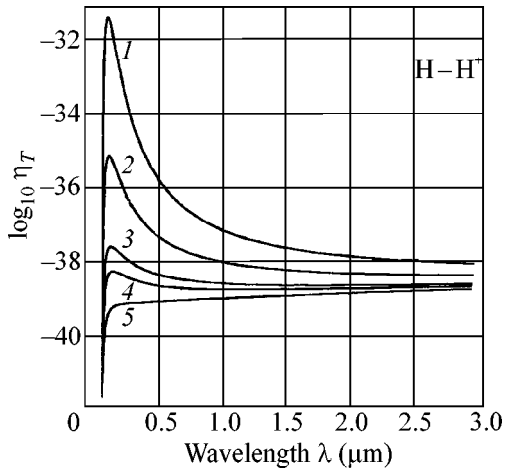

Fig. 2. Total photoabsorption rate constant $\eta_T^{H_2^+} = k_T^{H_2^+}/N_H N_{H^+}$ (cm^5) for the H–H$^+$ system vs. photon wavelength λ. Curves *1*, *2*, *3*, *4*, and *5* correspond to T = 1500, 2500, 4500, 5800, and 10 000 K, respectively.

ent temperatures of the hydrogen plasma. The numerical data on the potential energy curves and relevant oscillator strengths were taken from [4, 5, 11]. For each T, the cross section shows a clearly defined maximum σ_T^{max}, whose magnitude decreases while position $\omega_{max}(T)$ undergoes a low-frequency shift as the temperature increases. This is explained by the increase in the contribution of the high-lying energy levels vJ with a rise in temperature.

The cross-section maxima are typically of the order of 10^{-18}–10^{-17} cm^2. The summarized photoabsorption rate constants $\eta_T(\lambda)$ calculated for processes (1) and (2) in the H–H$^+$ system are presented in Fig. 2. One can see that, except at very high temperatures, the $\eta_T(\lambda)$ functions are very sharp near their maxima and that their typical values change by several orders of magnitude upon changing T from 1500 to 10 000 K. In the long-wavelength range $\lambda > 1.5$ μm, the η_T values change within ~10^{-39}–10^{-38} cm^5.

The relative contribution $\zeta = k_T^{(2)}/k_T$ of the free–free transitions (2) to the total photoabsorption coefficient is shown in Fig. 3 as a function of photon wavelength λ. At T = 1500 K and T = 3000 K, the ζ ratio is equal to 15–20% near the corresponding maxima of the Planck distribution (λ_{max} = 1.93 and 0.97 μm, respectively). On increasing the temperature and wavelength, the contribution of the free–free transitions (2) rapidly increases and becomes dominant.

It is of interest to compare the absorption coefficients $k_T^{H_2^+} = \eta_T^{H_2^+} N_H N_{H^+}$ and $k_T^{H^-} = \eta_T^{H^-} N_H N_e$ for the H–H$^+$ and H–e systems in which the proton and electron concentrations are equal, $N_{H^+} = N_e$. For $T \geq 4500$ K, such a comparison was carried out in [8]. The corresponding results for T = 1400 K are illustrated in Fig. 4. It is seen that both absorption coefficients become equal at $\lambda \approx 2$ μm, i.e., at the maximum of the Planck

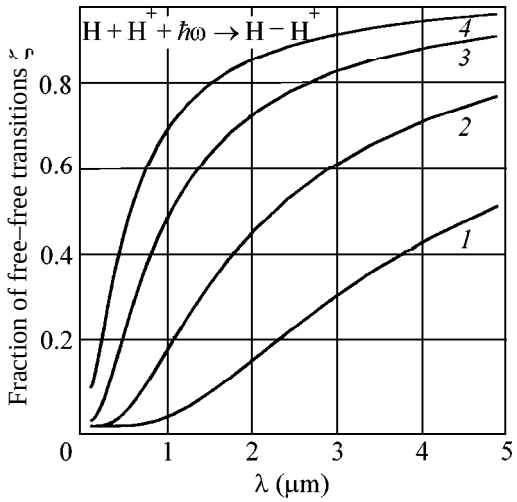

Fig. 3. The ratio $\zeta = k_T^{(2)}/k_T$ of the absorption coefficient $k_T^{(2)}$ of the H–H$^+$ continuum to the total coefficient $k_T = k_T^{(1)} + k_T^{(2)}$, including the contributions from processes (1) and (2). Curves *1*, *2*, *3*, and *4* correspond to T = 1500, 3000, 6000, and 10 000 K.

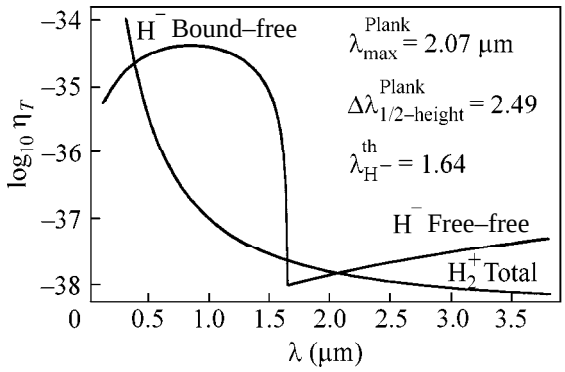

Fig. 4. Comparison of the total photoabsorption rate constants $\eta_T^{H_2^+}$ and $\eta_T^{H^-}$ caused by the bound–free and free–free transitions of the positive H_2^+ and negative H^- ions in hydrogen plasma (T = 1400 K).

distribution (its full width at half height is 1.27 μm < λ < 3.76 μm). In the range 1.64 μm < λ < 2 μm, i.e., up to the threshold $\lambda_{H^-}^{th}$, the contribution of the radiative processes studied in this work dominates. With an increase in T, the infrared absorption in the H–H^+ system becomes less strong than in H–e. Nevertheless, processes (1) and (2) still make a sizable contribution to the total absorption coefficient of the hydrogen plasma at T < 3000–3500 K. For instance, at T = 2800 K, the $k_T^{H_2^+}/k_T^{H^-}$ ratio at the photoneutralization threshold $\lambda_{H^-}^{th}$ = 1.64 μm and at λ = 2 μm amounts to 37 and 24%, respectively.

The calculations of photoabsorption by the H–H^+ system are of prime interest for the photospheres of low-temperature stars (~1500–3500 K). Among them are classes of stars with a very low content of the elements heavier than H or He (see [12]). The photoabsorption processes in these stars are mostly controlled by the hydrogen component of the atmosphere.

This work was supported by the Russian Foundation for Basic Research (project nos. 99-02-16602 and 00-02-17245) and the INTAS (grant no. 99-01326).

REFERENCES

1. M. Venuti and P. Decleva, J. Phys. B **30**, 4839 (1997).
2. K. L. Bell and K. A. Berrington, J. Phys. B **20**, 801 (1987).
3. D. R. Bates, Mon. Not. R. Astron. Soc. **111**, 303 (1951); **112**, 40 (1952).
4. D. R. Bates, K. Ledsham, and A. L. Stewart, Philos. Trans. R. Soc. London, Ser. A **246**, 215 (1953).
5. D. R. Bates, J. Chem. Phys. **19**, 1122 (1951).
6. Yu. D. Oksyuk, Opt. Spektrosk. **23**, 214 (1967) [Opt. Spectrosc. **23**, 115 (1967)].
7. G. H. Dunn, Phys. Rev. A **172**, 172 (1968).
8. V. S. Lebedev, L. P. Presnyakov, and I. I. Sobel'man, Astron. Zh. **77**, 3090 (2000) [Astron. Rep. **44**, 338 (2000)].
9. L. D. Landau and E. M. Lifshitz, *Quantum Mechanics: Non-Relativistic Theory* (Nauka, Moscow, 1974; Pergamon, Oxford, 1977).
10. V. S. Lebedev, J. Phys. B **24**, 1993 (1991).
11. D. M. Bishop and L. M. Cheung, J. Phys. B **11**, 3133 (1978).
12. A. Unsöld and B. Baschek, *The New Cosmos* (Springer-Verlag, Berlin, 1991).

Translated by V. Sakun

JETP Letters, Vol. 72, No. 4, 2000, pp. 182–185. Translated from Pis'ma v Zhurnal Éksperimental'noĭ i Teoreticheskoĭ Fiziki, Vol. 72, No. 4, 2000, pp. 261–266.

Phase Separation in Dipolar Systems: Numerical Simulation

A. F. Pshenichnikov and V. V. Mekhonoshin

Institute of Continuum Mechanics, Ural Division, Russian Academy of Sciences, ul. Akademika Koroleva 1, Perm, 614061 Russia

Received July 5, 2000

The first-order phase transition in a three-dimensional system of solid dipolar spheres is simulated by the Monte Carlo technique. It is shown that the dipole–dipole and steric interactions alone can induce the separation of a system into the low- and high- concentration phases. Additional attractive potentials need not be introduced. The phase diagram is constructed for the system of dipoles. The results of the simulation qualitatively agree with the predictions of some analytical models. © *2000 MAIK "Nauka/Interperiodica".*

PACS numbers: 64.70.Fx; 75.40.Mg; 75.50.Mm

Over the last several decades, there has been much discussion on the problem of phase transitions in systems of interacting dipoles. At present, various points of view are expressed on this subject and, in particular, on the first-order phase transition. A phase transition of the gas–liquid type was repeatedly observed (see, e.g., [1–5]) in magnetic fluids (colloidal solutions of single-domain particles), which are typical representatives of dipolar systems. On lowering the temperature or applying an external field, so-called droplike aggregates, i.e., drops of a "condensed" phase with a clearly visible interface, reversibly arise in a magnetic fluid. The drops are distinguished from the surrounding colloidal solution by a higher concentration of colloidal particles and, as a result, a higher magnetic permeability. In the absence of the external magnetic field, the droplike aggregate assumes the spherical shape because of the surface tension at its boundaries. The experimentally observed strong dependence of the phase-transition temperature on the field strength implies that magnetic dipolar interactions play an important part in such transitions. Nevertheless, the crucial question is whether the dipole–dipole interactions alone can be responsible for the first-order phase transition or they play a secondary role. The experiments with magnetic fluids do not provide an unambiguous answer to this question. Van der Waals forces can also be responsible for the many-particle aggregation in nonmagnetic colloids.

Phase transition of the gas–liquid type is predicted for the dipolar systems by a series of theoretical models [6–9]. In particular, according to the mean-sphere approximation [8] and the perturbation treatment [9], an initially homogeneous system of rigid magnetic dipoles can be separated into two phases upon lowering the temperature below some critical value. The resulting phases have identical superparamagnetic structures and differ only in the particle concentration. According to these models, the magnetic dipolar interactions, although markedly enhance the field-induced magnetization, cannot induce spontaneous magnetization. As distinct from [8, 9], the authors of [6, 7] predict "ferromagnetic" ordering for the particle magnetic moments in the condensed phase. However, this result naturally follows from the Weiss effective-field model that underlies developments [6, 7]. As shown in [10, 11], the Weiss model does not apply to concentrated systems, to which, evidently, the "liquid" phase belongs. It should also be noted that the applicability of the above-mentioned analytical models is restricted to small (compared to unity) aggregation parameters λ—the ratio of the energy of interparticle interactions to the thermal energy. Since the separation in the dipolar system occurs at $\lambda \gtrsim 3$, some care is required when applying the predictions of these models to the phase transitions.

High values of the aggregation parameter were considered in a group of analytical works [12–15]. In these works, the chain models were used. It was assumed that weakly interacting long chains of particles are the main structural units of dipolar systems. The conclusion about the absence of the first-order phase transitions in the dipolar systems followed from this approximation in a natural way.

Monte Carlo simulation is one of the most suitable methods of studying dipolar systems with large aggregation parameters. This method was used in a series of works, and it was concluded in most of them (e.g., [16–19]) that the first-order phase transition cannot occur in purely dipolar systems (i.e., without an additional attractive potentials). The exception is provided by recent publications [20–22]. In [20], the first-order transition was obtained for a system of spherocylinders differing only slightly from spheres. Based on this fact, the authors of [20] argued that the same transition may be anticipated in a system of spherical dipoles as well. Some evidence in favor of the phase transition was given in [21]. The authors of [21] have recognized three very weak minima in the number-density dependence of the free energy and assigned them to different

0021-3640/00/7204-0182$20.00

phases. An exceedingly small difference in entropies is the main feature of these phases. Finally, cluster analysis [22] showed that the quasi-spherical clusters containing as many as hundreds of particles and having a fractal dimensionality close to 3 are formed in a system of solid dipolar spheres at $\lambda > 3$. These aggregates were considered in [22] as nuclei of a more dense new phase. In this work, the occurrence of a two-phase state (the interface between two phases with different densities) is directly proved for the systems containing at least on the order of a thousand particles. The external field is absent. No additional attractive potentials are introduced.

One of the main challenges in the Monte Carlo method is that the sizes of a model system are restricted because of the limited computer resources. The properties of a small system depend on its size. A standard way of obviating this unwanted effect consists in imposing periodic boundary conditions. This procedure, in conjunction with the Ewald summation, is ordinarily applied to the dipolar systems [12–21]. However, it should be noted that the periodic boundary conditions are inefficient in the latter case and, moreover, may lead to erroneous results because of the infinite radius of dipole–dipole interactions. In particular, the periodic boundary conditions do not remove the problem of inclusion of the demagnetizing fields when calculating the magnetization of a system of superparamagnetic particles [22]. The demagnetization factors depend on the shape of the system and not on its size. Insofar as the volume of each phase in the dipolar system with separated phases is, obviously, smaller than the volume of the whole simulation cell, the periodic boundary conditions cannot affect the characteristic inhomogeneity scale in the system, so that the problem of transition to the thermodynamically large system remains unsolved. In this work, the periodic boundary conditions are not used. The model system is represented by a single array of a thousand particles (canonical ensemble). Such a choice provides a unique interpretation of the results. Although the properties of this system may be different from the properties of the thermodynamically large system, there are grounds to expect that these distinctions will be insignificant [23]. For instance, test computations with $\lambda < 10$ show [22] that, as the system size increases, monotonic changes in the properties of the dipolar system become imperceptible on the fluctuation background, provided that the number of particles in the cell is as large as several hundred. The problem was solved for two different configurations (spherical and cylindrical) of the system in zero external field. In doing so, various algorithms were used to speed up the process of establishing equilibrium state in the two-phase systems. The fact that the results proved to be identical for all variants makes them quite reliable.

In the first variant, the simulation cell was a long circular cylinder with rigid impenetrable isothermic walls. The particles were modeled by spheres of diameter d with identical dipole (magnetic) moments m. The contribution of the ith particle to the total energy of the system was the sum of the energies of dipole–dipole interactions of this particle with all other particles. In the dimensionless form (the particle diameter d was taken as a unit length), it is written as

$$\frac{U_i}{kT} = -\lambda \sum_{\substack{lj=1 \\ j \neq i}}^{N} \frac{1}{R_{ij}^3}\left[\frac{3(\mathbf{e}_i\mathbf{R}_{ij})(\mathbf{e}_j\mathbf{R}_{ij})}{R_{ij}^2} - \mathbf{e}_i\mathbf{e}_j\right], \qquad (1)$$

where R_{ij} is the dimensionless separation between the centers of two particles; $\mathbf{e}_i = \mathbf{m}_i/m$; and $\lambda = m^2/d^3kT$ is the aggregation parameter. The summation goes over all particles of the system, except for the probe particle. The steric interactions (i.e., mutual impenetrability of the particles) were taken into account by the exclusion of the transitions resulting in particle overlap. Therefore, the equilibrium state of the system was determined by two dimensionless parameters: the aggregation parameter λ and the particle volume fraction $\varphi = N/6R^2h$ (R and h are the dimensionless radius and height of the cylinder, respectively). A macroscopic state of the system is determined by the Cartesian coordinates of the particle centers and the orientations of their magnetic moments. The transition from one macroscopic state to the other was modeled by the standard Metropolis algorithm [23]. After many ($\sim 10^3$–10^5) Monte Carlo steps (MC steps), the thermodynamic equilibrium was established in the system, allowing its equilibrium state to be studied without direct evaluation of the configurational integral and the computational procedure to be sizably speeded up.

The initial particle distribution in the simulation cell is not critical for the Metropolis algorithm, but it strongly influences the rate of establishing equilibrium. The starting microscopic state is customarily formed through chaotic filling of the cell with particles. This simple method provides satisfactory results if the system is far from phase separation. However, when modeling the condensation process, a large number of weakly interacting clusters are formed, between which particle exchange is highly improbable. The time (i.e., the number of MC steps) of establishing thermodynamic equilibrium becomes too long, so that equilibrium becomes practically unattainable. To keep the computer time down, we simulated the "evaporation" process for the condensed phase. At zero time, all particles were assembled into a condensed drop that was placed in the middle part of the cylindrical cell. The evolution toward thermodynamic equilibrium was accompanied by drop evaporation and the formation of a "gas" phase. Simultaneously, the density and the boundaries of the condensed phase changed. This expedient prevented the breakdown of the system into many subsystems and allowed the quasi-equilibrium state to be attained within a reasonable computer time. Examples of establishing thermodynamic equilibrium in the

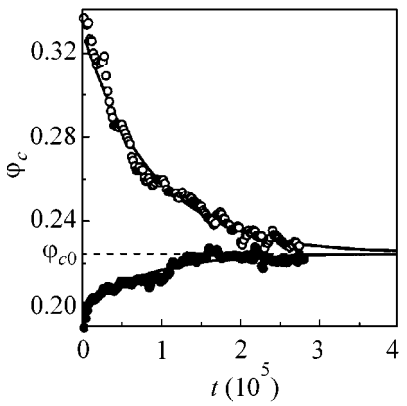

Fig. 1. Concentration of the dense phase vs. microstate number. ○ $\varphi_c(0) = 0.34$; ● $\varphi_c(0) = 0.18$. Solid lines are the exponential approximations of the computational results.

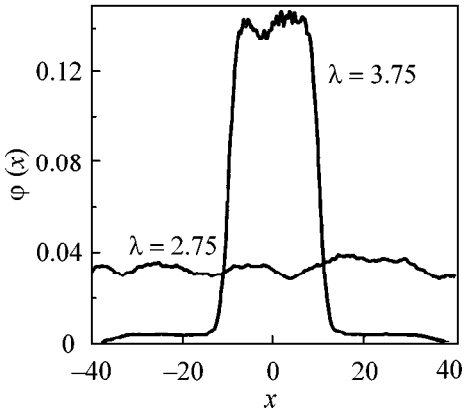

Fig. 2. Volume fraction of the dense phase vs. coordinate x along the cylinder axis for the system with mean particle density $\varphi = 0.04$.

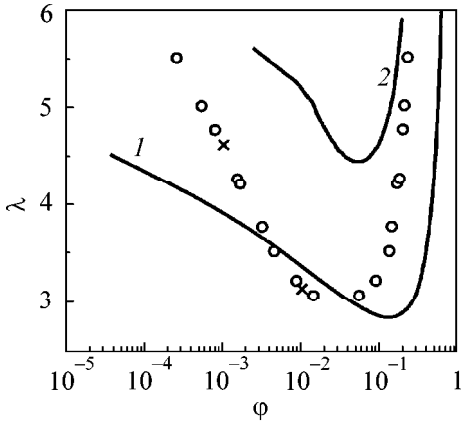

Fig. 3. Phase diagram of a ferrocolloid. (*1*) Perturbation theory [9]; (*2*) mean-sphere model [8]; ○ numerical simulation for the mean particle concentration $\varphi = 0.03$; and × concentration of saturated vapor, as determined upon modeling the particle concentration.

system are illustrated in Fig. 1, where the concentration of the dense phase is plotted as a function of the microstate number t. The upper curve corresponds to the case where the initial particle concentration in the condensed phase was larger than the equilibrium concentration ($\varphi_c(0) > \varphi_{c0}$), and the lower curve is for $\varphi_c(0) < \varphi_{c0}$. One can see from Fig. 1 that the equilibrium value φ_{c0} does not depend on the initial conditions. To reduce the influence of fluctuations and increase the accuracy of the calculated equilibrium concentration φ_{c0}, its value was determined from the $\varphi_c(t)$ curve by the exponential approximation of the calculated data.

The cylindrical shape of the simulated cell allows the formation of a plane phase interface. The density of the substance depends only on the coordinate along the cylinder axis. This removes the problem associated with the possible influence of interface curvature on the saturation vapor pressure. The equilibrium density is shown in Fig. 2 for two values of the aggregation parameter. The curves were obtained by averaging the data for 3×10^4 equilibrium microstates. The calculations showed that in all cases where the aggregation parameter was smaller than its critical value $\lambda^* = 3.0 \pm 0.1$ the initial drop in the middle of the cylinder was fully evaporated. After thermodynamic equilibrium was achieved, large density fluctuations were observed in the system, but it became, on the whole, macroscopically homogeneous ($\lambda = 2.75$). At $\lambda > \lambda^*$, only a small fraction of the drop was evaporated, although its volume and density might change by 1.5– 2 times on the way to equilibrium. (As mentioned above, the density of the drop could both decrease and increase.) The system was separated into two phases with particle concentrations differing by several orders of magnitude. The interface between the two phases was easily visible at $\lambda = 3.75$. If the system was far from the critical point, the transition region ("interface width") covered several units. The interface became diffuse upon approaching the critical point and disappeared entirely at $\lambda < \lambda^*$.

The phase diagram obtained in this work is shown in Fig. 3 in φ, λ coordinates. As expected, the phase equilibrium curve has a minimum corresponding to the critical point $\lambda = \lambda^*$ and $\varphi = \varphi^* \approx 0.034$. The region inside the curve corresponds to the two-phase state; the left part of the diagram corresponds to the gas state, and the right part to the condensed state. The numerical results are qualitatively consistent with the predictions of perturbation theory (curve *1*) and the mean-sphere approximation (curve *2*). One can hardly expect a good quantitative agreement, because the aggregation parameters corresponding to the phase curve fall beyond the area of applicability of the analytical models. Nevertheless, it is worth noting that the perturbation theory provides better agreement with the numerical simulation near the critical point, while the mean-sphere model is more appropriate for large λ values.

In the second variant, the condensation process was simulated for the dipolar particles filling a sphere with

impenetrable boundaries. To overcome the problems associated with the formation of a large number of subsystems, the clusters were allowed to execute Brownian motion as individual kinetic units [22] and the system was exposed to a centrally directed "gravitational" field. The gravitational potential was chosen in such a way that it did not markedly affect the particles but promoted fast aggregation of the "fog" drops into a unified condensed subsystem. The effective volume V_{eff} calculated for the mean-square distance between the particles was chosen as the order parameter. For a system in mesoscale equilibrium, $V_{\text{eff}} = 1$; the V_{eff} value decreased jumpwise upon liquid layering. The position and shape of the interface were not tracked, but, on average, the system preserved the spherically symmetric configuration.

Since the second variant required much greater computer time, the computations were carried out only for two volume-averaged particle concentrations. The computations showed that the system is spatially homogeneous at $\lambda < 3$ ($V_{\text{eff}} \approx 1$). As the aggregation parameter increases, the effective volume tangibly (by approximately an order of magnitude) decreases: the systems transits to the two-phase state. The λ value corresponding to the phase transition was determined from the steepest portion of the $V_{\text{eff}} = f(\lambda)$ curve. These λ values are indicated by crosses in the phase diagram (Fig. 3). Figure 3 shows that the agreement between the results of the two different algorithms is very good. This signifies that the interface curvature is immaterial because of the extremely small surface tension coefficient. The estimations carried out for the droplike aggregates formed in magnetic fluids and containing at least several hundred particles confirm this conclusion.

This work was supported by the Federal Target Program "Integratsiya," project no. 99-04.

REFERENCES

1. C. F. Hayes, J. Colloid Interface Sci. **52**, 239 (1975).
2. E. A. Peterson and D. A. Krueger, J. Colloid Interface Sci. **62**, 24 (1977).
3. J. C. Bacri and D. Salin, J. Phys. Lett. **43**, L649 (1982).
4. V. V. Chekanov, V. I. Drozdova, P. V. Nutsubidze, *et al.*, Magn. Gidrodin., No. 1, 3 (1984).
5. A. F. Pshenichnikov and I. Yu. Shurubor, Izv. Akad. Nauk SSSR, Ser. Fiz. **51**, 1081 (1987).
6. A. O. Tsebers, Magn. Gidrodin., No. 2, 42 (1982).
7. K. Sano and M. Doi, J. Phys. Soc. Jpn. **52**, 2810 (1983).
8. K. I. Morozov, Izv. Akad. Nauk SSSR, Ser. Fiz. **51**, 1073 (1987).
9. A. Yu. Zubarev and A. O. Ivanov, Phys. Rev. E **55**, 7192 (1997).
10. A. F. Pshenichnikov, J. Magn. Magn. Mater. **145**, 319 (1995).
11. A. F. Pshenichnikov, V. V. Mekhonoshin, and A. V. Lebedev, J. Magn. Magn. Mater. **161**, 94 (1996).
12. R. P. Sear, Phys. Rev. Lett. **76**, 2310 (1996).
13. J. M. Tavares, M. M. Telo da Gama, and M. A. Osipov, Phys. Rev. E **56**, 6252 (1997).
14. Y. Levin, Phys. Rev. Lett. **83**, 1159 (1999).
15. J. M. Tavares, J. J. Weis, and M. M. Telo da Gama, Phys. Rev. E **59**, 4388 (1999).
16. J. J. Weis and D. Levesque, Phys. Rev. Lett. **71**, 2729 (1993).
17. D. Levesque and J. J. Weis, Phys. Rev. E **49**, 5131 (1994).
18. M. J. Stevens and G. S. Grest, Phys. Rev. E **51**, 5962 (1995).
19. M. J. Stevens and G. S. Grest, Phys. Rev. E **51**, 5976 (1995).
20. J. C. Shelley, G. N. Patey, D. Levesque, and J. J. Weis, Phys. Rev. E **59**, 3065 (1999).
21. P. J. Camp, J. C. Shelley, and G. N. Patey, Phys. Rev. Lett. **84**, 115 (2000).
22. A. F. Pshenichnikov and V. V. Mekhonoshin, J. Magn. Magn. Mater. **213**, 357 (2000).
23. *Monte Carlo Methods in Statistical Physics*, Ed. by K. Binder (Springer-Verlag, New York, 1979).

Translated by V. Sakun

JETP Letters, Vol. 72, No. 4, 2000, pp. 186–189. Translated from Pis'ma v Zhurnal Éksperimental'noĭ i Teoreticheskoĭ Fiziki, Vol. 72, No. 4, 2000, pp. 267–272.

Negative Interband Photoconductivity in Ge/Si Heterostructures with Quantum Dots of the Second Type

A. I. Yakimov, A. V. Dvurechenskiĭ, A. I. Nikiforov, and O. P. Pchelyakov

Institute of Semiconductor Physics, Siberian Division, Russian Academy of Sciences, pr. Akademika Lavrent'eva 13, Novosibirsk, 630090 Russia

e-mail: yakimov@isp.nsc.ru

Received July 7, 2000

It was found that irradiating an array of Ge nanoclusters in *n*-Si with light that induced interband transitions gave rise to negative photoconductivity. This result was explained by localization of equilibrium electrons at the Si/Ge interface in the potential of the nonequilibrium holes trapped on deep states in Ge islands. © *2000 MAIK "Nauka/Interperiodica".*

PACS numbers: 73.20.Mf; 73.50.Pz

Interest in studying photoelectric properties of assemblies of nanosized atomic clusters (quantum dots, QDs) obtained during the growth of mismatched heteroepitaxial systems via a Stranski–Krastanov process is due to new possibilities of creating efficient light-emitting devices and photodetectors [1, 2]. Arrays of Ge islands grown on Si(001) are a typical example of such a system.

Strained Ge/Si(001) layers represent heterostructures of the second type. The characteristic properties of systems of this class are determined by the relative positions of the band edges of the source semiconductors at the interface. The conduction band of one of the materials (Si) here is close to the valence band of the other (Ge), which causes spatial separation of carriers. In this case, holes are localized in Ge quantum dots, whereas there is a potential barrier for electrons in Ge. However, the positive charge generated by holes and the nonuniform structural deformation of the silicon islands surrounding Ge because of the mismatch of the Ge and Si lattice constants may give rise to potential wells for electrons at the Si/Ge interface. Self-consistent calculations of the energy spectrum of electrons and holes were carried out in [3] within the effective mass approximation for pyramidal Ge nanoclusters with a base length of 15 nm and a height of 1.5 nm. The calculations showed that the localization energy of holes in QDs is $E_{lh} \approx 400$ meV and the localization energy of electrons in Si at QDs is $E_{le} \approx 40$–70 meV (depending on the number of holes in the dot). The contribution to E_{le} from the deformation of the silicon matrix comprises only a small part (7 meV [3]); therefore, electrons can be localized at a QD at sufficiently high temperatures only when the QD is charged by a hole. In our opinion, in structures with *n*-type conductivity, this may lead to such a rare phenomenon as negative photoconductivity (PC). In the majority of real cases, the conductivity increases upon illumination (positive PC), because band-to-band illumination increases the concentration of free charge carriers.

Consider *n*-type silicon in which undoped Ge nanoclusters have been introduced (Fig. 1a). The dark conductivity of the system is determined by the free electrons in the Si conduction band. Upon absorption of light that induces interband transitions and generates electron–hole pairs, holes will start to accumulate in Ge QDs, charging them positively. As a result, potential wells for electrons will arise at the Si/Ge interfaces in silicon. If $E_{le} > E_D$, where E_D is the ionization energy of donor impurities in Si, these potential wells will behave like photoinduced electron attachment centers (Fig. 1b). The localization of electrons on these centers will decrease the concentration of mobile carriers and reduce the conductivity of the system.

To verify the above considerations, we investigated the photoconductivity of the Ge/Si epitaxial structure grown on a Si(001) substrate with the phosphorus concentration $N_s \approx 5 \times 10^{15}$ cm^{-3}. The substrate thickness was $L_s = 300$ μm. The structure consisted of ten layers of Ge islands separated by Si interlayers 30 nm thick. The total thickness of the epitaxial layer was $L_{epi} \approx 0.3$ μm. The concentration of donors (Sb) in the epitaxial Si layer was $N_{epi} \approx 2.5 \times 10^{16}$ cm^{-3}. The Ge nanoclusters were of a pyramidal shape with a base length of 15 nm and a height of 1.5 nm [4]. The layer density of nanoclusters in each layer was $n_{QD} \approx 3 \times 10^{11}$ cm^{-2}. A GaAs light-emitting diode with an emission maximum at a wavelength of ~ 0.9 μm was used as a light source. The emission intensity of the light-emitting diode was modulated with a frequency of 2 kHz. The photoconductivity was measured at the modulation frequency.

The dependences of the relative PC $\Delta G/G$ on the illumination power P for a Ge/Si structure with quan-

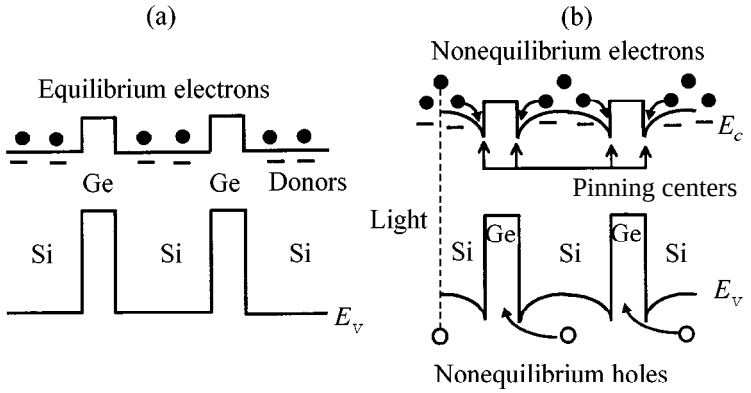

Fig. 1. Band structure of a multilayer *n*-type Ge/Si heterostructure with Ge quantum dots (a) in the absence of light and (b) under illumination. The figure illustrates the mechanism of negative interband photoconductivity (see text).

tum dots at various temperatures are shown in Fig. 2. The lux–ampere characteristic at $T = 77$ K for a sample containing no epitaxial layer with islands is also presented there (dashed line). The photoconductivity in the sample containing no quantum dots is positive and increases almost linearly with increasing P. The structure containing Ge nanoclusters exhibits negative PC in the range of illumination intensities $P = 0$–100 mW/cm^2. The effect of a decrease in photoconductivity upon illumination is suppressed with an increase in temperature, because the thermal energy kT at high T becomes of the order of the localization energy of electrons E_{le} and most of the electrons are no longer confined by the positive potential of the holes.

As the illumination intensity increases, a transition to positive PC is observed (at $P > 100$ mW/cm^2). We associate the change of the PC sign with the saturation of the number of electrons that can be localized in the potential of quantum dots charged by holes. The calculations given in [3] demonstrate that the third or the fourth electron is already displaced to the region of conduction-band delocalized states through the Coulomb interaction with the trapped electrons. Optical generation directly in Ge cannot markedly affect the filling of islands because of the small thickness of Ge. Note, however, that the diffusion length of nonequilibrium carriers in Si (100–1000 μm [5]) is much larger than the light penetration depth (~10 μm). Therefore, virtually all the photoexcited holes and electrons in Si can be trapped, diffusing from the bulk, on the bound states in the region of QDs. Then, taking into account that the interband recombination times of electrons and holes in Si and Ge nanoclusters are much the same [3], we obtain the average number of nonequilibrium holes and electrons per island $N_h = P\tau/h\nu n_{QD}N$, where τ is the interband recombination time, $h\nu$ is the photon energy, and N is the number of QD layers. For $\tau \sim 15$ μs, $h\nu = 1.4$ eV, $n_{QD} \approx 3 \times 10^{11}$ cm^{-2}, and $N = 10$, we actually obtain the degree of filling $N_h = 2.5$. This means that the potential wells in the silicon conduction band are already filled with electrons at an illumination intensity of ~ 100 mW/cm^2. Additional generation of nonequilibrium electrons will lead to growth of the concentration of free carriers. Therefore, the PC has a positive sign.

If the maximum number of bound electron states at each island equals two, a minimum of the photoconductivity is reached when each QD contains one nonequilibrium hole. In this case, both equilibrium and nonequilibrium electrons can be confined at a QD, thus making no contribution to the conductivity.

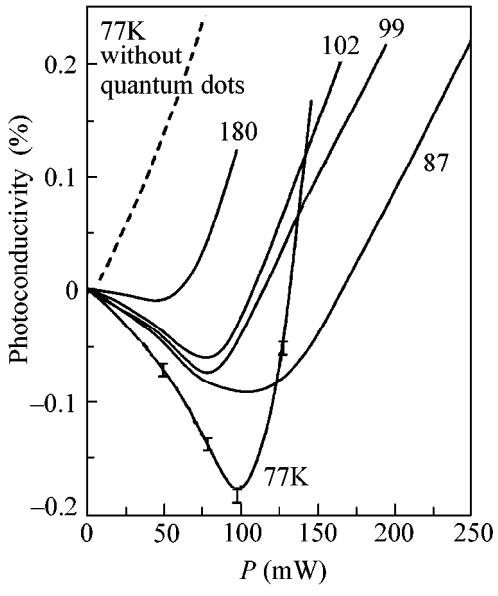

Fig. 2. Dependence of the relative photoconductivity on the interband illumination intensity in *n*-type Si with Ge quantum dots and in a sample without Ge nanoclusters at various temperatures. The light source is a GaAs light-emitting diode whose emission maximum corresponds to a photon wavelength of ~0.9 μm.

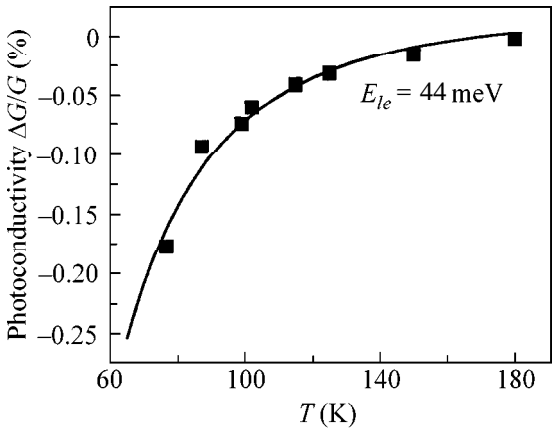

Fig. 3. Temperature dependence of the photoconductivity minimum. The solid line shows the result of approximating the experimental data (points) by Eq. (4) for the localization energy of electrons on the photoinduced attachment center E_{le} = 44 meV.

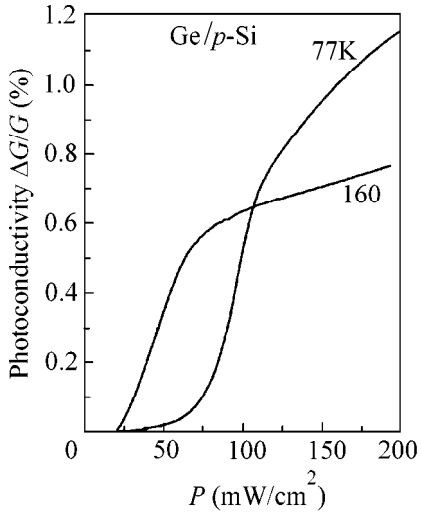

Fig. 4. Dependence of the relative photoconductivity on the interband illumination intensity in *p*-type Si with Ge quantum dots.

The expected value of negative PC can be estimated within a simple model. When photoinduced attachment centers appear at the interface of positively charged QDs, free electrons, on leaving Si, will start to quit the conduction process. Because the relationship $Nn_{\mathrm{QD}} > N_{epi}L_{epi}$ is fulfilled at the given parameters of the epitaxial Si layer (impurity concentration and thickness), part of the electrons will go out of the substrate to the layer with islands, leaving there a region of space charge of ionized donors with the width *w*. The value of *w* can be found from the electroneutrality condition

$$Nn_{\mathrm{QD}} = N_{epi}L_{epi} + N_s w. \tag{1}$$

The layer conductivity in the absence of illumination is determined by the equation

$$\begin{aligned} G &= e\mu_s N_s L_s \exp(-E_{\mathrm{P}}/kT) \\ &+ e\mu_{epi} N_{epi} L_{epi} \exp(-E_{\mathrm{Sb}}/kT), \end{aligned} \tag{2}$$

where μ_s is the electron mobility in the substrate, μ_{epi} is the electron mobility in the epitaxial Si layer, E_{P} is the ionization energy of the phosphorus level in the substrate, and E_{Sb} is the ionization energy of the antimony level in the epitaxial layer. The layer conductivity under illumination takes the form

$$\begin{aligned} G_{ph} &= e\mu_s N_s (L_s - w) \exp(-E_{\mathrm{P}}/kT) \\ &+ e\mu_{\mathrm{QD}} N n_{\mathrm{QD}} \exp(-E_{le}/kT), \end{aligned} \tag{3}$$

where μ_{QD} is the electron mobility at the Si/Ge interface. Assume for the estimations that all the mobilities μ_s, μ_{epi}, and μ_{QD} are equal to each other. Then the relative value of PC can be obtained from Eqs. (1), (2), and (3):

$$\begin{aligned} \frac{\Delta G}{G} &= -\left\{1 + \frac{Nn_{\mathrm{QD}}}{N_{epi}L_{epi}}\left[\exp\left(-\frac{E_{\mathrm{P}} - E_{\mathrm{Sb}}}{kT}\right)\right.\right. \\ &\left.\left. - \exp\left(-\frac{E_{le} - E_{\mathrm{Sb}}}{kT}\right)\right] - \exp\left(-\frac{E_{\mathrm{P}} - E_{\mathrm{Sb}}}{kT}\right)\right\} \\ &\times \left\{1 + \frac{N_s L_s}{N_{epi}L_{epi}} \exp\left(-\frac{E_{\mathrm{P}} - E_{\mathrm{Sb}}}{kT}\right)\right\}^{-1}. \end{aligned} \tag{4}$$

The points in Fig. 3 show the experimental temperature dependence of the minimum of the relative photoconductivity. The calculated curve obtained using Eq. (4) is also drawn there as a solid line. The electron energy on the attachment centers E_{le} was the only fitting parameter. For E_{P} = 45.2 meV and E_{Sb} = 42.5 meV [6], the least deviation of the calculated curve from the experimental data is reached at E_{le} = 44 meV. The self-consistent calculations [3] give the following values of E_{le} for various variants of QD filling: 38 meV for one electron in the potential of one hole, 70 meV for one electron in the potential of two holes, and 50 meV for the first of two electrons in the field of two holes. The experimental energy E_{le} falls within the same range and has quite a reasonable value. It is evident in Fig. 3 that the simple model reproduces well both the value and the temperature dependence of negative photoconductivity. However, the temperature and concentration dependence of the mobilities must be correctly taken into account for obtaining results that are more accurate.

As noted at the beginning, the appearance of an electron-localizing potential when holes are trapped in QDs is the crucial factor in the occurrence of negative PC. It is clear that illumination should not lead to a decrease in the concentration of equilibrium carriers in

the *p*-type structures. This is because the occurrence of a potential well in the Ge valence band is mainly determined by the discontinuity between the Ge and Si valence bands. However, the Coulomb interaction energy of an electron and a hole bound into a spatially indirect exciton (≈25 meV [3]) is much lower than the localization energy of a hole (~400 meV in the ground state).

The lux–ampere characteristics of a Ge/*p*-Si structure are presented in Fig. 4. The sample was grown under conditions similar to those for the synthesis of the Ge/*n*-Si sample, except for the conductivity type of the substrate and the upper epitaxial Si layer with Ge islands (the concentration of the acceptor boron impurity was $\approx 10^{15}$ cm^{-3} in the substrate and $\approx 10^{16}$ cm^{-3} in the epitaxial Si layer). It is clear that the region with negative PC is absent in the *p*-type structure. Instead, an extended region with low positive PC is observed, after which a step increase in the photocurrent occurs. This behavior at low illumination intensities is due to trapping of nonequilibrium carriers of both types on the bound states in the vicinity of Ge islands (holes on the states in Ge islands and electrons on the states at the Si/Ge interface). The growth of PC at high intensities is explained by filling of the electron levels and the appearance of free nonequilibrium electrons.

We emphasize in conclusion that the mechanism of negative photoconductivity proposed in this work is accomplished only in quantum dots of the second type, because both electrons and holes in heterostructures of the first type are localized in the same semiconductor independently of the charge state of QDs.

This work was supported by the Russian Foundation for Basic Research, project nos. 00-02-17885 and 00-02-17638, and by the scientific program "Physics of Solid-State Nanostructures," project no. 98-1100.

REFERENCES

1. N. N. Ledentsov, V. M. Ustinov, V. A. Shchukin, *et al.*, Fiz. Tekh. Poluprovodn. (St. Petersburg) **32**, 385 (1998) [Semiconductors **32**, 343 (1998)].
2. A. V. Dvurechenskiĭ and A. I. Yakimov, Izv. Vyssh. Uchebn. Zaved., Mater. Élektron. Tekh. **4**, 4 (1999).
3. A. I. Yakimov, A. V. Dvurechenskiĭ, N. P. Stepina, *et al.*, Zh. Éksp. Teor. Fiz. (in press) [JETP (in press)].
4. A. I. Yakimov, A. V. Dvurechenskii, Yu. Yu. Proskuryakov, *et al.*, Appl. Phys. Lett. **75**, 1413 (1999).
5. J. A. del Alamo, in *Properties of Silicon*, Ed. by T. H. Ning (INSPEC, Institute of Electrical Engineers, New York, 1988), p. 164.
6. V. L. Bonch-Bruevich and S. G. Kalashnikov, *Physics of Semiconductors* (Nauka, Moscow, 1977).

Translated by A. Bagatur'yants

JETP Letters, Vol. 72, No. 4, 2000, pp. 190–194. Translated from Pis'ma v Zhurnal Éksperimental'noĭ i Teoreticheskoĭ Fiziki, Vol. 72, No. 4, 2000, pp. 273–278.

Enhancement of the Nonlinear Acoustoelectric Interaction in a Photoexcited Plasma in a Quantum Well

A. V. Kalameĭtsev*, A. O. Govorov*, H.-J. Kutschera, and A. Wixforth****

** Institute of Semiconductor Physics, Siberian Division, Russian Academy of Sciences, pr. Akademika Lavrent'eva 13, Novosibirsk, 630090 Russia*

*** Sektion Physik der Ludwig-Maximilians-Universität and Center for NanoScience, Münich, D-80539 Germany*

Received July 12, 2000

Nonlinear interaction of an intense surface acoustic wave (SAW) with a 2D electron–hole plasma generated by light in a semiconductor quantum well near a piezoelectric crystal is investigated. It is shown that, in a strongly nonlinear regime, the acoustoelectric interaction is enhanced because of the accumulation of carriers in the field of an intense SAW. In addition, in a strongly nonlinear regime, the dissipation of the acoustic wave energy increases and the sound velocity decreases. These dependences fundamentally differ from those observed in a unipolar plasma. For high sound intensities, analytical results are obtained. © *2000 MAIK "Nauka/Interperiodica".*

PACS numbers: 73.20.Dx; 73.50.Rb

Surface acoustic waves offer good possibilities for studying of 2D electron systems [1] owing to the piezoelectric interaction. In recent years, the so-called hybrid structures have been developed [2]. A hybrid structure (Fig. 1) consists of a submicron thin film (A_3B_5) with an electron quantum well and a substrate made of a piezoelectric crystal ($LiNbO_3$). Such a system is a quasi-monolithic one, because the film is tightly bound to the piezoelectric crystal by the Van der Waals forces. For a surface acoustic wave (SAW) in a hybrid structure, the electromechanical coupling constant K^2_{eff} is two orders of magnitude greater than in conventional GaAlAs systems [2]. In a hybrid structure, the regime corresponding to nonlinear acoustoelectric interaction can be obtained in experiments. The experimental studies [3, 4] showed that the electron plasma (which was induced in the cited experiments by a metal gate) could be divided into strips in the piezoelectric field of a SAW.

In this paper, we theoretically investigate the nonlinear acoustoelectric interaction in a hybrid structure in the presence of laser illumination, which generates an electron–hole plasma at room temperature. In hybrid structures, the acoustoelectric interaction is mainly governed by the piezoelectric effect. In the presence of a high-intensity SAW, the mean carrier density increases and the plasma falls into electron and hole strips. As the sound intensity increases, the absorption of the SAW also increases and the SAW velocity shift due to plasma decreases. These dependences are related to a strong recombination nonlinearity. The behavior of a unipolar plasma in an intense acoustic wave is fundamentally different: the absorption of the acoustic wave saturates, and the sound velocity increases [3–6].

In piezoelectric crystals with mobile electrons, the nonlinearity of the acoustoelectric interaction may be of a concentration character [5–7] or may occur as a

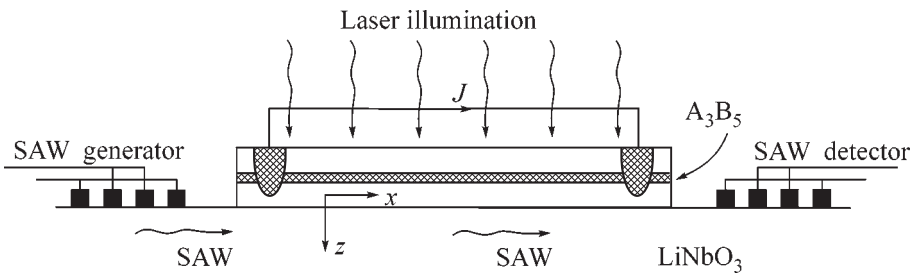

Fig. 1. Schematic diagram of a semiconductor–piezoelectric hybrid structure used for the experiments with SAW. The contacts to the 2D plasma are closed. The SAW can induce an acoustoelectric current *J* in the circuit.

0021-3640/00/7204-0190$20.00 © 2000 MAIK "Nauka/Interperiodica"

result of the capture of electrons by traps [8]. In this paper, we consider the combined effect of two mechanisms of nonlinearity, namely, the concentration mechanism and the recombination one. In our model, the recombination nonlinearity occurs in the case of the luminescence of mobile electron–hole pairs in a direct gap semiconductor and in the presence of permanent illumination. The recombination nonlinearity in some respect is similar to the nonlinearity due to traps, because it also leads to a change in the mean density of mobile carriers. However, there are some important differences. We note that, in the cited papers [8], the nonlinearity associated with traps was considered in the absence of illumination and for static traps. In our model, both electrons and holes are mobile. This fact plays a fundamental role, because the mobility leads to a spatial separation of the carriers in the field of an intense SAW.

In this paper, we consider the conventional case of weak acoustoelectric interaction between an intense SAW and the 2D plasma; i.e., we assume that $K_{\text{eff}}^2 \ll 1$. In addition, the sample is considered to be short in the sense that $\Gamma L < 1$ and long in the sense that $L \gg \lambda$. Here, Γ is the absorption coefficient for the SAW, L is the sample length, and λ is the wavelength. When the condition $\Gamma L < 1$ is valid, the contributions of higher harmonics of the SAW play a negligible role. To solve the problem in the framework of the aforementioned approximations, it is sufficient to determine the nonlinear response of the plasma to the piezoelectric potential of a monochromatic SAW. In the nonlinear regime, the SAW velocity shift due to the 2D plasma, δv_s, and the sound absorption coefficient Γ are determined by the expressions [4]

$$\frac{\delta v_s}{v_s^0} = \frac{\langle j\Phi^{SAW}\rangle}{2I}, \quad \Gamma = \frac{\langle jE_x^{SAW}\rangle}{I}, \tag{1}$$

where $\langle\ldots\rangle$ denotes spatial averaging, v_s^0 is the sound velocity in the absence of plasma, I is the SAW intensity, Φ^{SAW} is the piezoelectric potential of the SAW, E_x^{SAW} is the electric field induced by the SAW in the plane of the 2D plasma, and j is the current of the charge carriers. A SAW that propagates in the x direction generates an electric field $E_x^{SAW} = E_0\cos(qx - \omega t)$ and the corresponding piezoelectric potential $\Phi^{SAW} = -\Phi_0\sin(qx - \omega t)$, where $\Phi_0 = E_0/q$, t is time, q is the wave vector, and $\omega = v_s^0 q$. Since we assumed that $K_{\text{eff}}^2 \ll 1$, we have $\delta v_s \ll v_s^0$ and $\Gamma \ll q$.

The current $j = j_n + j_p$ is determined from the system of hydrodynamic equations

$$\begin{aligned} e\frac{\partial n}{\partial t} + \frac{\partial j_n}{\partial x} &= (G - Cnp)e, \\ |e|\frac{\partial p}{\partial t} + \frac{\partial j_p}{\partial x} &= (G - Cnp)|e|, \\ j_n = \sigma_n E_x - eD_n\frac{\partial n}{\partial x}, &\quad j_p = \sigma_p E_x - |e|D_p\frac{\partial p}{\partial x}, \end{aligned} \tag{2}$$

where n and p are the 2D electron and hole densities, respectively; j_n and j_p are the electron and hole currents; $e = -|e|$ is the electron charge; G is the rate of carrier generation by the laser light; C is the recombination constant; σ_n and σ_p are the electron and hole conductivities; and D_n and D_p are the electron and hole diffusion coefficients. Here, the following relations are valid: $\sigma_n = |e|\mu_n n$ and $\sigma_p = |e|\mu_p p$, where μ_n and μ_p are the electron and hole mobilities and $D_n/\mu_n = D_p/\mu_p = KT/|e|$, where T is temperature.

The electric field consists of two components: $\mathbf{E} = \mathbf{E}^{SAW} + \mathbf{E}^{ind}$. The field $\mathbf{E}^{ind}$ is induced by the plasma and determined from the Maxwell equation

$$\text{div}\mathbf{D}^{ind} = 4\pi(en + |e|p)\delta(z), \tag{3}$$

where $\mathbf{D}^{ind} = \hat{\epsilon}(z)\mathbf{E}^{ind}$ and z is normal to the system. The 2D plasma in the quantum well is modeled by the δ-function.

We will seek a steady-state periodic solution to the system of Eqs. (2) and (3) as a function of the coordinate $x' = x - v_s^0 t$. We note that, in our system with shorted contacts to the 2D plasma, we have $\langle E_x\rangle = 0$ (see Fig. 1) and the solution can be found in the form of a periodic function of x'. To determine the numerical solution, it is convenient to expand all functions in Eqs. (2) and (3) in Fourier series in the x' coordinate. Neglecting the thickness of the film, we obtain $\Phi_m^{ind} = 2\pi(en_m + |e|p_m)/\epsilon_{\text{eff}}|q_m|$, where Φ_m^{ind} represents the Fourier coefficients; $m = 0, \pm1, \pm2, \ldots$, $q_m = qm$; and $\epsilon_{\text{eff}} = (\epsilon + 1)/2$. Here, $\epsilon = \sqrt{\epsilon_{xx}^T\epsilon_{zz}^T}$ is the mean permittivity of $LiNbO_3$. The SAW intensity and the amplitude of the potential Φ_0 are related by the formula $K_{\text{eff}}^2 = (\sigma_m q/2)(\Phi_0^2/I)$, where $\sigma_m = \epsilon_{\text{eff}} v_s^0/2\pi$ [4]. The coefficient K_{eff}^2 was calculated earlier in the framework of the linear theory [2, 9].

The system of Eqs. (2) and (3) was solved numerically. The calculations were performed by using about 100 spatial harmonics and the following typical parameters of the system at $T = 300$ K: $\mu_e = 2 \times 10^3$ cm^2/(V s), $\mu_e/\mu_p = 6$, $v_s^0 = 3.9 \times 10^5$ cm/s, $\lambda = 60$ μm, $K_{\text{eff}}^2 =$

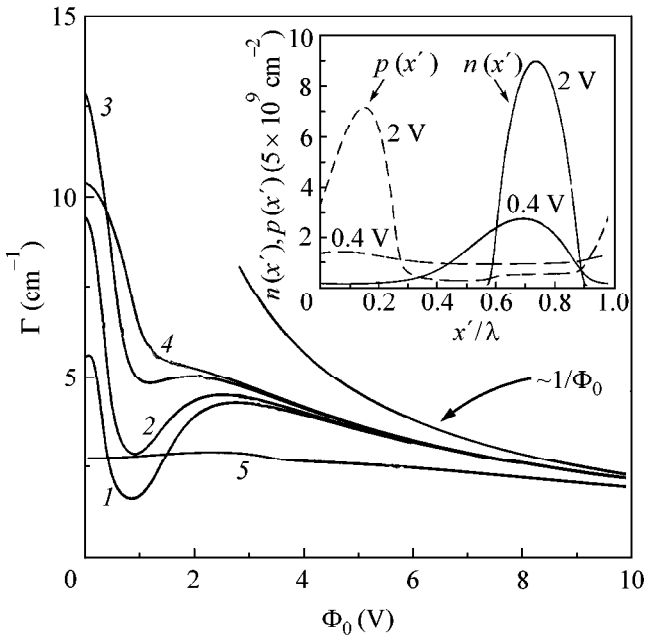

Fig. 2. Dependence of the sound absorption coefficient on the amplitude of the SAW potential. Curves *1–5* correspond to different intensities of optical pumping: $n_{s0} = 10^9$, 2×10^9, 5×10^9, 10^{10}, and 5×10^{10} cm^{-2}. The inset shows the profiles of the electron and hole concentrations for $n_{s0} = 5 \times 10^9$ cm^{-2} and for two different amplitudes $\Phi_0 = 0.4$ and 2 V.

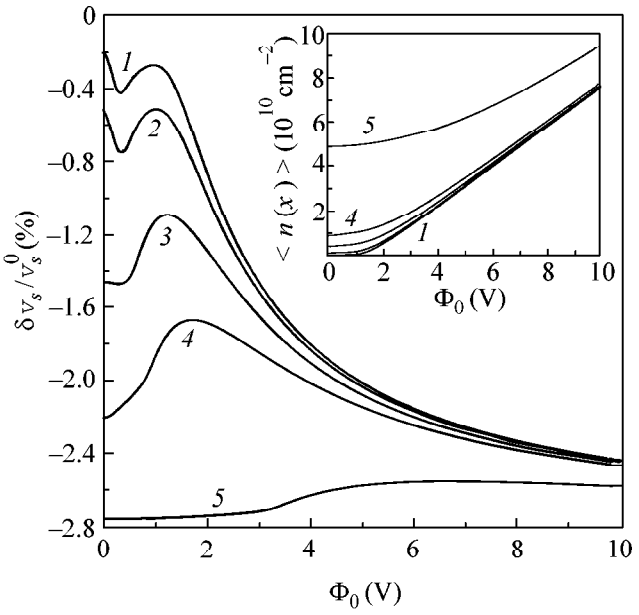

Fig. 3. Dependence of the SAW velocity shift on the SAW amplitude. The curves correspond to those in Fig. 2. The inset shows the dependence of the mean concentration on the SAW amplitude for different values of n_{s0}.

0.056, and $\epsilon = 50$. The recombination constant for nonequilibrium electrons and holes was estimated by a formula similar to Eq. (13) from [10]: $C = 4 \times 10^{-4}$ cm^2/s, which corresponds to the radiative recombination time $\tau_0^{rad} = 1/Cn_{s0} = 250$ ns for the electron and hole densities $n_{s0} = p_{s0} = 10^{10}$ cm^{-2}. At $\Phi_0 = 0$, the steady-state carrier concentrations were $n_{s0} = p_{s0} = \sqrt{G/C}$. The concentration n_{s0} was selected within the interval 10^9–10^{11} cm^{-2}, which is typical of optical experiments [10]. The corresponding luminous fluxes were within 10^{-2}–10^2 W/cm^2. The calculations were performed for the amplitudes of the potential $\Phi_0 \sim 1$–10 V. The amplitudes $\Phi_0 \sim 3$ V are typical of the experiments on hybrid structures with metallic gates [3, 4]. In these experiments, the input powers of SAW generation varied from –10 to 30 dB m [3, 4]. In this paper, we consider a gateless structure, for which the coefficient K_{eff}^2 should be greater.

The inset in Fig. 2 shows the calculated functions $n(x')$ and $p(x')$ for different values of Φ_0. One can see that, as Φ_0 increases, the plasma becomes separated into adjacent electron and hole strips. Electrons and holes tend to screen the potential $\Phi^{SAW}(x')$ at all x', but, simultaneously, the functions $n(x')$ and $p(x')$ slightly overlap. Only this type of carrier distribution can exist in a steady-state regime with a strong recombination nonlinearity, because the appearance of a noticeable gap between the strips should lead to a nonstationary accumulation of carriers. The absorption coefficient Γ (Fig. 2) mainly decreases with increasing Φ_0. The nonmonotonic behavior of Γ at $\Phi_0 \sim 1$–2 V correlates with the instant of noticeable separation of the plasma into strips and with the onset of the increase in the mean density $N_0 = \langle n(x') \rangle = \langle p(x') \rangle$ (the inset in Fig. 3). The increase in N_0 is a natural consequence of the spatial separation of electrons and holes and of the suppression of their recombination. When $\Phi_0 \longrightarrow \infty$, the sound absorption coefficient behaves as $\Gamma \propto 1/\Phi_0$ and the absorbed energy is $Q = I\Gamma \propto \Phi_0$. The increase in Q with growing sound intensity is related to the increase in the mean carrier density N_0 with $\Phi_0 \longrightarrow \infty$ (the inset in Fig. 3). Below, we will analytically derive the asymptotic expression for $Q(\Phi_0)$.

The calculations were also performed for the mean currents induced by the SAW. With increasing Φ_0, the current $\langle j_n(x') + j_p(x') \rangle$ first increased in magnitude and then decreased, because the carriers were trapped by the SAW. The mean velocities of electrons and holes tend to v_s^0 with $\Phi_0 \longrightarrow \infty$.

The velocity shift δv_s (Φ_0) shown in Fig. 3 exhibits a maximum at $\Phi_0 \sim 1$–2 V. This maximum is also related to the onset of plasma separation into strips. When $\Phi_0 \longrightarrow \infty$, the velocity shift δv_s decreases,

because the plasma becomes more and more dense and strongly screens the field of the SAW.

From the curves shown in the inset in Fig. 3, one can see that the transition to the nonlinear regime of carrier accumulation depends on the initial density $n_{s0} = p_{s0}$. The characteristic value of Φ_0 at which the density N_0 begins to grow increases with n_{s0}. The order of magnitude of this characteristic amplitude $\Phi_0^{non-lin}$ can be estimated in terms of the linear theory. Using the condition $\delta\rho_s \sim |e|n_{s0}$, where $\delta\rho_s$ is the perturbation of the 2D charge, we obtain $\Phi_0^{non-lin} \sim |e|n_{s0}\lambda/\epsilon_{\text{eff}}$. This estimate is valid on condition that $\sigma_0 > \sigma_m$, where $\sigma_0 = |e|(\mu_n + \mu_p)n_{s0}$. For $n_{s0} \sim 10^{10}$ cm^{-2}, we obtain $\Phi_0^{non-lin} \sim 2$V.

The asymptotic behavior of Γ and δv_s for $\Phi_0 \longrightarrow \infty$ can be obtained analytically from the following consideration. When $\Phi_0 \longrightarrow \infty$, the plasma screens the SAW field E_x^{SAW} at practically all points, and the density of 2D carriers can be determined from the simple integral equation $E_x = E_x^{ind}(x') + E_x^{SAW}(x') = 0$. In this case, the electrons screen half of the wave in the region where $e\Phi^{SAW} < 0$, and the holes screen half of the wave in the region where $e\Phi^{SAW} > 0$. From the condition $E_x = 0$, we obtain the asymptotic expression $N_0 \longrightarrow q\Phi_0\epsilon_{\text{eff}}/2\pi^2|e|$, which adequately describes the numerical data given in the inset in Fig. 3. According to the Drude model, the local absorption of the SAW by the plasma has the form

$$Q_{loc} = \frac{v_n^2 m_e^*}{\tau_n} n + \frac{v_p^2 m_h^*}{\tau_p} p,$$

where v_n and v_p are the velocities of electrons and holes, m_e^* and m_h^* are the electron and hole effective masses, and τ_n and τ_p are the corresponding relaxation times. Since the electrons and holes are almost totally trapped by the SAW and spatially separated, we have $v_n \simeq v_s^0$ for $\lambda/2 < x < \lambda$ and $v_p \simeq v_s^0$ for $0 < x < \lambda/2$. The total absorption now takes the form

$$\begin{aligned} Q = \langle Q_{loc} \rangle &\simeq (v_s^0)^2 N_0 \left(\frac{m_e^*}{\tau_n} + \frac{m_h^*}{\tau_p} \right) \\ &= (v_s^0)^2 N_0 |e| \left(\frac{1}{\mu_n} + \frac{1}{\mu_p} \right) \\ &= (v_s^0)^2 \left(\frac{1}{\mu_n} + \frac{1}{\mu_p} \right) q\Phi_0\epsilon_{\text{eff}}/2\pi^2. \end{aligned}$$

Thus, we derived the asymptotic expression $Q \propto N_0 \propto \Phi_0$ for $\Phi_0 \longrightarrow \infty$. The small parameters corresponding to $\Phi_0 \longrightarrow \infty$ are $v_s^0/\mu_n E_0 \ll 1$ and $v_s^0/\mu_p E_0 \ll 1$. To determine δv_s for $\Phi_0 \longrightarrow \infty$, we used similar small parameters and obtained the asymptotic expression $\delta v_s / v_s^0 \longrightarrow -K_{\text{eff}}^2/2$.

In the case of a unipolar plasma, which is induced, e.g., by the gate, the quantity $\langle n \rangle$ will evidently be constant for any Φ_0. When $\Phi_0 \longrightarrow \infty$, electrons form narrow strips and, on the whole, the screening of the SAW field is reduced. In the limit $\Phi_0 \longrightarrow \infty$, we have $Q \longrightarrow Q_{\max} = \langle n \rangle (v_s^0)^2 m_e^*/\tau_e$ and $\delta v_s \sim 1/\Phi_0 \longrightarrow 0$ [4–6].

The experimental studies of acoustoelectric interaction in 3D crystals in the presence of illumination were performed in the regime corresponding to hopping photoconduction and weak nonlinearity (see, e.g., [11]). The acoustoelectric interaction between the SAW and the photoexcited plasma in GaAs gave rise to a longitudinal voltage between the gates [12]. A strongly nonlinear acoustoelectric interaction in 2D systems was experimentally studied at $T = 4$ K in the exciton ionization regime [13, 14]. For example, a delay line for photons was realized in [13]: the incident photons were converted to electrons and holes and then carried along the sample by the SAW; at the final stage, the carriers generated secondary photons. At $T = 300$ K, an intense SAW was used to study a strongly nonuniform plasma excited in a quantum well by a laser beam [15]. One more class of experiments is related to the diffraction of light by volume and surface acoustic waves [16].

The predicted nonlinear acoustoelectric interaction applies to uniform illumination in an infinite sample. In a finite sample, the density accumulated in the potential wells of the SAW saturates when $\Phi_0 \longrightarrow \infty$. In our system, an intense SAW first separates the electrons and holes and then carries them along the sample. At the final stage, the carriers recombine as soon as they reach the right contact. In other words, an intense SAW "collects" the carriers over the whole sample length. The maximum density accumulated by SAW is equal to $N_{\max} = GL/v_s^0 = (L/v_s^0) n_0^2 C = n_0(t_0/\tau_0^{rad})$, where $t_0 = L/v_s^0$ is the time of SAW propagation over the sample length. Thus, in a finite system, each curve shown in the inset in Fig. 3 is saturated at its own level $N_{\max}(n_0)$. The described enhancement of the acoustoelectric interaction in the nonlinear regime manifests itself when $N_{\max} > n_0$. The latter inequality is equivalent to $t_0 > \tau_0^{rad}$. These inequalities hold for the typical parameters of our problem. For example, when $n_0 = 10^{10}$ cm^{-2} and $L = 2$ mm, we obtain $t_0/\tau_0^{rad} \sim 2$.

We are grateful to A.V. Chaplik and J.P. Kotthaus for useful discussions. The work was supported by the Volkswagen-Stiftung, the Russian Foundation for Basic Research (project nos. 99-02-17019 and 99-02-17127), and the State program "Physics of Solid-state Nanostructures."

REFERENCES

1. A. Wixforth, J. Scribe, M. Wassermeier, *et al.*, Phys. Rev. B **40**, 7874 (1989); R. L. Willett, R. R. Ruel, K. W. West, and L. N. Pfeiffer, Phys. Rev. Lett. **71**, 3846 (1993); I. L. Drichko, A. M. D'yakonov, V. D. Kagan, *et al.*, Fiz. Tekh. Poluprovodn. (St. Petersburg) **31**, 451 (1997) [Semiconductors **31**, 384 (1997)].
2. M. Rotter, A. Wixforth, W. Ruile, *et al.*, Appl. Phys. Lett. **73**, 2128 (1998).
3. M. Rotter, A. V. Kalameitsev, A. O. Govorov, *et al.*, Phys. Rev. Lett. **82**, 2171 (1999); M. Rotter, A. Wixforth, A. O. Govorov, *et al.*, Appl. Phys. Lett. **75**, 965 (1999).
4. A. O. Govorov, A. V. Kalameitsev, M. Rotter, *et al.*, Phys. Rev. B **62**, 2659 (2000).
5. V. L. Gurevich and B. D. Laĭkhtman, Zh. Éksp. Teor. Fiz. **46**, 598 (1964) [Sov. Phys. JETP **19**, 407 (1964)].
6. Yu. V. Gulyaev, Fiz. Tverd. Tela (Leningrad) **12**, 415 (1970) [Sov. Phys. Solid State **12**, 328 (1970)].
7. P. K. Tien, Phys. Rev. **171**, 970 (1968); P. N. Butcher and N. R. Ogg, J. Phys. D, Ser. 2 **2**, 333 (1969).
8. Yu. V. Gulyaev, Fiz. Tekh. Poluprovodn. (Leningrad) **2**, 628 (1968) [Sov. Phys. Semicond. **2**, 525 (1968)]; R. Katilyus, Fiz. Tverd. Tela (Leningrad) **10**, 458 (1968) [Sov. Phys. Solid State **10**, 359 (1968)].
9. K. A. Ingebrigtsen, J. Appl. Phys. **41**, 454 (1970); A. V. Chaplik, Pis'ma Zh. Tekh. Fiz. **10**, 1385 (1984) [Sov. Tech. Phys. Lett. **10**, 584 (1984)].
10. L. V. Kulik, A. I. Tartakovskiĭ, A. V. Larionov, *et al.*, Zh. Éksp. Teor. Fiz. **112**, 353 (1997) [JETP **85**, 195 (1997)].
11. E. M. Ganapol'skiĭ and V. V. Tarakanov, Fiz. Tverd. Tela (Leningrad) **14**, 487 (1972) [Sov. Phys. Solid State **14**, 583 (1972)]; Yu. M. Gal'perin, I. L. Drichko, and D. V. Shamshur, Fiz. Tverd. Tela (Leningrad) **32**, 2579 (1990) [Sov. Phys. Solid State **32**, 1498 (1990)].
12. V. A. V'yun, V. V. Pnev, A. V. Tsarev, and I. V. Yakovkin, Pis'ma Zh. Tekh. Fiz. **18** (7), 34 (1992) [Sov. Tech. Phys. Lett. **18**, 219 (1992)].
13. C. Rocke, S. Zimmermann, A. Wixforth, and J. P. Kotthaus, Phys. Rev. Lett. **78**, 4099 (1997).
14. C. Rocke, A. O. Govorov, A. Wixforth, *et al.*, Phys. Rev. B **57**, R6850 (1998).
15. M. Streibl, A. Wixforth, J. P. Kotthaus, *et al.*, Appl. Phys. Lett. **75**, 4139 (1999).
16. Yu. V. Gulyaev, V. V. Proklov, and G. N. Shkerdin, Usp. Fiz. Nauk **124**, 61 (1978) [Sov. Phys. Usp. **21**, 29 (1978)]; M. K. Balakirev, S. V. Bogdanov, and L. A. Fedyukhin, Zh. Tekh. Fiz. **50**, 2439 (1980) [Sov. Phys. Tech. Phys. **25**, 1421 (1980)].

Translated by E. Golyamina

JETP Letters, Vol. 72, No. 4, 2000, pp. 195–198. Translated from Pis'ma v Zhurnal Éksperimental'noĭ i Teoreticheskoĭ Fiziki, Vol. 72, No. 4, 2000, pp. 279–284.

Anharmonicity of Short-Wavelength Acoustic Phonons in Silicon at High Temperatures

V. V. Brazhkin*, S. G. Lyapin, I. A. Trojan*, R. N. Voloshin*, A. G. Lyapin*, and N. N. Mel'nik*****

** Institute of High-Pressure Physics, Russian Academy of Sciences, Troitsk, Moscow region, 142092 Russia*
*** Clarendon Laboratory, Physics Department, University of Oxford, Oxford OX1 3PU, England*
**** Lebedev Institute of Physics, Russian Academy of Sciences, Leninskiĭ pr. 53, Moscow, 117924 Russia*
Received July 13, 2000

Second-order Raman spectra corresponding to transverse acoustic phonons are studied in detail for crystalline Si over the temperature range 20–620°C. The largest relative softening and anharmonicity at the boundaries of the Brillouin zone were observed for the TA(*X*) mode. Extrapolation of the TA(*X*) frequency to high temperatures suggests that the Si lattice should be dynamically unstable at temperatures on the order of a doubled melting temperature. It is found that the main contribution to the softening of the transverse acoustic phonons in silicon comes from the anharmonicity and not from the volume expansion. *© 2000 MAIK "Nauka/Interperiodica".*

PACS numbers: 63.20.Ry

1. With an increase in the vibrational amplitudes of atoms in crystals, one should go beyond the well-known harmonic approximation [1, 2] and take into account the anharmonic terms in the expansion of potential energy of the crystal in powers of atomic deviations from equilibrium positions. The inclusion of anharmonicity is particularly important if the vibrational amplitudes or certain vibrational modes (soft modes) become comparable with the interatomic distance, e.g., in quantum crystals, near the melting temperature, or at structural phase transitions. In spite of the impressive progress in the theoretical description of strongly anharmonic crystals (see [3–5] and references therein), the problem of taking rigorous account of the anharmonicity in the phase-transition region, e.g., at the melting point or upon the approach of the instability point of the crystal lattice, is still far from being resolved. It is worth noting that the interrelation between the melting, the lattice instability caused by an increase in the thermal vibrations of atoms, and the anharmonicity of interatomic interaction was pointed out in a number of works [4–7].

Experimentally, direct information on crystal anharmonicity can be gained from the temperature dependences of some quantities such as interatomic distances, elastic constants, and phonon frequencies at high-symmetry points. In studying the vibrational modes, the anharmonicity can be analyzed most simply on the basis of the well-known thermodynamic relation [8]

$$\left(\frac{\partial \nu}{\partial T}\right)_P = \left(\frac{\partial \nu}{\partial T}\right)_V - \frac{\alpha}{\beta}\left(\frac{\partial \nu}{\partial P}\right)_T, \qquad (1)$$

where the phonon frequency variation with temperature at a constant pressure incorporates two parts corresponding to the purely anharmonic contribution at a constant volume and the quasi-harmonic contribution due to thermal expansion; α is the coefficient of volume expansion and β is the isothermal compressibility. This relation was previously applied to a series of molecular and ionic crystals [9], and it was found that the quasi-harmonic part, i.e., the thermal expansion, made the main contribution to phonon softening.

In this work, crystalline silicon was chosen as a subject of investigation because it is one of the most prominent representatives of the covalent tetrahedral semiconductors. Interest in the lattice dynamics of the tetrahedral semiconductors is caused by some of its unusual properties, such as a negative coefficient of volume expansion at low temperatures and negative Grüneisen parameters (and, accordingly, negative frequency derivatives with respect to pressure) of the transverse acoustic phonons [9]. It is also known that the tetrahedral semiconductors are related to the substances with the so-called "anomalous" melting: their density increases upon the crystal–liquid transition, because the atoms in the corresponding melts are packed more densely than in the crystals [10]. As distinct from the majority of crystals, the melting temperature of these substances decreases with pressure, in accordance with the Clausius–Clapeyron equation. It is also worth noting that in the majority of substances (metals, alkali halide crystals, or solid rare gases) the elastic constants and acoustic phonon frequencies undergo softening by 20–50% upon melting [11–13], whereas the elastic constants and the optical phonon frequencies in the tet-

0021-3640/00/7204-0195$20.00

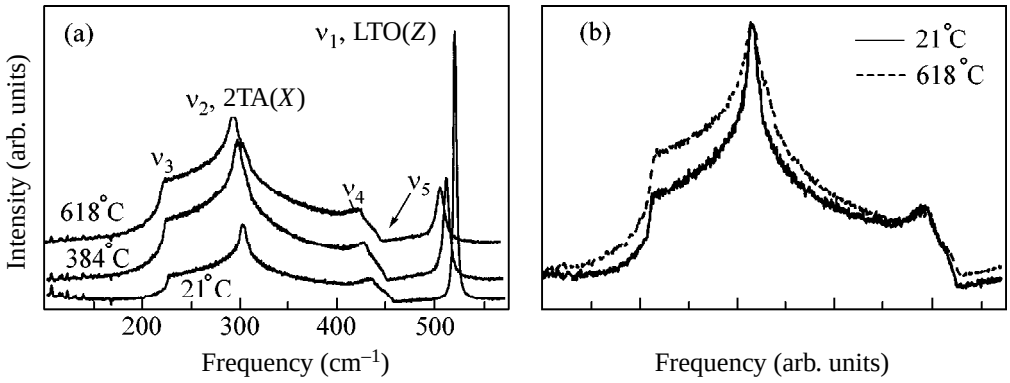

Fig. 1. (a) Temperature-dependent second-order Raman spectra due to the transverse acoustic phonons of Si, together with the main first-order line of the optical LTO(*Z*) mode. Numerical analysis and assignment (according to [9, 19]) of the characteristic features in the spectra are presented in the table. For convenience, the spectra are shifted along the vertical axis. (b) Temperature-dependent shape of the two-phonon spectrum. The curves are shifted along the frequency axis and normalized, in order to bring into coincidence the maxima corresponding to the 2TA(*X*) mode.

rahedral semiconductors soften by only 5–10% at the melting temperature [13].

These unusual properties of tetrahedral semiconductors no doubt are associated with the anharmonicity of interatomic interactions and special features of their phonon spectra. Nevertheless, detailed information on the anharmonicity of different phonon modes over a wide temperature range is, in great part, lacking for the system of interest. Only a few attempts were made to carry out a comparative analysis of the different contributions to phonon softening in semiconductors, specifically in the tetrahedral ones [8, 14].

The anharmonicity of the short-wavelength transverse acoustic phonons of the diamond-like Si lattice at the boundaries of its Brillouin zone are probably of particular interest, because it is these modes that are responsible, e.g., for the pressure-induced instability of the diamond-like lattices [15]. It should also be noted that the longitudinal acoustic modes at the boundaries of the Brillouin zone in Si are energetically close to the longitudinal optical modes and lie considerably higher than the transverse acoustic modes [9]. Earlier, attempts were undertaken to investigate the temperature dependences of phonon frequencies at the boundaries of the Brillouin zone in tetrahedral semiconductors by inelastic neutron scattering, e.g., in Ge [8], or using the data on the two-phonon line shifts in the second-order Raman spectra of Si [16]. However, only the temperature coefficients were determined for the phonon frequencies in these measurements. The anharmonic effects in Si were measured only for the optical phonons at the center of the Brillouin zone [17]. The purpose of this work was a detailed study of the anharmonicity of transverse acoustic phonons in Si at high temperatures by measuring the second-order Raman spectra.

2. A sample was heated in a vacuum furnace with continuous evacuation and resistive heating. The temperature was measured to within ±1 K by a chromel–alumel thermocouple placed near the sample. The Raman spectra were recorded in the geometry of backscattering from the (001) surface of a Si single crystal by a Jobin-Yvon T64000 Raman triple spectrometer with a nitrogen-cooled multichannel CCD detector. The 488 nm Ar^+ laser line was used for excitation. The spectra were measured in the $Z(XX)\bar{Z}$ and $Z(XY)\bar{Z}$ polarizations with a resolution of 0.5 cm^{-1}.

3. The Raman spectra of silicon are shown in Fig. 1. The second-order spectra reflect the phonon density of states. The calculations by the formulas relating the density of states to the shapes of Raman spectra [18] have shown that the anomalous points (Fig. 1 and table) in the spectrum are shifted from their true positions corresponding to the density of states by no more than 0.5%. On heating, all phonon frequencies go down, with the greatest effect (as regards both the amplitude and the rate of buildup of the negative derivative) being observed for the transverse acoustic (TA) phonons at the boundary point *X* of the Brillouin zone (Fig. 2). The accuracy of measurement was high enough for a substantial nonlinearity to be revealed in the temperature dependence of the frequencies, primarily for the TA(*X*) mode. The heating leads to a change not only of the characteristic frequencies, but also of the spectrum shapes (Fig. 1b), likely indicating the anharmonicity-induced changes in the phonon density of states [9].

Different contributions to the temperature coefficients [see Eq. (1)] obtained in our experiments for some phonon frequencies of the Si lattice are presented in the table. The quasi-harmonic contribution to the temperature derivatives is relatively small and comprises 5–30%. For the acoustic phonons, the quasi-harmonic contribution has the opposite sign, because they behave anomalously in the tetrahedral semiconductors under pressure: the frequencies of acoustic modes decrease upon compression [8, 9, 19, 21]. Thus, the

Temperature-dependent frequencies of the optical mode ν_1 in the first-order Raman spectrum and of the characteristic features (ν_2–ν_5) in the two-phonon spectra shown in Fig. 1, the temperature derivatives of the logarithms of these frequencies, and the decomposition of the derivatives into the anharmonic and quasi-harmonic components. The $(\partial \ln \nu/\partial P)_T$ values are taken from [9, 19], and α and β are from [20]

	T (°C)	ν (cm^{-1}) ±0.5	$\left(\frac{\partial \ln \nu}{\partial T}\right)_P$ (10^{-5} K^{-1})	$\left(\frac{\partial \ln \nu}{\partial T}\right)_V$ (10^{-5} K^{-1})	$-\frac{\alpha}{\beta}\left(\frac{\partial \ln \nu}{\partial P}\right)_T$ (10^{-5} K^{-1})
ν_1, LTO(Z)	21	521.4	–4.28	–3.51	–0.77
	320	514.1	–5.04	–3.95	–1.09
	618	505.9	–5.79	–4.37	–1.42
ν_2, 2TA(X)	21	303.4	–3.39	–4.71	1.32
	320	299.3	–5.71	–7.58	1.87
	618	293.4	–8.01	–10.46	2.45
ν_3, 2TA(L)	21	228.4	–4.20	–4.86	0.66
	320	225.1	–4.98	–5.95	0.97
	618	221.5	–5.78	–7.04	1.26
ν_4, 2TA(W)	21	436.2	–4.42	–4.54	0.12
	320	430.1	–4.86	–5.05	0.19
	618	423.7	–5.29	–5.52	0.23
ν_5, 2A(Σ, 2), 2A($L-K$, 2)	21	459.3	–2.87	–2.96	0.09
	320	454.0	–4.85	–4.98	0.13
	618	446.3	–6.74	–6.9	0.16

crystal lattice of Si exhibits strongly anharmonic behavior on heating.

4. The data obtained can be used to analyze the temperature-induced instability of the Si lattice in more detail and, in this connection, to touch on the melting problem. As is known, crystals may be heated over the equilibrium melting temperature for a short time [22], but the overheating is bounded by the stability loss line [11, 13] corresponding to the zero frequencies of certain lattice eigenmodes [1]. However, in the presence of a strong lattice anharmonicity, the phonon modes responsible for the lattice instability likely soften not to zero but to certain finite values (of the order of 40–60% of the initial frequencies) [4–7], with the derivatives of the corresponding frequencies (or elastic constants) turning to infinity at the instability point.

On normal melting, the short-range order is retained, while the long-range order is destroyed, so that, on a further increase in temperature, the structure of the liquid becomes stable against the softening of the long-wavelength acoustic phonons. The fact that the short-range order in the tetrahedral semiconductors alters upon "anomalous" melting suggests that the short-wavelength phonons, primarily the acoustic

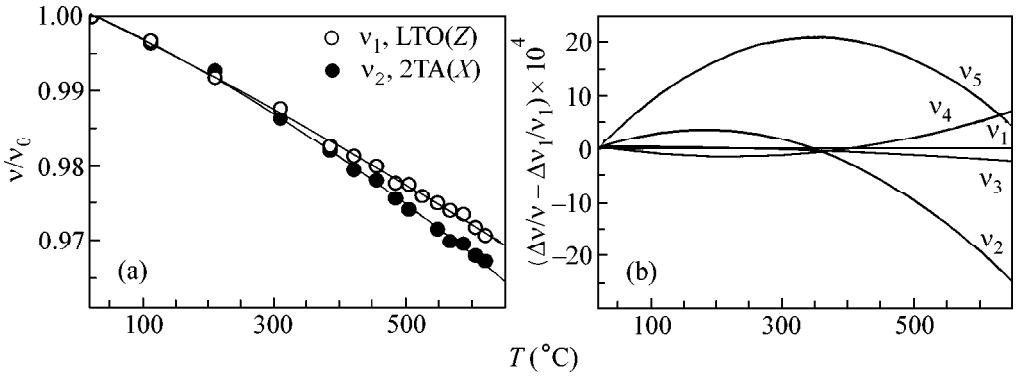

Fig. 2. Temperature-dependent frequencies of the characteristic features in the spectra of Si shown in Fig. 1: (a) fractional changes for the LTO(Z) and 2TA(X) modes; (b) fractional frequency changes after subtracting the $\Delta\nu_1/\nu_1(T)$ curve. Symbols correspond to the experimental points, and lines are the interpolations.

phonons near the boundaries of the Brillouin zone, play an important part in the lattice decomposition. The maximum values observed for the softening and anharmonicity of the TA(X) mode on heating support this assumption.

Extrapolation of the TA(X) frequency to the melting temperature at normal pressure (T_m = 1688 K) gives a value of $\Delta\nu/\nu \sim 0.11$–0.12 for the softening, whereas the corresponding value for the optical mode in the center of the Brillouin zone is $\Delta\nu/\nu \sim 0.07$. For the conventional stability-loss temperature defined by the condition $\Delta\nu/\nu \sim 0.5$, one obtains $T^* \sim 2T_m$. Taking into account the anharmonicity of the TA(X) mode (Fig. 2) and the fact that the derivative of the $\nu(T)$ function at the stability-loss point is likely infinite [4, 5, 7], one can expect a stronger softening for the acoustic phonons above the melting point and the loss of dynamic stability of the Si lattice at even lower temperatures.

Thus, the melting and heating-induced instability of Si are caused by softening of the short-wavelength acoustic phonons. The strong anharmonicity and the anomalous softening of the acoustic branches at the boundaries of the Brillouin zone are due to a profound contribution of the noncentral forces to the interatomic interactions in tetrahedral covalent crystals [9, 15].

It is pertinent to draw a certain analogy between anomalous melting and solid-state amorphization. Solid-phase amorphization (SPA) of crystals occurs upon changing pressure at rather low temperatures and is accompanied by the reorganization of the short-range order. There are grounds to believe that SPA is also associated with the softening of the short-wavelength acoustic phonons [13, 15] and that the contribution of noncentral forces is likely also essential to the SPA mechanism [15].

For a more detailed study of phonon anharmonicity and the mechanism of anomalous melting of the tetrahedral semiconductors, precise measurements need to be carried out for the phonon spectra up to the melting points of the relevant materials.

We are grateful to S.M. Stishov and S.V. Popova for fruitful discussions. This work was supported by the Russian Foundation for Basic Research, project no. 98-02-16325.

REFERENCES

1. M. Born and K. Huang, *Dynamical Theory of Crystal Lattices* (Oxford Univ. Press, Oxford, 1954).
2. A. A. Maradudin, E. W. Montroll, and G. H. Weiss, *Theory of Lattice Dynamics in the Harmonic Approximation* (Academic, New York, 1963).
3. P. Z. Zyryanov, V. V. Kondrat'ev, and I. G. Kuleev, Fiz. Met. Metalloved. **35**, 233 (1973).
4. N. M. Plakida, Fiz. Tverd. Tela (Leningrad) **11**, 700 (1969) [Sov. Phys. Solid State **11**, 561 (1969)].
5. N. M. Plakida and T. Siklós, Phys. Status Solidi **39**, 171 (1970).
6. Y. Ida, Phys. Rev. **187**, 951 (1969).
7. K. Ishizaki, P. Bolsaitis, and I. L. Spain, Phys. Rev. B **7**, 5412 (1973).
8. G. Nelin and G. Nilsson, Phys. Rev. B **10**, 612 (1974).
9. B. A. Weinstein and R. Zallen, in *Light Scattering in Solids*, Ed. by M. Cardona and G. Cuntherrodt (Springer-Verlag, Berlin, 1984), Part IV.
10. S. M. Stishov, Usp. Fiz. Nauk **96**, 467 (1968) [Sov. Phys. Usp. **11**, 816 (1969)].
11. A. R. Ubbelohde, *The Molten State of Matter* (Wiley, New York, 1978; Metallurgiya, Moscow, 1982).
12. V. G. Vaks, S. P. Kravchuk, and A. V. Trefilov, J. Phys. F **10**, 2105 (1980).
13. V. V. Brazhkin and A. G. Lyapin, High Press. Res. **15**, 9 (1996).
14. H. D. Hochheimer, M. L. Shand, J. E. Potts, *et al.*, Phys. Rev. B **14**, 4630 (1976).
15. A. G. Lyapin and V. V. Brazhkin, Phys. Rev. B **54**, 12036 (1996).
16. R. Tsu and J. G. Hernandez, Appl. Phys. Lett. **41**, 1016 (1982).
17. M. Balkanski, R. F. Wallis, and E. Haro, Phys. Rev. B **28**, 1928 (1983).
18. G. A. N. Connell, Phys. Status Solidi B **69**, 9 (1975).
19. B. A. Weinstein and G. I. Piermarini, Phys. Rev. B **12**, 1172 (1972).
20. M. E. Drits, *Handbook of Properties of Elements* (Metallurgiya, Moscow, 1985).
21. S. Klotz, J. M. Besson, M. Braden, *et al.*, Phys. Rev. Lett. **79**, 1313 (1997).
22. R. W. Cahn, Nature **323**, 668 (1986).

Translated by V. Sakun

JETP Letters, Vol. 72, No. 4, 2000, pp. 199–201. From Pis'ma v Zhurnal Éksperimental'noĭ i Teoreticheskoĭ Fiziki, Vol. 72, No. 4, 2000, pp. 285–288.

Zero Modes for Dirac Fermions on a Sphere with Fractional Vortex[1]

V. A. Osipov and E. A. Kochetov

Joint Institute for Nuclear Research, Bogoliubov Laboratory of Theoretical Physics, Dubna, Moscow region, 141980 Russia

e-mail: osipov@thsun1.jinr.ru

e-mail: kochetov@thsun1.jinr.ru

Received July 7, 2000; in final form, July 13, 2000

Normalized zero-energy states are shown to emerge for massless Dirac fermions in an external gauge field that gives rise to nonquantized vortices on a sphere. A field-theory model is used to describe electronic states of a fullerene-like molecule. In particular, we predict the existence of exactly one zero-energy mode due to a disclination. For 60° disclination, the normalized electron density at zero energy is found to behave as $R^{-5/3}$, with R being the fullerene radius. © *2000 MAIK "Nauka/Interperiodica".*

PACS numbers: 71.20.Tx; 03.65.Pm; 73.61.Wp

In [1], the 3D space-time Dirac equation

$$i\gamma^{\mu}(\partial_{\mu} + ieA_{\mu})\psi = 0 \qquad (1)$$

for massless fermions in the presence of a magnetic field was found to yield $N - 1$ zero modes in the N-vortex background field. Zero modes for fermions in topologically nontrivial manifolds have been of current interest in both field theory and condensed matter physics. In particular, they play a major role in getting some insight into understanding anomalies [2] and charge fractionalization that results in unconventional charge-spin relations (e.g., the paramagnetism of charged fermions) [3] with some important implications for the physics of superfluid helium (see, e.g., review [4]). More recently, the importance of the fermion zero modes was discussed in the context of high-temperature chiral superconductors [5–7] and the fullerene molecules [8]. The last example is our main concern in this paper. As we show below, the problem of the local electronic structure of fullerene is closely related to Jackiw's consideration [1]. Indeed, it was shown within the effective-mass approximation [9] that the electronic spectrum of a graphite plane linearized around the corners of a hexagonal Brillouin zone coincides with that of Eq. (1) for $A_{\mu} = 0$. As a consequence, the field-theory models for Dirac fermions on a plane and sphere [8, 10] were invoked to describe the variously shaped carbon materials.

What is important is that disclinations appear as generic defects in closed carbon structures, fullerenes, and nanotubes. Actually, in accordance with Euler's theorem, these microcrystals can only be formed by having a total disclination of 4π. According to the geometry of the hexagonal network, this means the presence of twelve pentagons (60° disclinations) on the closed hexatic surface. In an attempt to describe the electronic spectrum of fullerenes in the presence of disclinations, in [8, 10], the Dirac equation on the surface of a sphere was studied, where lattice curving due to insertion of pentagons was mimicked by introducing an effective gauge field. Indeed, since fivefold rings being inserted into the honeycomb lattice induce frustration, Dirac spinors acquire a nontrivial phase when rotated around a pentagon. It was demonstrated in [8] that the rotation can be implemented by inserting a line of magnetic flux at each of the pentagons. The flux is selected in the form needed to satisfy the transformation properties. It was assumed that the flux has to be nonabelian with the only nonvanishing component, A_{ϕ}, around each puncture, so that the correct value of a phase $\exp(i\oint \mathbf{A})$ is achieved at $\Phi = \pi/2$. Thus, this picture implies the existence of a fictitious magnetic monopole inside the surface with a charge $g = (1/4\pi)\sum \Phi_i = N/8$, where N is the number of conical singularities on the surface. In the continuum approximation, the effect of the magnetic field is smoothed over the sphere by considering a monopole sitting at its center. This phenomenological model is then used for the description of the low-lying electronic levels of the fullerene molecule. In particular, the model predicts the existence of two zero modes with the monopole charges $g = 1/2$ and $g = 3/2$. Notice that a similar problem for an electron in a monopole field was used in studying anyons and the fractional quantum Hall effect on a sphere [11] in the nonrelativistic formulation.

[1] This article was submitted by the authors in English.

In the present paper, we suggest a more adequate continuum model to describe the electronic spectrum of a fullerene molecule. The distinctive feature of our approach is that both electrons and disclinations are considered to be located on the *surface* of a sphere. In other words, we will deal with vortices on a sphere instead of a monopole inside a sphere. In this case, the flux due to a disclination is abelian. Actually, we extend a self-consistent gauge model formulated recently for the description of disclinations on fluctuating elastic surfaces [12] to include fermionic fields.

The basic field equation for the $U(1)$ gauge field in a curved background reads

$$D_a F^{ab} = 0, \quad F^{ab} = \partial^a W^b - \partial^b W^a, \tag{2}$$

where covariant derivative $D_a := \partial_a + \Gamma_a$ includes the Levi–Civita (torsion-free, metric compatible) connection

$$\Gamma^b_{ac} := (\Gamma_a)^b_c = \frac{1}{2} g^{bd}\left(\frac{\partial g_{dc}}{\partial x^a} + \frac{\partial g_{ad}}{\partial x^c} - \frac{\partial g_{ac}}{\partial x^d}\right), \tag{3}$$

g_{ab} being the metric tensor on a certain Riemannian surface Σ. For a single disclination on an arbitrary elastic surface, a singular solution to Eq. (2) is found to be [12]

$$W^b = -\nu \varepsilon^{bc} D_c G(x, y), \tag{4}$$

where

$$D_a D^a G(x, y) = 2\pi \delta^2(x, y)/\sqrt{g}, \tag{5}$$

with $\varepsilon_{ab} = \sqrt{g}\,\epsilon_{ab}$ being the fully antisymmetric tensor on Σ and $\epsilon_{12} = -\epsilon_{21} = 1$. It should be mentioned that Eqs. (2) and (5) self-consistently describe a defect located on an arbitrary surface [12].

Metric tensor $g_{\mu\nu} = e^\alpha{}_\mu e^\beta{}_\nu \delta_{\alpha\beta}$, where $e_\alpha{}^\mu$ is the zweibein; $\alpha, \beta = \{1, 2\}$; and coordinate indices $\mu, \nu = \{x, y\}$. We employ the real projective coordinates on a sphere. Explicitly,

$$e^1_x = e^2_x = e^1_y = -e^2_y = \sqrt{2}R^2/(R^2 + x^2 + y^2),$$

where R is the radius of the sphere. Notice that $e^\mu{}_\alpha$ is the inverse of $e^\alpha{}_\mu$. In this case,

$$g_{xx} = g_{yy} = 4R^4/(R^2 + x^2 + y^2)^2, \quad g_{xy} = g_{yx} = 0. \tag{6}$$

From Eqs. (4) and (5), the following solution can be easily read off:

$$W_x = -\nu \partial_y G, \quad W_y = \nu \partial_x G, \qquad G = \log r, \quad r = \sqrt{x^2 + y^2}. \tag{7}$$

Locally, it corresponds to the topological vortex on a Euclidean plane, which confirms the observation that disclinations can be viewed as vortices in elastic media.

An elastic flow through a surface on a sphere is given by the circular integral

$$\frac{1}{2\pi}\oint \mathbf{W}\, d\mathbf{r} = \nu. \tag{8}$$

Generally, there are no restrictions on the value of the winding number ν apart from $\nu > -1$ for topological reasons. However, if we take into account the symmetry group of the underlying crystal lattice the possible values of ν become "quantized" in accordance with the group structure (e.g., $\nu = 1/6, 1/4, 1/3, \ldots$ for hexagonal lattice). Note that the elastic flux is characterized by the Frank vector $\boldsymbol{\omega}$, $|\boldsymbol{\omega}| = 2\pi\nu$, with ν being the Frank index. Thus, the elastic flux is "classical" in its origin; i.e., there is no quantization, as opposed to the magnetic vortex. In some physically interesting applications, however, vortices with a fractional winding number have already been considered (see, e.g., the discussion in [5]). Note also that a detailed theory of magnetic vortices on a sphere has been presented in [13].

The Dirac equation on a sphere takes the form

$$i\gamma^\alpha e_\alpha{}^\mu (\nabla_\mu + iW_\mu)\psi = E\psi, \tag{9}$$

where $\nabla_\mu = \partial_\mu + \Omega_\mu$, with Ω_μ being the spin connection, which is generally defined as

$$\Omega_\mu = -\frac{1}{8}\Gamma^\alpha{}_\mu{}^\beta [\gamma_\alpha, \gamma_\beta],$$

where $\Gamma^\alpha{}_\mu{}^\beta = e^\alpha{}_\nu D_\mu e^{\beta\nu}$. One can check that $\Omega_x = \Omega_y = 0$, so that the spin connection does not enter (9). In general, spin connection Ω_μ vanishes if $\dim \Sigma = 2$ [14].

In 2D, the Dirac matrices can be chosen to be the Pauli matrices $\gamma^1 = -\sigma^2$, $\gamma^2 = \sigma^1$. For massless fermions, σ^3 serves as a conjugation matrix, and the energy eigenmodes are symmetric about $E = 0$ ($\sigma^3\psi_E = \psi_{-E}$). We are interested in the zero-energy modes. Let us write down the wave function as $\psi_0 = \begin{pmatrix} u \\ v \end{pmatrix}$. Then (9) reduces to the pair

$$\begin{aligned} (\partial_x + i\partial_y)v - \nu[(\partial_x + i\partial_y)G]v &= 0, \\ (\partial_x - i\partial_y)u + \nu[(\partial_x - i\partial_y)G]u &= 0. \end{aligned} \tag{10}$$

The solution is obvious:

$$\begin{aligned} u &= \exp(-\nu G) g(x - iy), \\ v &= \exp(\nu G) f(x + iy), \end{aligned} \tag{11}$$

where $f(x + iy)$ and $g(x - iy)$ are arbitrary entire functions. One can construct self-conjugate solutions $\begin{pmatrix} u \\ 0 \end{pmatrix}$ and $\begin{pmatrix} 0 \\ v \end{pmatrix}$. For nonvanishing flux, either u or v are normalizable. In particular, for planar systems in a vortex magnetic field, f and g are considered to be any polynomial functions of the form $r^n e^{in\theta}$ with $n = 0, 1, \ldots, [\nu - 1]$, where the brackets indicate the integer part. In this case,

there are exactly $[\nu - 1]$ normalized zero energy states because of the fact that the $\nu \le 1$ mode cannot be normalized on a plane. As was mentioned by Jackiw [1], a mismatch between the value of the quantized flux and the number of zero modes may be removed, provided R^2 is compacted to a two-sphere, S^2. Another possible solution is to consider a sort of extended model to include coupling of fermions to a scalar field [15]. It is clear that on a sphere for $0 < |\nu| < 1$, which is of interest in this paper, one can expect only one isolated zero-energy bound state with $n = 0$.

In a nontrivial geometry, the measure factor $\sqrt{g}$ should be taken into account, which on a sphere yields

$$\int |\psi_0|^2 \sqrt{g}\, dx dy = \int_0^\infty \int_0^{2\pi} r^{-2|\nu|} \frac{2R^2}{R^2 + r^2} r\, dr d\theta = \frac{2\pi^2}{\sin \pi(1 - |\nu|)} R^{2(1-|\nu|)}, \quad 0 < |\nu| < 1. \tag{12}$$

As is seen from (12), the zero-energy mode cannot be normalized on a plane. Indeed, the planar case corresponds to the limit $R \longrightarrow \infty$, so that (12) diverges as $R^{2(1-|\nu|)}$. As a consequence, there are no localized zero-energy electronic states on disclinations in monolayer graphite. It should be emphasized that this conclusion agrees with the results of numerical calculations [16] where the local density of states at the Fermi level ($E = 0$) was found to be zero for the case of five- and seven-membered rings, which correspond to single disclinations of the 2D graphite. Notice that though the eigenvalue Eq. (9) acquires a weight for nonzero eigenvalues, the zero eigenvalues remain unchanged. This finding agrees with Jackiw's conjecture [1]. The measure, however, affects condition Eq. (12), resulting in a normalizable zero-energy wave function for fractional vortex on a sphere.

For a fullerene molecule, we thus predict the existence of only one zero-energy mode due to a disclination, since it has been possible to normalize only one of two self-conjugate solutions for any elastic flux with $0 < |\nu| < 1$. In accordance with Eq. (12) the expected electron density at zero energy behaves like $R^{-2(1-|\nu|)}$. In particular, for $\nu = 1/6$, the normalized electron density behaves as $R^{-5/3}$. It would be interesting to verify our conclusions in experiments with fullerene molecules.

To conclude, we have formulated a field theory model to describe electronic states of a fullerene-like molecule. The key point of our approach is to consider disclinations located directly on a sphere, rather than describe the system in a mean-field approach by placing a fictitious monopole in the centre of the sphere. The latter case [8, 10] is essentially the 3D one, which implies that a nonvanishing spin connection is to be added to the covariant derivative in the Dirac Eq. (9) and, as a consequence, two normalizable zero modes appear, in contrast to our result.

REFERENCES

1. R. Jackiw, Phys. Rev. D **29**, 2375 (1984).
2. R. Jackiw and C. Rebbi, Phys. Rev. D **16**, 1052 (1977).
3. R. Jackiw and J. R. Schrieffer, Nucl. Phys. B **190**, 253 (1981).
4. M. M. Salomaa and G. E. Volovik, Rev. Mod. Phys. **59**, 533 (1987).
5. G. E. Volovik, Pis'ma Zh. Éksp. Teor. Fiz. **63**, 802 (1996) [JETP Lett. **63**, 763 (1996)].
6. G. E. Volovik, JETP Lett. **70**, 609 (1999).
7. G. E. Volovik, JETP Lett. **70**, 792 (1999).
8. J. González, F. Guinea, and M. A. H. Vozmediano, Nucl. Phys. B **406**, 771 (1993).
9. D. P. DiVincenzo and E. J. Mele, Phys. Rev. B **29**, 1685 (1984).
10. J. González, F. Guinea, and M. A. H. Vozmediano, Phys. Rev. Lett. **69**, 172 (1992).
11. Dingping Li, Nucl. Phys. B **396**, 411 (1993).
12. E. A. Kochetov and V. A. Osipov, J. Phys. A: Math. Gen. **32**, 1961 (1999).
13. B. A. Ovrut and S. Tomas, Phys. Rev. D **43**, 1314 (1991).
14. M. Nakahara, *Geometry, Topology and Physics* (A. Hilger, New York, 1990).
15. R. Jackiw and P. Rossi, Nucl. Phys. B **190**, 681 (1981).
16. R. Tamura and M. Tsukada, Phys. Rev. B **49**, 7697 (1994).

JETP Letters, Vol. 72, No. 4, 2000, pp. 202–204. Translated from Pis'ma v Zhurnal Éksperimental'noĭ i Teoreticheskoĭ Fiziki, Vol. 72, No. 4, 2000, pp. 289–293.

Influence of Physisorbed Water Molecules on the Dynamics of Domain Wall in an Amorphous Ferromagnet

V. E. Zubov, A. D. Kudakov*, N. L. Levshin, and T. S. Fedulova

Moscow State University, Vorob'evy gory, Moscow, 119899 Russia

** e-mail: kudakov@adk.phys.msu.su*

Received June 20, 2000; in final form, July 17, 2000

It was found that physisorbed water molecules affect the near-surface dynamics of a 180° domain wall in an amorphous FeCuNbSiB ferromagnet. In the range of water vapor pressures 400–1300 Pa, the oscillating domain walls suffer enhanced damping in the near-surface region and reduce their relaxation frequency from 10 to 4 kHz. This effect is explained by the influence of surface magnetic defects arising due to the pressure produced by the clusters of physisorbed water molecules on the walls of micropores at the magnet surface.

PACS numbers: 75.60.Ch; 68.45.Da

The interrelation between the adsorption–desorption processes and magnetic properties of ferromagnets was repeatedly pointed out in the literature [1, 2]. Studies of the oscillations of the 180° domain walls (DWs) in filamentary iron single crystals (whiskers) with a perfect crystal structure in bulk and at their surface have shown [2] that the DW relaxation frequency in the near-surface region increases by more than an order of magnitude upon reducing the air pressure in a measurement cell from atmospheric (p = 100 kPa) to p = 1 kPa. This effect was explained by the interaction between the DWs and the magnetic defects arising upon the adsorption of air molecules, in particular, water molecules. At the above-mentioned pressures and at a relative humidity of 70%, the partial pressure of water vapor in air at room temperature is 1500 and 15 Pa, respectively. The density of lattice defects at the surface of iron whiskers is too small to influence the DW motion (for details, see [3, 4]).

The observation of a fine effect such as the influence of reversible adsorption on the DW mobility at room temperature is possible because of the extremely low DW coercive force in iron whiskers, where it is equal to ~0.1 A/m [4]. In the highest quality samples of magnetically soft amorphous magnets, the coercive forces approach these values. At the same time, amorphous magnets have a developed surface containing both macro- and microdefects; i.e., from the viewpoint of surface quality, amorphous samples are the exact opposite of whiskers.

In this work, the influence of the adsorption of water, oxygen, nitrogen, and argon molecules on the mobility of the 180° DW in an amorphous ferromagnetic tape was studied at room temperature. Tapes of the amorphous ferromagnet $Fe_{76.5}Cu_1Nb_3Si_{13.5}B_6$ were prepared by the spinning method. Prior to amorphization, the melt was subjected to special thermotemporal treatment in order to obtain a homogeneous equilibrium distribution of dopants and, as a result, improve the magnetically soft properties of the alloy [5]. The samples were 25–30 μm thick, 0.55 μm wide, and 15–20 mm in length. The x and y axes of the coordinate system in this work were chosen to be directed along the medium and long edges of the sample, respectively, and the z axis was directed along its short edge. The 180° DW lay in the yz plane at the center of the samples and divided them into two domains with oppositely directed magnetizations aligned with the y axis. The effective DW width at the surface and the coercive force of the DW were measured by the magnetooptical method and found to be 7 μm and 1 A/m, respectively.

The properties of the DW at the surface of the amorphous tape were studied using a magnetooptic micromagnetometer described in [6]. Measurements were made for the equatorial Kerr effect induced by a change in the magnetization of the illuminated area of the sample as a result of the DW movement in a magnetic field. The photomultiplier slit scanned the surface along the x axis perpendicular to the DW. The magnetization reversal was caused by the DW movement in an external y-directed magnetic field with an amplitude of 80 A/m and a frequency from 20 Hz to 15 kHz. The micromagnetometer was equipped with a vacuum cell, into which the sample was placed, and a controlled gas-admission system. The adsorbate pressure (p) in the cell could be varied from atmospheric to 10^{-3} Pa. In our experiments, the molecules were adsorbed from the gas phase onto a surface formed after a prolonged exposure of the amorphous ferromagnetic tape to air. Prior to gas admission, the sample was evacuated. Under these conditions, the sample surface contained a thin oxide film covered with

0021-3640/00/7204-0202$20.00 © 2000 MAIK "Nauka/Interperiodica"

hydroxy groups and water molecules adsorbed through the mechanism of formation of coordination bonds [7].

The studies were carried out for the frequency dependence of the DW oscillation amplitude (Δ) in an atmosphere of different gases. Water, oxygen, and nitrogen molecules of the air and the inert argon molecules were chosen as adsorbates. The $\Delta(f)$ dependence was characterized by the relaxation frequency f_r defined as $\Delta(f = f_r) = 0.7\Delta_0$, where Δ_0 equals Δ at $f \longrightarrow 0$. In Fig. 1, the DW oscillation amplitude is shown as a function of the frequency of external magnetic field for the adsorption of water molecules. Curve *1* corresponds to pressures from 1 to 400 Pa and affords the relaxation frequency $f_r = 10$ kHz. As the water vapor pressure was increased, the relaxation frequency appreciably decreased (curves *2*, *3*). The effect was fully reversible: after evacuation, the initial dependence $\Delta(f)$ was restored. A substantial change in the relaxation frequency was observed in the range of water vapor pressures 400 Pa < p < 1300 Pa (Fig. 2). The initial $\Delta(f)$ dependence did not alter upon the admission of oxygen, nitrogen, and argon into the vacuum cell up to pressures close to atmospheric.

The relaxation frequency of a DW characterizes the effective frictional force acting on a moving DW. Indeed, the DW motion in the alternating magnetic field $H = H_0\cos 2\pi ft$ can be described by the equation of a harmonic oscillator with a negligibly small effective mass:

$$b\dot{x} + kx = 2I_sH; \qquad (1)$$

where b is the damping (viscous friction) parameter, k is the effective restoring force constant due to the demagnetizing field of the sample, I_s is the saturation magnetization of the sample, $x(t) = \Delta\cos(2\pi ft - \varphi)$ is the DW displacement from its equilibrium position, and φ is the phase difference between the external field and the DW oscillations. The DW oscillation amplitude is expressed as

$$\frac{\Delta}{\Delta_0} = \left[1 + \left(\frac{f}{f_r}\right)^2\right]^{-1/2}, \qquad (2)$$

$$\Delta_0 = \Delta(f = 0) = 2I_sH_0/k, \quad f_r = k/2\pi b.$$

The experimental curves shown in Fig. 1 qualitatively agree with the theoretical ones calculated from Eq. (2) (curves *4*, *5* in Fig. 1). In particular, at low frequencies, the theoretical and experimental curves have a plateau whose length decreases with increasing water vapor pressure and, accordingly, with a decrease in the relaxation frequency. This gives evidence that the observed decrease in the relaxation frequency is associated with the increase in the damping parameter in Eq. (1).

Since the samples were not subjected to thermovacuum treatment prior to measurements, their surfaces were covered with chemisorbed oxygen atoms and hydroxy groups and coordinatively sorbed water molecules, which remained surface-bonded upon the evacuation of the sample. The reversible adsorption–desorption processes observed in this work correspond to the formation and breaking of weak hydrogen bonds between the water molecule and the hydrate covering of the real surface of the sample. At a high coverage degree, the adsorbed H_2O molecules form clusters attached to the coordinatively sorbed water molecules and containing up to three molecular layers [7].

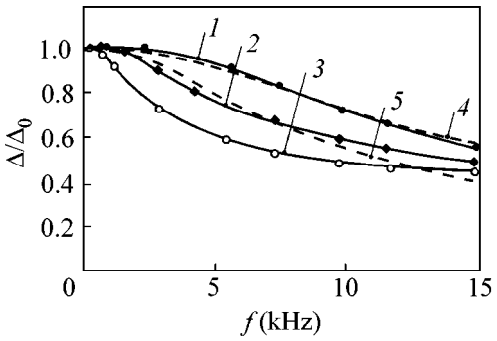

Fig. 1. Experimentally measured DW oscillation amplitudes vs. frequency of the external magnetic field in the presence of adsorption of water molecules. Water vapor pressure p = (*1*) 1–400, (*2*) 1000, and (*3*) 1900 Pa. Curves *4* and *5* are the theoretical $\Delta(f)$dependences obtained by Eq. (2) for $f_r = 10$ and 6.5 kHz, respectively.

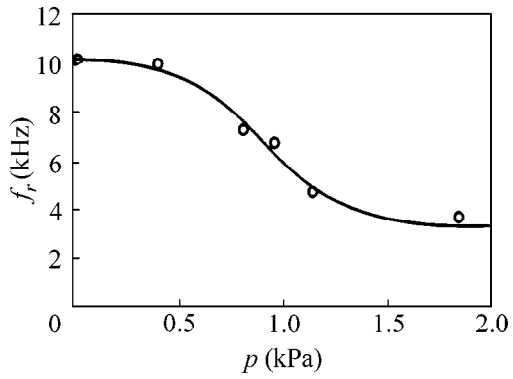

Fig. 2. Relaxation frequency of the DW oscillations as a function of water vapor pressure in the cell with the sample.

The maximum change in the relaxation frequency f_r was observed in the pressure range 0.4–1.3 kPa, where, according to the adsorption isotherms obtained for water on different oxides, the neighboring clusters of water molecules adsorbed through the formation of hydrogen bonds start to overlap [7]. At pressures $p \sim$ 1.3 kPa, the clusters completely merge to form a polymolecular surface covering of H_2O molecules. Inasmuch as the samples of amorphous ferromagnets had developed surfaces containing, in particular,

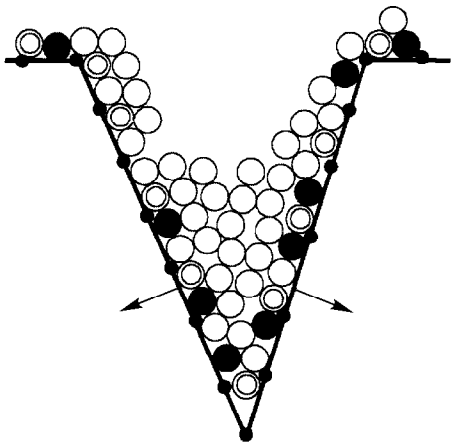

Fig. 3. Model of the formation of a magnetic microdefect at the rough surface of an amorphous magnetic tape. The microdefect is formed due to the pressure exerted by the adsorbed water molecules on the micropore walls at high concentrations of admolecules: • are the iron atoms; ● are the OH groups; ○ are the coordinatively sorbed water molecules; and ◎ are the hydrogen-bonded water molecules.

micropores, the mechanism of influence of the adsorption of water molecules on DW dynamics in the samples studied can be imagined as follows. At water vapor pressures 0.4 kPa < p < 1.3 kPa, the adsorbed water molecules fill the micropores. As a result, the adsorbed molecules produce pressure on the micropore walls. Note that the pressure in this model is applied to the micropore walls not as a result of an increase in the water vapor pressure in the cell with the sample but as a result of filling the micropores with the adsorbed water molecules. Due to the magnetoelastic interaction, the resulting microstresses produce magnetic microdefects. The suggested model of formation of surface magnetic microdefects is illustrated in Fig. 3. The enhanced surface magnetoelastic energy caused by the symmetry lowering in the surroundings of the surface atoms, compared to the atoms in the bulk of a magnet, is favorable to the formation of surface magnetic microdefects. The characteristic sizes of the micropores involved in the formation of the magnetic microdefects are determined by merging of the water clusters adsorbed on the micropore walls; i.e., these sizes are of the order of six layers of water molecules. Since the effective widths of the DWs studied in this work are several orders of magnitude larger than the characteristic sizes of the indicated microdefects, the damping of the DW motion is caused by the fluctuations of the microdefect density. The adsorption of O_2 and N_2 molecules and Ar atoms on a real surface, whose active centers all are already occupied by the chemisorbed molecules, proceeds at room temperature only through the formation of weak van der Waals bonds. In this case, only a small amount of molecules are adsorbed (less than one monolayer [7]), so that the surface is not deformed appreciably. For this reason, the above mechanism of formation of the magnetic defects in micropores is not operative in this case.

In conclusion, it should be noted that the observation of the damping effect exerted by physisorbed water molecules on the DW in the near-surface region of amorphous ferromagnets is quite unexpected, because adsorption-induced defects, at first sight, should not reveal themselves on the background of the defects of a wide range of sizes that are invariably present at the developed surfaces of amorphous ferromagnets. Since the strong influence of surface defects on DW motion is well known, it is even more unexpected that the damping parameter (effective viscous friction of DW) may increase by several times under the action of the reversible adsorption of water molecules.

We are grateful to V.S. Tsepelev for the samples of amorphous ferromagnets. This work was supported by the grant of the Ministry of Education of the Russian Federation (the St. Petersburg Competitive Center) and the Russian Foundation for Basic Research (project no. 99-02-16595).

REFERENCES

1. V. F. Kiselev and O. V. Krylov, *Adsorption and Catalysis on Transition Metals and Their Oxides* (Springer-Verlag, Berlin, 1987).
2. V. E. Zubov, A. D. Kudakov, N. L. Levshin, and V. V. Pilipenko, J. Magn. Magn. Mater. **140**–**144**, 1895 (1995).
3. B. Heinrich, K. B. Urguhart, S. T. Dutcher, *et al.*, J. Appl. Phys. **63**, 3863 (1988).
4. V. E. Zubov, G. S. Krinchik, and S. N. Kuz'menko, Zh. Éksp. Teor. Fiz. **99**, 552 (1991) [Sov. Phys. JETP **72**, 307 (1991)].
5. Yu. N. Starodubtsev, L. D. Son, V. S. Tsepelev, *et al.*, Rasplavy **4**, 76 (1992).
6. V. E. Zubov, G. S. Krinchik, and A. D. Kudakov, Prib. Tekh. Éksp., No. 3, 206 (1988).
7. V. F. Kiselev and O. V. Krylov, *Adsorption Processes on Semiconductor and Dielectric Surfaces* (Springer-Verlag, Berlin, 1985), Springer Ser. Chem. Phys., Vol. 32.

Translated by V. Sakun

JETP Letters, Vol. 72, No. 4, 2000, pp. 205–208. Translated from Pis'ma v Zhurnal Éksperimental'noĭ i Teoreticheskoĭ Fiziki, Vol. 72, No. 4, 2000, pp. 294–299.

Interface Corrugation Effect on the Polarization Anisotropy of Photoluminescence from (311)A GaAs/AlAs Short-Period Superlattices

G. A. Lyubas* and V. V. Bolotov**

** Institute of Semiconductor Physics, Siberian Division, Russian Academy of Sciences, pr. Akademika Lavrent'eva 13, Novosibirsk, 630090 Russia, e-mail: lubas@isp.nsc.ru*

*** Institute of Sensor Microelectronics, Siberian Division, Russian Academy of Sciences, Omsk, 644077 Russia*

Received July 17, 2000

Studying GaAs/AlAs superlattices containing a quantum-well-wire array revealed photoluminescence polarization anisotropy for samples with GaAs layers less than 21 Å thick. It was found that polarization for a thickness of more than 40 Å was mainly due to valence band anisotropy, whereas polarization for a thickness of less than 21 Å was equally attributable to both valence band anisotropy and anisotropy associated with interface corrugation. For a GaAs layer thickness of less than 21 Å, a blueshift of the Γ electron–Γ heavy hole transition was observed. In this transition, the position of the peak of photoluminescence from the GaAs/AlAs (311)A superlattices containing a quantum-well-wire array is shifted toward higher energies compared to the (311)B and (100) superlattices containing no quantum-well wire with the same GaAs layer thickness. The conclusion was made that a blueshift is observed in GaAs/AlAs superlattices with GaAs layers less than 21 Å thick and a redshift is observed when the thickness is larger than 43 Å. © *2000 MAIK "Nauka/Interperiodica".*

PACS numbers: 78.55.Cr

Under some conditions, a faceted (311)A GaAs surface undergoes reconstruction to a periodic array of microfacets (microgrooves) aligned with the $[\bar{2}33]$ crystallographic direction with a period of 32 Å along the $[01\bar{1}]$ direction [1–6]. Heteroepitaxy using this property is one of the promising methods for forming quantum-well wires (QWWs). The height of the microgrooves is 10.2 Å in one of the models [1–4] and 3.4 Å in another one [5, 6]. A superlattice (SL) containing an array of QWWs (QWWSL) with a diameter of less than 20 Å and, hence, with a strong effect of dimensional quantization of charge carriers, can be obtained by this strategy. This offers scope for both studying quantum phenomena at room temperature and creating QWWSL-based devices working at high temperatures. At present, many problems remain unclear in creating and studying such complicated structures. Note, for example, the statement that the (311)A surface was not split into an array of microgrooves [7]. With the aim of gaining an understanding of these problems, this work reports a study of the polarization anisotropy of photoluminescence (PL) from GaAs/AlAs (311)A QWWSL due to its structural anisotropy.

The GaAs/AlAs SLs under study were grown by molecular beam epitaxy on (311)A-, (311)B-, and (100)-oriented GaAs substrates. The A and B directions were determined by chemical etching anisotropy. Depending on the average thickness of GaAs, either corrugated GaAs and AlAs layers or a periodic array of isolated QWWs (when the average thickness of the GaAs layers was smaller than the height of microfacets) was formed in the case when the growth proceeded according to the model described in [1]. The thickness of GaAs layers in the SLs under study was varied from 4 to 23 monolayers (ML) along the (311) direction (1 ML = 0.17 nm); and the thickness of the AlAs barrier was 8, 12, and 16 ML. All the samples were examined by PL spectroscopy over a wide temperature range from 77 to 300 K. The source of PL excitation was an Ar laser (488 nm) with a typical pumping power of 10–20 mW (the power density was 5–10 W/cm^2). The PL spectra were measured using a double monochromator SDL-1 at a resolution of 0.5 nm and a photomultiplier with an S-20 cathode. Subsequently, we will mainly consider the properties of (311)A $GaAs_{10}/AlAs_8$ SLs. Note that the other samples under study demonstrated similar behavior. Typical PL spectra at 300 K from a $GaAs_{10}/AlAs_8$ SL grown on a faceted (311)A surface and containing a QWW array are shown in Fig. 1 for differing polarizations of the PL-exciting light and the light emitted by the sample. The PL-exciting light was polarized along the GaAs QWWs, and the polarization of the light emitted by the sample was analyzed in two geometries: along (solid line, *S*-component) and across (dashed line, *P*-component) the QWWs. As expected, strong polarization anisotropy was observed in the PL spectra. The degrees of polarization $(S - P)/(S + P)$ for

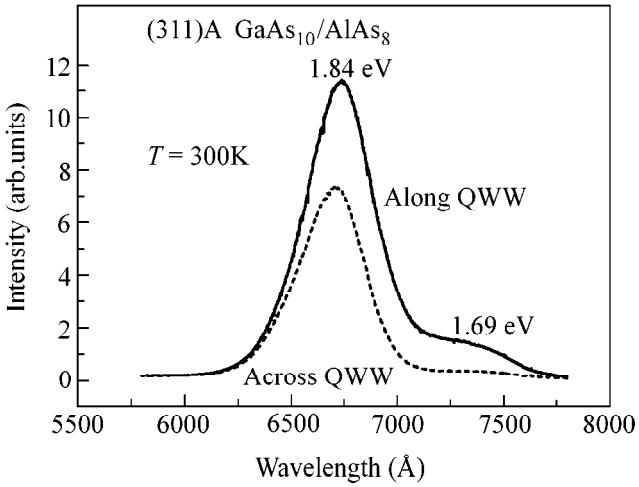

Fig. 1. Photoluminescence spectra at 300 K from a $GaAs_{10}/AlAs_8$ superlattice grown on a faceted (311)A surface and containing a quantum-well-wire array. The photoluminescence-exciting light was polarized along, and the light emitted by the sample was polarized both along (solid line, *S*-component) and across (dashed line, *P*-component) the GaAs quantum-well wires.

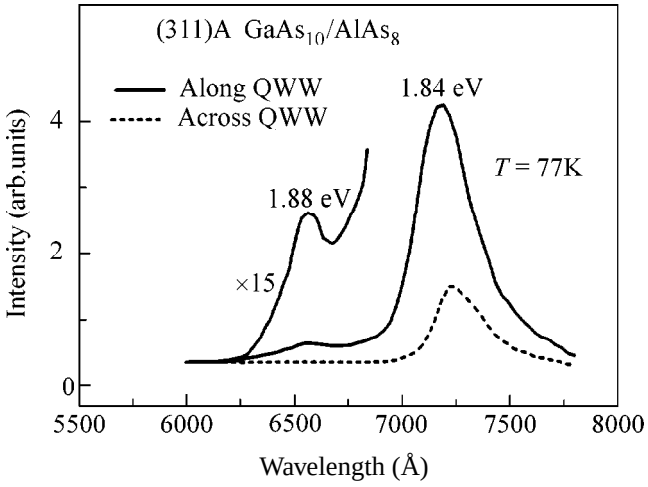

Fig. 2. Photoluminescence spectra at 77 K from a $GaAs_{10}/AlAs_8$ superlattice grown on a faceted (311)A surface and containing a quantum-well-wire array for variously polarized light emitted by the sample.

the low-energy (1.69 eV) and high-energy peaks were 0.8 and 0.22, respectively. We classified the peak at 1.84 eV as direct electron recombination (we designate it as type-I) between GaAs Γ electrons and GaAs Γ heavy holes (1*ehh* transition). The peak at 1.69 eV was determined as indirect electron recombination (type-II) between AlAs *X* electrons and GaAs Γ heavy holes. The energies of Γ–Γ and *X*–Γ optical transitions calculated by the effective mass method using the data from [8] for both the $GaAs_{10}/AlAs_8$ QWWSL and the other QWWSLs under study differing in layer thickness are in good agreement with the experimental data obtained.

The PL polarization anisotropy at 77 K is shown in Fig. 2. At this temperature, the intensity of the indirect peak (1.73 eV) is approximately 25 times higher than in the case of direct recombination (1.88 eV). The PL polarization anisotropy observed for the GaAs/AlAs QWWSLs correlates with the data of [9]. In this work, anisotropy of phonon properties was found for the same SLs, and this anisotropy was also caused by the structural anisotropy of the (311)A QWWSL. PL polarization anisotropy is exhibited over the entire range of measured temperatures from 77 to 300 K. Note that an increase in temperature leads to an increase in the intensity of direct PL and, conversely, to a decrease in the intensity of PL associated with indirect recombination (see Figs. 1, 2). This behavior agrees well with the following relationship between the direct and indirect transition intensities [10]: $I(\text{direct})/I(\text{indirect}) \sim \exp(-E_{\text{I–II}}/kT)$, where $E_{\text{I–II}} \sim$ 150 meV is the energy difference between the Γ and *X* states and *k* is the Boltzmann constant.

Consider the interface corrugation effect on the PL polarization anisotropy. The data on the optical anisotropy of 1*ehh* transitions in (311)-oriented two-dimensional GaAs/AlAs structures calculated in [11] are given in Fig. 3.[1] This figure also presents the experimental points from the same work, our experimental data, and the calculated data from [8]. It is evident in Fig. 3 that the optical anisotropy of (311)-oriented two-dimensional GaAs/AlAs structures with a GaAs layer thickness larger than 35 Å is mainly explained by the valence band anisotropy. This is evidenced by agreement of the calculated data (solid line) with the experimental points (Fig. 3, black squares) obtained in [11] and with our experimental data (Fig. 3, the light square at a thickness of 40 Å). Interface corrugation leads to relatively small additional anisotropy at a GaAs layer thickness of 35 Å. The corrugation effect at a thickness of less than 35 Å has not been observed up to now. For this purpose, we investigated structures with narrower quantum wells: the GaAs thickness was 21, 17, and 10 Å. The experimental data obtained for these structures are also presented in Fig. 3 (light squares at 21, 17, and 10 Å). It is evident that the polarization anisotropy at a thickness of less than 35 Å increases with decreasing GaAs layer thickness and is explained equally by both valence band anisotropy and interface corrugation. From the above discussion, it follows that the nature of polarization at a thickness of more than 40 Å is mainly explained by valence band anisotropy, whereas, at a thickness of less than 21 Å, it is explained equally by both valence band anisotropy and anisotropy

[1] The calculation was performed by taking into account the spin–orbit splitting of the Γ_7 band, and the inclusion of this interaction explained the growth of anisotropy for $d_{\text{GaAs}} \geq 40$ Å observed experimentally.

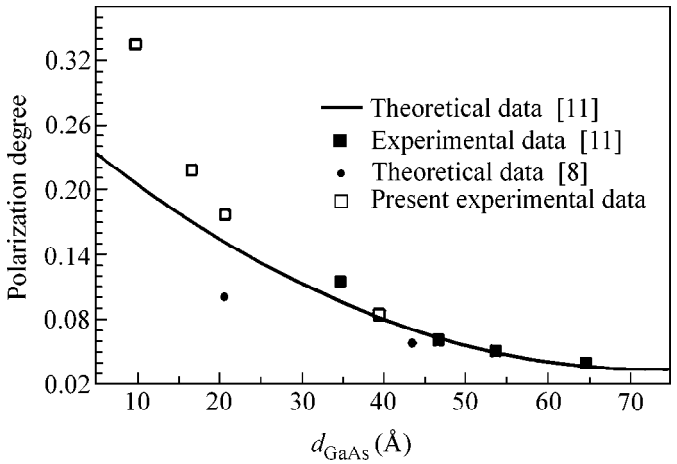

Fig. 3. Data calculated in [11] for the optical anisotropy of (311)-oriented two-dimensional GaAs/AlAs structures (solid line), experimental points from the same work (black squares), our experimental data (light squares), and data calculated in [8] (black circles).

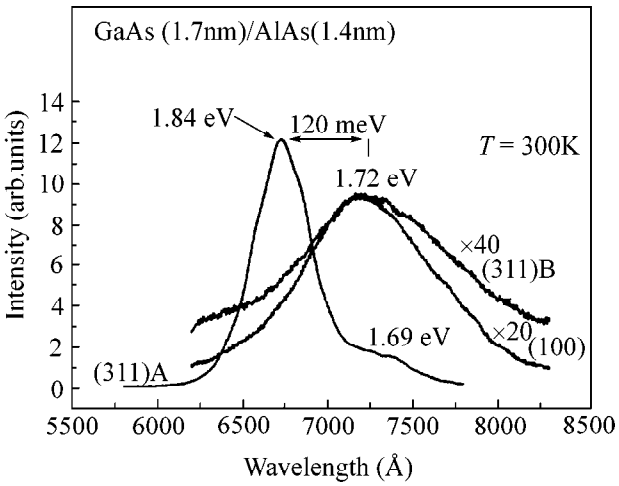

Fig. 4. Photoluminescence spectra at room temperature from $GaAs_{10}/AlAs_8$ superlattices grown on a faceted (311)A and flat (311)B and (100) surfaces with the same thickness of GaAs layers. The spectra were recorded without an analyzer.

associated with interface corrugation. The effect of the latter increases with decreasing GaAs layer thickness. Moreover, the PL intensity in (311)A structures, in which high-resolution electron microscopy revealed either corrugated GaAs layers or a periodic QWW array, was an order of magnitude higher and the PL maximum was shifted towards shorter wavelengths than in structures without corrugation.[2] Similar results were obtained for structures grown on different substrates.

The PL spectra from $GaAs_{10}/AlAs_8$ SLs grown on faceted (311)A and flat (311)B and (100) surfaces are shown in Fig. 4. Efficient PL at room temperature was observed for a GaAs/AlAs SL grown on a faceted (311)A surface and containing a QWW array. Its efficiency in the case of the (311)A SL was 25–50 times higher than in the case of (311)B and (100). In both cases, the differences were related to the formation of GaAs QWWs or corrugation. The additional dimensional quantization that resulted in this case led to a shift of the PL maximum. The lateral localization of electrons in QWWSLs (electrons in a QWWSL can move only along the QWWs) reduces the nonradiative interface recombination [3], and the high PL intensity at 300 K is the result of this effect. Moreover, we found a so-called blueshift of the Γ electron–Γ heavy hole transition, when the PL peak position for the GaAs/AlAs (311)A QWWSL was shifted towards higher energies compared to the (311)B and (100) SLs with the same thickness of GaAs layers. With regard to the data reported in [1, 2], where a redshift was observed for (311)A SLs with a GaAs layer thickness of more than 43 Å (the PL peak position for (311)A QWWSLs was shifted towards lower energies), the conclusion can be made that GaAs/AlAs SLs should respectively exhibit a blueshift or a redshift when the GaAs layer thickness is smaller than 21 Å or larger than 43 Å. Note that the blueshift was observed for the first time, and its magnitude increases from 60 meV for 21 Å thick samples to 170 meV for samples with a GaAs layer thickness of 10 Å. This fact reflects the enhancement of the corrugation effect with decreasing GaAs layer thickness and correlates with the calculation made by Kiselev and Rössler [12], where it was shown that the lowest electron state in corrugated GaAs structures is higher than in flat GaAs/AlAs SLs with the same effective thickness of GaAs layers.

Thus, we investigated the properties of PL from GaAs/AlAs QWWSLs. The phenomenon of PL polarization anisotropy was observed for samples with a less than 21 Å GaAs layer thickness. The QWWSLs with an average GaAs layer thickness of less than 10 Å exhibited considerably lower anisotropy. The polarization anisotropy was entirely absent in the (100)-oriented SLs. As distinct from [2], where the properties of PL from corrugated GaAs/AlAs SLs with a GaAs layer thickness varying over the range from 43 to 66 Å and where efficient PL was observed for the emitted light polarized across the quantum wires, the efficient PL in this work was observed in the PL spectra from GaAs/AlAs QWWSLs with a GaAs layer thickness of less than 21 Å for the emitted light polarized along the quantum wires. It was found that the nature of polarization anisotropy differs for differing thicknesses of the GaAs layer. In the case of a (311)A SL of 40–66 Å thickness, the nature of polarization is explained mainly by valence band anisotropy, whereas it is

[2] The quality of the samples to be studied was monitored by x-ray diffraction analysis and was comparable.

explained equally by both valence band anisotropy and anisotropy associated with interface corrugation in the case of a QWWSL less than 21 Å thick. The phenomenon of PL polarization anisotropy is exhibited over a wide range of temperatures from 77 to 300 K. For a GaAs layer thickness of less than 21 Å, a blueshift of the Γ electron–Γ heavy hole transition (1*ehh* transition) was observed. That is, the position of the peak of photoluminescence from the GaAs/AlAs (311)A QWWSL was shifted towards higher energies compared to the (311)B and (100) SLs with the same thickness of GaAs layers. Based on systematization of the experimental data, we made the conclusion that a blueshift should be observed in GaAs/AlAs superlattices with a GaAs layer thickness of less than 21 Å and a redshift should be observed for a thickness of more than 43 Å. The differences found in PL from SLs grown on (100), (311)B, and faceted (311)A surfaces confirm the formation of GaAs quantum wires in the case of GaAs/AlAs heteroepitaxy on a faceted surface. This fact, even taken alone, rules out the statement made in [7] that the (311)A surface is not split into an array of microgrooves.

The studies outlined above are important for manufacturing QWWSL-based optoelectronic devices (lasers, light-emitting diodes, etc.) working over a wide temperature range.

The authors are grateful to V.A. Volodin, M.D. Efremov, V.V. Preobrazhenskiĭ, and B.R. Semyagin (Institute of Semiconductor Physics, Siberian Division, Russian Academy of Sciences) for help in PL measurements and for manufacturing the structures.

REFERENCES

1. R. Nötzel, N. N. Ledentsov, L. A. Daweritz, *et al.*, Phys. Rev. Lett. **67**, 3812 (1991).
2. R. Nötzel, N. N. Ledentsov, L. A. Daweritz, *et al.*, Phys. Rev. B **45**, 3507 (1992).
3. R. Nötzel, N. N. Ledentsov, and K. Ploog, Phys. Rev. B **47**, 1299 (1993).
4. V. Ya. Prints, I. A. Panaev, V. V. Preobrazhenskiĭ, and B. R. Semyagin, Pis'ma Zh. Éksp. Teor. Fiz. **60**, 209 (1994) [JETP Lett. **60**, 217 (1994)].
5. M. Wassermeier, J. Sudijono, M. D. Johnson, *et al.*, J. Cryst. Growth **150**, 425 (1995).
6. M. Wassermeier, J. Sudijono, M. D. Johnson, *et al.*, Phys. Rev. B **51**, 14721 (1995).
7. O. Brandt, K. Kamamoto, Y. Tokuda, and N. Tsukada, Phys. Rev. B **48**, 17599 (1993).
8. C. Joanin, A. Hallaoui, and D. Bertho, Phys. Rev. B **50**, 1645 (1994).
9. M. D. Efremov, V. A. Volodin, V. V. Bolotov, *et al.*, Solid State Phenom. **69–70**, 507 (1999).
10. M. Nakayama, I. Tanaka, I. Kimura, and H. Nishimura, Jpn. J. Appl. Phys. **29**, 41 (1990).
11. M. V. Belousov, V. L. Berkovits, A. O. Gusev, *et al.*, Fiz. Tverd. Tela (St. Petersburg) **36**, 1098 (1994) [Phys. Solid State **36**, 596 (1994)].
12. A. A. Kiselev and U. Rössler, Phys. Rev. B **50**, 14283 (1994).

Translated by A. Bagatur'yants

JETP Letters, Vol. 72, No. 4, 2000, pp. 209–212. Translated from Pis'ma v Zhurnal Éksperimental'noĭ i Teoreticheskoĭ Fiziki, Vol. 72, No. 4, 2000, pp. 300–305.

Magnetotransport Properties of a Ballistic Ring Interferometer on the Basis of a GaAs Quantum Well with a High Concentration of 2D Electron Gas

A. A. Bykov, A. K. Bakarov, L. V. Litvin, and A. I. Toropov

Institute of Semiconductor Physics, Siberian Division, Russian Academy of Sciences, pr. Akademika Lavrent'eva 13, Novosibirsk, 630090 Russia

e-mail: bykov@thermo.isp.nsc.ru

Received July 18, 2000

Magnetotransport properties of ballistic ring interferometers made on the basis of 2D electron gas in a GaAs quantum well with AlAs/GaAs superlattice barriers are studied. An asymmetry of magnetoresistance and a phase reversal in h/e oscillations are observed when the bias voltage across the ring exceeds kT/e. *© 2000 MAIK "Nauka/Interperiodica".*

PACS numbers: 73.50.Jt; 75.70.Cn; 07.60.Ly

By now, ring interferometers have become conventional model objects for studying the processes of coherent charge carrier transfer in solid-state structures [1, 2]. One of the important physical characteristics that determine the transport regime in such interferometers is the ratio $l_p/\pi r_{\text{eff}}$, where l_p is the momentum-related mean free path of charge carriers and r_{eff} is the effective ring radius corresponding to the period of h/e oscillations. In the first interferometers fabricated on the basis of metal films, this ratio was much less than unity, $l_p/\pi r_{\text{eff}} \ll 1$, which corresponded to a diffusive regime of charge carrier transfer in a ring [3–5]. The small value of l_p in metal films does not allow one to go beyond the diffusive regime in ring interferometers fabricated on their basis. This barrier was overcome with the progress in molecular beam epitaxy, which made it possible to grow GaAs/AlGaAs semiconductor heterojunctions with high-mobility 2D electron gas (2DE gas). On the basis of 2DE gas in GaAs/AlGaAs heterojunctions, ballistic rings with a transport regime satisfying the condition $l_p/\pi r_{\text{eff}} > 1$ were fabricated and studied [6–9].

At present, coherent transport in ballistic interferometers are being studied for $T < 0.3$ K and for bias voltages across the ring no greater than kT/e. This is related to the fact that the maximum temperature at which interference processes occur in the ring is determined by the value of r_{eff}. To increase this temperature and to carry out experimental studies of the coherent properties of ballistic interferometers at bias voltages exceeding kT/e, it is necessary to reduce the dimensions of the ring. However, the fabrication of ballistic interferometers of small dimensions on the basis of conventional GaAs/AlGaAs heterojunctions encounters some difficulties related to the contradictory requirements that are imposed on the equilibrium parameters of 2DE gas in the original structure. On the one hand, to reduce r_{eff}, it is necessary that the 2DE gas have the maximum concentration, because the main factor that limits r_{eff} in semiconductor rings is not the resolution of the electron beam lithography, as in the case of metallic rings, but the presence of depletion regions comparable with the lithographic width of the ring. In this situation, the minimum possible r_{eff} is equal to the depletion region width, which is less, the higher the concentration of 2DE gas. On the other hand, in GaAs/AlGaAs and InGaAs/AlGaAs heterojunctions with high 2DE gas concentrations, the scattering potential of the dopant causes a decrease in l_p and does not allow one to use these structures for the fabrication of ballistic rings [10, 11].

We believe that the optimal structure for the fabrication of small-size ballistic rings is the modulated semiconductor structure proposed in recent publications [12, 13]. In such a structure, the 2DE gas is confined in a GaAs quantum well whose barriers are formed by short-period AlAs/GaAs superlattices. The *X*-electrons that occur in the superlattice barriers smooth out the fluctuation potential of the dopant, which allows one, without loss of mobility, to considerably increase the concentration of 2DE gas in the GaAs quantum well, compared to the conventional GaAs/AlGaAs heterojunctions. In this paper, we report on the studies of the transport properties of submicron rings fabricated for the first time on the basis of such a modulated structure.

The original semiconductor structure was grown by molecular beam epitaxy on a (001) GaAs semi-insulating substrate. The quantum well was formed by a GaAs layer 10 nm thick. The barriers of the well were formed by $(AlAs)_4(GaAs)_8$ short-period superlattices lying on two sides of the GaAs layer. The sources of charge car-

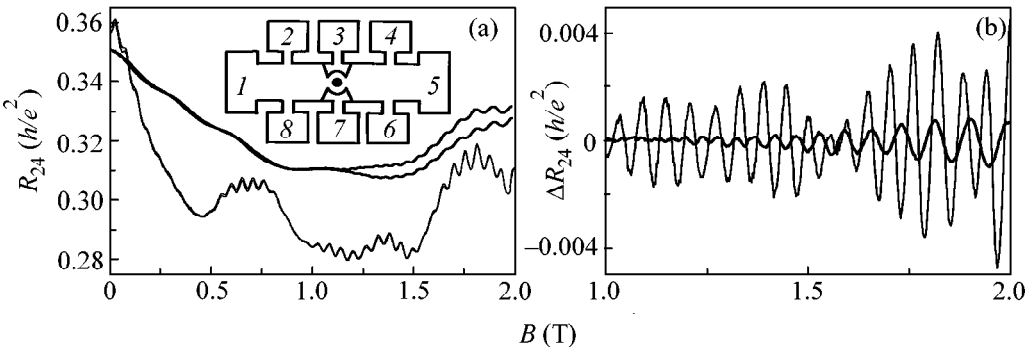

Fig. 1. (a) Typical experimental dependences $R_{24}(+B)$ and $R_{24}(-B)$ at $T = 4.2$ K. The inset shows the schematic diagram of a ballistic ring interferometer with a split gate. (b) Dependences of R_{24} on magnetic field with the subtracted monotonic component; $I_{15} = 10^{-9}$ (thin line) and 10^{-6} A (thick line).

riers for the quantum well were two Si δ-layers with a concentration of 2.5×10^{12} cm^{-2}. These layers were positioned in the GaAs layers of the short-period superlattices at distances of 12.8 and 8.8 nm from the walls of the quantum well. The greater distance corresponded to the lower Si δ-layer, which was made in view of silicon segregation. At $T = 4.2$ K, the equilibrium parameters of a 2DE gas confined in the quantum well were as follows: the concentration $n_s = 1.8 \times 10^{12}$ cm^{-2}, the mobility $\mu = 3.5 \times 10^5$ cm^2/V s, and the corresponding mean free path for the momentum $l_p = 5.5$ μm.

The schematic diagram of a ring interferometer is shown in the inset in Fig. 1a. The samples used in the experiment were Hall bars 50 μm wide. The samples had a single pair of current leads (*1* and *5*) and three pairs of Hall leads (*2* and *8*, *3* and *7*, and *4* and *6*) spaced at 100-μm intervals. The ring was positioned between the central Hall leads (*3* and *7*), which were used as contacts for the split gate. The Hall bars were fabricated by optical lithography with wet chemical etching, and the rings were formed by electron beam lithography and dry etching.

The experiments were carried out at a temperature of 4.2 K in magnetic fields up to 2 T. The magnetoresistance of the interferometers was determined by the formula $R_{24} = V_{24}/I_{15}$, where V_{24} is the voltage between contacts *2* and *4*, and I_{15} is the current between contacts *1* and *5*. The currents used in the experiment varied from 10^{-9} to 10^{-6} A. The voltage V_{24} was measured by a phase-sensitive amplifier at the frequency of the alternating bias current I_{15}, which was equal to 777 Hz. The microwave emf was measured across the bias ohmic contacts *1* and *5* and recorded at the frequency of the amplitude modulation of the microwave radiation, which was supplied to the sample under study through a coaxial cable. Below, we present the results of the experimental study of the transport properties of an interferometer with $r_{\text{eff}} = 0.15$ μm. Qualitatively similar behavior was observed for a ring with $r_{\text{eff}} = 0.20$ μm.

Figure 1a shows the dependences $R_{24}(+B)$ and $R_{24}(-B)$ for the conditions corresponding to $V_{24} \ll kT/e$ (thin line) and $V_{24} \gg kT/e$ (thick line). In the first case, the magnetoresistance curves obtained for different signs of the magnetic field coincide within the experimental error. In these conditions at $T = 4.2$ K, the magnetoresistance exhibits pronounced *h*/*e* oscillations (Fig. 1b) corresponding to single-quantum steps in the magnetic flux through a circle with the effective radius $r_{\text{eff}} = 0.15$ μm (as far as we know, this is the least value of r_{eff} yet achieved for ballistic rings). In the second case, i.e., when $V_{24} \gg kT/e$, the *h*/*e* oscillations disappear, and, in higher magnetic fields ($B > 1$ T), only Shubnikov–de Haas (SdH) oscillations are observed (see Fig. 1b). The SdH oscillations are also present in the dependences $R_{24}(B)$ for small bias currents, but, at $T = 4.2$ K in magnetic fields $B < 2$ T, they are difficult to observe against the dominant *h*/*e* oscillations. Fourier analysis of the dependences $R_{24}(1/B)$ showed that, in contrast to *h*/*e* oscillations, the amplitude of SdH oscillations is retained in the entire range of bias currents I_{15} used in the experiment. The period of these oscillations was found to correspond to the concentration calculated from the dependence $V_{28}(B)$, and their amplitude coincided with that of SdH oscillations for the original Hall bar without a ring.

The experimental results allow us to conclude that the "coexistence" of two types of oscillations in a ballistic interferometer in the conditions $V_{24} \ll kT/e$ is caused by the series connection of the ring resistance and that of 2DE gas regions located between the ring and the ohmic contacts *2* and *4*. In this case, the disappearance of the *h*/*e* oscillations observed for high voltages ($V_{24} \gg kT/e$) is related to heating of the electron gas in the ring. The independence of the amplitude of SdH oscillations of the voltage V_{24} in the entire range of currents under study testifies to fairly weak heating in the 2DE gas regions. Such behavior is consistent with the fact that, for the interval of the currents I_{15} used in the experiment, the voltage drop across the 2DE gas

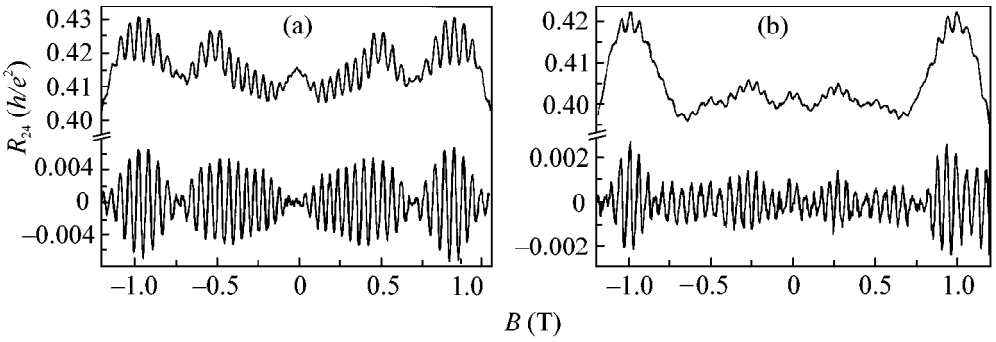

Fig. 2. Experimental dependences $R_{24}(B)$ and the dependences with the subtracted monotonic component at T = 4.2 K for $R_{24}(0) \sim h/2e^2$: I_{15} = (a) 10^{-9} and (b) 10^{-7} A.

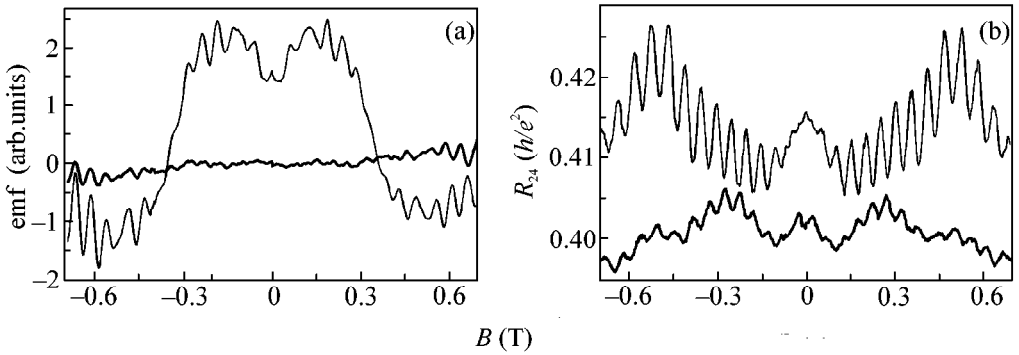

Fig. 3. (a) Dependences of the microwave emf on magnetic field at T = 4.2 K for a microwave radiation frequency of 2 GHz: the experimental curve (thin line) and the antisymmetric component (thick line). (b) Experimental dependences $R_{24}(B)$ at T = 4.2 K; $I_{15} = 10^{-9}$ (thin line) and 10^{-7} A (thick line).

regions located between the ring and the contacts *2* and *4* was always much less than kT/e, because the resistance of these regions was two orders of magnitude less than the resistance of the ring; hence, the major part of the voltage drop V_{24} occurred across the latter resistance.

An unexpected result was the difference between the dependences $R_{24}(+B)$ and $R_{24}(-B)$ observed in the case $V_{24} \gg kT/e$ in high magnetic fields (the thick line in Fig. 1a), because, according to the Onsager relations, such an asymmetry should not occur in a mesoscopic system without magnetic impurities [4]. With an increase in the bias current, the Aharonov–Bohm oscillations also become asymmetric about zero magnetic field. This can be seen from Fig. 2, which shows the dependences $R_{24}(B)$ for two different values of the current I_{15} and for an interferometer state close to single-mode. When $V_{24} \ll kT/e$, the dependences exhibit beats of h/e oscillations, which are typical of single-mode rings [9, 14], and a symmetry about zero magnetic field. At $I_{15} = 10^{-9}$ A, this symmetry was retained for all other states of the interferometer. However, in the case $V_{24} > kT/e$, the beats disappear and the h/e oscillations become asymmetric about zero magnetic field.

Let us discuss the experimental results. The fundamental difference between the transport properties of rings in the diffusive and ballistic regimes of charge carrier transfer consists in the fact that, in the first case, the transport properties are determined by the type of random scattering potential [15] and, in the second case, by the profile of the confining potential that forms the geometry of the conducting regions of the ring [14, 16]. One of the consequences of the inequality $l_p/\pi r_{\text{eff}} > 1$ is that, in a ballistic interferometer, the transport processes will depend not only on the ring geometry, but also on the geometry of the 2DE gas regions located at a distance of the order of $(l_p - \pi r_{\text{eff}})/2$ from the ring input and output. For the ring under study, this distance is 2.5 μm, which is much greater than πr_{eff} = 0.5 μm. This fact does not allow one to neglect the influence of the 2DE gas regions contacting the ring on charge carrier transfer in a ballistic interferometer. The central symmetry of both the ring and these regions can be violated because of the imperfection of the technol-

ogy used for the fabrication of ballistic microstructures [1]; in nonequilibrium conditions, such a symmetry violation should give rise to nonlinear effects [17–20].

This point of view is supported by the measurements of the microwave emf in the ring. The results of these measurements are presented in Fig. 3a. The studies were performed at $T = 4.2$ K, at a microwave radiation frequency of 2 GHz. In these conditions, when the energy of a microwave radiation quantum is much less than kT, the measured emf is a result of the effect of rectification caused by violation of the central symmetry in the mesoscopic system [18, 19]. From Fig. 3a, one can see that, in a ballistic interferometer, the effect of rectification contains both symmetric and antisymmetric components with respect to zero magnetic field. These components are observed in strong magnetic fields, and they are absent in mesoscopic systems with diffusive charge carrier transfer [19]. The presence of these components allows one to conclude that the asymmetry of the magnetoresistance of a ballistic interferometer, $R_{24} = V_{24}/I_{15}$, in the conditions $V_{24} > kT/e$ is caused by the contribution of a nonlinear correction that depends on the sign of the magnetic field to the measured voltage V_{24}. A nonlinear correction that is symmetric about zero magnetic field also manifests itself in the dependences $R_{24}(B)$. As seen from Fig. 3b, this correction gives rise to a reversal of the phase of h/e oscillations with increasing bias current I_{15}.

Thus, we studied the magnetotransport properties of ballistic ring interferometers made on the basis of a 2DE gas in a GaAs quantum well; the studies were performed in a wide range of bias currents at $T = 4.2$ K. The experiments showed that, when the voltage across the ring exceeds the quantity kT/e, an asymmetry of the magnetoresistance is observed and a phase reversal occurs in the Aharonov–Bohm oscillations. The effect of rectification was also observed in a ballistic ring interferometer; this effect depends on the sign of the magnetic field and is caused by the asymmetry of the scattering of nonequilibrium charge carriers by the confining potential of the microstructure. It was shown that, owing to the high concentration and mobility of the 2DE gas confined in GaAs quantum wells with AlAs/GaAs short-period superlattice barriers, such a modulated semiconductor structure is promising for the fabrication of ballistic microstructures with submicron dimensions.

This work was supported by the Russian Foundation for Basic Research (project no. 98-02-17921) and the international program in science and technology "Physics and Technology of Nanostructures" (project no. 99-1132).

REFERENCES

1. S. Pedersen, A. E. Hansen, A. Kristensen, *et al.*, Phys. Rev. B **61**, 5457 (2000).
2. A. Van Oudenaarden, Yu. V. Nazarov, and J. E. Mooij, Phys. Rev. B **57**, 8816 (1998).
3. R. A. Webb, S. Washburn, S. P. Umbach, *et al.*, Phys. Rev. Lett. **54**, 2696 (1985).
4. A. D. Benoid, S. Washburn, C. P. Umbach, *et al.*, Phys. Rev. Lett. **57**, 1765 (1986).
5. S. Washburn, H. Schmid, D. Kern, *et al.*, Phys. Rev. Lett. **59**, 1791 (1987).
6. G. Timp, A. M. Chang, J. E. Cunningham, *et al.*, Phys. Rev. Lett. **58**, 2814 (1987).
7. J. A. Simmons, D. C. Tsui, and G. Weimann, Surf. Sci. **196**, 81 (1988).
8. G. Timp, M. Mankiewich, P. de Vegvar, *et al.*, Phys. Rev. B **39**, 6227 (1989).
9. K. Ismail, S. Washburn, and K. Y. Lee, Appl. Phys. Lett. **59**, 1998 (1991).
10. A. A. Bykov, L. V. Litvin, and S. P. Moshchenko, Surf. Sci. **361**/**362**, 747 (1996).
11. A. A. Bykov, Z. D. Kvon, E. B. Olshanetsky, *et al.*, Physica E (Amsterdam) **2**, 519 (1998).
12. K.-J. Friedland, R. Hey, H. Kostial, *et al.*, Phys. Rev. Lett. **77**, 4616 (1996).
13. K.-J. Friedland, R. Hey, H. Kostial, *et al.*, Jpn. J. Appl. Phys. **37**, 1340 (1998).
14. W.-C. Tan and J. I. Inkson, Phys. Rev. B **53**, 6947 (1996).
15. A. D. Stone, Phys. Rev. Lett. **54**, 2692 (1985).
16. O. A. Tkachenko, V. A. Tkachenko, D. G. Baksheev, *et al.*, Pis'ma Zh. Éksp. Teor. Fiz. **71**, 366 (2000) [JETP Lett. **71**, 255 (2000)].
17. V. I. Belinicher and B. I. Sturman, Usp. Fiz. Nauk **130**, 415 (1980) [Sov. Phys. Usp. **23**, 199 (1980)].
18. A. I. Larkin and D. E. Khmel'nitskiĭ, Zh. Éksp. Teor. Fiz. **91**, 1815 (1985) [Sov. Phys. JETP **64**, 1075 (1986)].
19. V. I. Fal'ko and D. E. Khmel'nitskiĭ, Zh. Éksp. Teor. Fiz. **95**, 328 (1989) [Sov. Phys. JETP **68**, 186 (1989)].
20. F. Hekking and Yu. V. Nazarov, Phys. Rev. B **44**, 11506 (1991).

Translated by E. Golyamina

JETP Letters, Vol. 72, No. 4, 2000, pp. 213–216. Translated from Pis'ma v Zhurnal Éksperimental'noĭ i Teoreticheskoĭ Fiziki, Vol. 72, No. 4, 2000, pp. 306–311.

Observation of Spin-Wave Envelope Dark Solitons in Ferromagnetic Films

H. Benner*, B. A. Kalinikos, N. G. Kovshikov**, and M. P. Kostylev****

** Darmstadt University of Technology, D-64289 Darmstadt, Germany*

*** St. Petersburg State Electrotechnical University, St. Petersburg, 197376 Russia*

*** e-mail: borisk@borisk.usr.etu.spb.ru*

Received July 20, 2000

Microwave spin-wave envelope dark solitons were experimentally observed for the first time. Dark solitons with zero minimum amplitude were generated by two-frequency excitation of input spin waves with a fixed amplitude. Nonlinear interaction between these two traveling waves gave rise to periodic sequences of dark solitons in a ferromagnetic film. © *2000 MAIK "Nauka/Interperiodica".*

PACS numbers: 75.30.Ds; 75.70.-i

It is known that two types of envelope solitons—bright and dark—can propagate in nonlinear dispersive waveguide media (see, e.g., [1]). The great majority of experimental works have been devoted to studying bright solitons. Optical solitons in optical fibers [2] and spin-wave solitons in ferromagnetic films (see, e.g., [3–6] and references therein) have been most thoroughly studied. At the same time, the generation and propagation of dark solitons, both optical (detailed information can be found in recent review [7]) and spin-wave (only one publication [8] is known to us), have not been adequately studied.

In the first experimental work [4] devoted to studying spin- wave dark solitons, the envelopes of the spin-wave signals were found to exhibit two characteristic minima at the "bottom" of dark pulses. In a recent theoretical work [9], this phenomenon was explained by the excitation of soliton pairs. In the second experimental work [6], the spin-wave pulses were self-generated in the form of pairs of dark solitons.

The purpose of this work was to experimentally investigate the possibility of exciting sequences of single dark solitons. To generate envelope dark solitons, one usually feeds dark rectangular pulses into the input of a nonlinear dispersive waveguide medium. In this work, wave profiles shaped like single envelope solitons with zero minimum amplitude (the so-called black solitons) were formed by a different method, namely, by using two-frequency input excitation. Two continuous microwave signals with equal amplitudes and different (close) frequencies f_1 and f_2 were fed into the input of a ferromagnetic film.

The basic idea of the method was that, even in the linear regime, two such continuous input signals would give rise to periodic spin-wave beats with period $T = 1/\Delta f$ ($\Delta f = |f_1 - f_2|$) in the ferromagnetic film. In this case, the phase of a signal at the central "carrier" frequency $(f_1 + f_2)/2$ would undergo 180° jumps at the beat zero-amplitude points. Such phase jumps of the carrier signal are known to be one of the main characteristics of a topological (black) envelope soliton [1, 2]. We conjectured that the nonlinear evolution of spin-wave beats might give rise to a periodic sequence of single black solitons. This assumption was justified in our experiments.

Previous experiments with spin-wave bright and dark solitons were successfully explained on the basis of the nonlinear Schrödinger equation (NSE). That is why this approach was used as a heuristic model in conducting the experiment described below. According to the NSE model

$$i(\partial u/\partial t + V_g \partial u/\partial z) + \frac{D}{2}\frac{\partial^2 u}{\partial z^2} - N|u|^2 u = 0, \qquad (1)$$

envelope dark solitons can arise in waveguide media if the dispersion and nonlinear coefficients for the carrier frequency have identical signs. This requirement is satisfied by a quasi-surface spin wave propagating in tangentially magnetized ferromagnetic films. In a single-crystal yttrium-iron garnet (YIG) film with free surface spins, such a wave is characterized by a monotonic dispersion $\omega(k)$ in the long-wavelength region of the spectrum [10]. The corresponding dispersion $D = \partial^2\omega/\partial k^2$ and nonlinear $N = \partial\omega/\partial|u|^2$ coefficients are negative.

Samples used in the experiments were narrow 2-mm thick YIG strips (spin-wave "waveguides"). The waveguides were cut from single-crystal YIG films of thickness L equal to 5.2, 6.9, 7.2, and 13.9 μm grown on (111)-orientated gadolinium-gallium garnet substrates. Spin waves were excited and picked up using a standard setup [3, 4] containing shorted input and out-

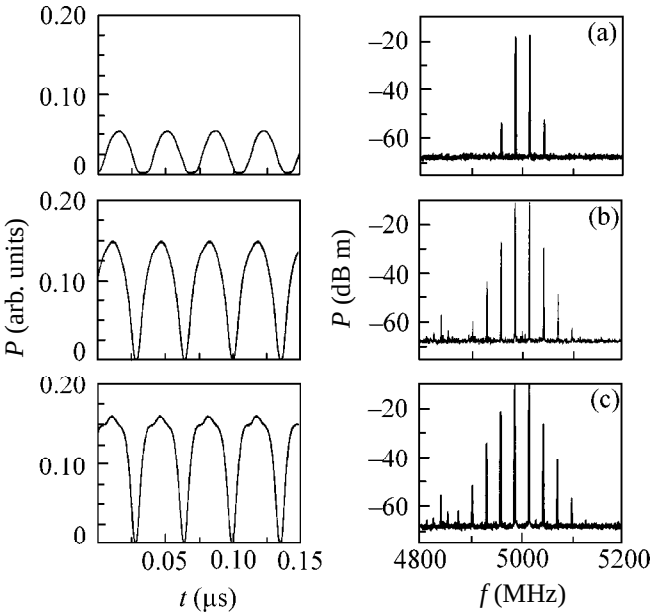

Fig. 1. Microwave signal envelope at the output of the setup (left) and the corresponding frequency spectra (right) for the input signals of different powers P_1 and P_2: (a) $P_1 = -3$ dB m and $P_2 = -1$ dB m; (b) $P_1 = 7$ dB m and $P_2 = 9$ dB m; and (c) $P_1 = 11$ dB m and $P_2 = 13$ dB m. The thickness of the yttrium-iron garnet film is 6.9 μm; the static magnetic field is 1034 Oe; and the frequencies of input signals are $f_1 =$ 4990 MHz and $f_2 = 5018$ MHz.

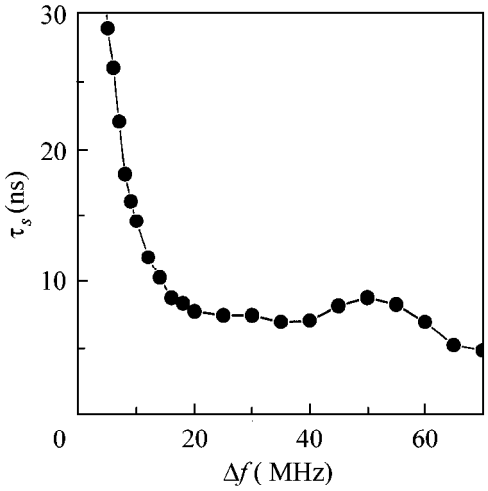

Fig. 2. Dark soliton duration as a function of detuning $\Delta f = f_1 - f_2$ between the input frequencies. The thickness of the yttrium-iron garnet film is 13.9 μm, and the powers of input signals are $P_1 = P_2 = 20$ dB m. The frequency of one of the input signals was maintained constant at $f_1 = 4990$ MHz.

put microstrip antennas of width 50 μm and length equal to the film waveguide width. The separation between the antennas, photolitographically formed on movable ceramic substrates, could be varied.

The experiments may be conventionally separated into two steps. At the first step, the amplitude-frequency characteristics and the dispersive properties of the samples were examined. The traveling spin waves were excited in the linear regime. At the second step, the nonlinear effects arising upon the excitation of two intense spin waves in the film were studied. The carrier frequencies of these input waves were chosen in such a way that they, and all the nonlinearly generated spin-wave harmonics, lie in the range of the spin-wave spectrum determined for a particular experimental sample at the first step.

The measurements carried out for all YIG film samples at different input frequencies f_1 and f_2 and the same power $P_1 = P_2$ showed that, as the input power increased, the spin-wave propagation regime changed from linear to nonlinear. In the nonlinear propagation regime, the formation of a steady periodic sequence of spin-wave pulses with profiles $u(t)$ corresponding to the envelope dark solitons was observed.

The typical experimental results are illustrated in Fig. 1. In these experiments, the microwave signal envelopes and the respective frequency spectra were simultaneously measured at the film output. The data shown in Fig. 1 were obtained for a sample of thickness $L = 6.9$ μm in a static magnetic field of 1034 Oe. The lower edge of the spectrum of quasi-surface spin waves measured for this field was 4860 MHz. The input frequencies were chosen to be $f_1 = 4990$ MHz and $f_2 =$ 5018 MHz. The wave number calculated for the mean frequency $(f_1 + f_2)/2$ was 191 rad/cm. As the power of the input signals increased, the minima in the spin-wave signal envelope sharpened and its frequency spectrum was enriched. The development of a nonlinear interference of input waves resulted in the formation of a periodic sequence of pulses shaped like black solitons (Fig. 1c).

The aforementioned gradual enrichment of the frequency spectrum of the soliton sequence proceeded by a four-wave mechanism. The spacing between the neighboring nonlinearly generated harmonics was equal to the Δf value. At the same time, the experiments showed that, after the microwave power exceeded a certain level depending on the film thickness, the periodic sequence of solitons was destroyed. This destruction was of both nonlinear and thermal character. The nonlinear and thermal mechanisms of destruction of the soliton sequence require special study.

It was found that, for all film thicknesses used and at a fixed input power chosen slightly below the "destruction threshold" of a periodic soliton sequence, the shape and duration τ_s of a single soliton remain virtually unchanged upon changing the detuning between the input frequencies f_1 and f_2 in a certain range (of one of them or both simultaneously). The soliton duration as a function of detuning Δf is shown in Fig. 2 for a film of thickness $L = 13.9$ μm. The frequency f_1 was maintained constant and equal to 4990 MHz. It should be

emphasized that similar curves demonstrating insensitivity of the soliton shape and duration to Δf were obtained for all films studied. For instance, it is seen in Fig. 2 that the soliton duration remains virtually constant upon changing Δf from 20 to 40 MHz at L = 13.9 μm. To illustrate this phenomenon more pictorially, Fig. 3 demonstrates the envelopes of the generated periodic soliton sequences and frequency spectra measured close to the τ_s constancy range boundaries, i.e., at Δf_{min} = 24 MHz (Fig. 3a) and Δf_{max} = 40 MHz (Fig. 3b). It is noteworthy that, when varying Δf from f_{min} to f_{max}, the soliton shape and duration are virtually independent of the number of nonlinearly generated harmonics arising in the frequency band of a single soliton. As the detuning between the input frequencies falls outside of the indicated Δf_{min} or Δf_{max} value, the soliton shape and duration begin to depend on Δf.

To verify that the pulse shapes in the observed sequence are governed by the four-wave mechanism of spin-wave self-action [11] and, hence, that we are indeed dealing with a soliton sequence, numerical simulation was carried out. The simulation was based on the theoretical relationships obtained in [12]. These relationships describe the motion of the spatial Fourier components of the envelope of varying magnetization. They were deduced based on the Landau–Lifshitz equation of motion of the magnetic moment and the equations of magnetostatics. The resulting system of nonlinear inhomogeneous first-order differential equations accounts for the excitation of the magnetization waves in ferromagnetic films by a microstrip antenna, the evolution of the wave envelope, and the formation of a sequence of nonlinear pulses. Depending on the chosen parameters, this system allows the propagation of the dark and bright solitons to be numerically analyzed.

As distinct from the NSE model (1), this approach allows for the specific features of the real spin-wave spectrum in ferromagnetic films, as well as of the excitation and reception of the magnetization waves by microstrip antennas. The latter is particularly important. This approach allows one to avoid the calculation of the spin-wave amplitudes (which is necessary in the NSE approach) and makes it possible to deal directly with the experimentally measured quantities, namely, the input and output microwave powers.

The envelope profile calculated for the microwave signal at the output of the experimental setup is shown in Fig. 4. The experimentally measured profile is shown in the same figure by the dashed line. The calculation was carried out for the following experimental conditions: film thickness L = 13.9 μm; saturation magnetization 1750 G; magnetic loss parameter ΔH = 0.5 Oe; static magnetic field 1090 Oe (the corresponding lower bound for the excitation of quasi-surface spin waves is 4930 MHz); input frequencies f_1 = 4995 MHz and f_2 = 5036 MHz; length and width of the input and output microstrip transducers 2 mm and 50 μm, respectively; and the distance between them, 6.5 mm. The microwave power at the input of the setup was taken as a fitting parameter.

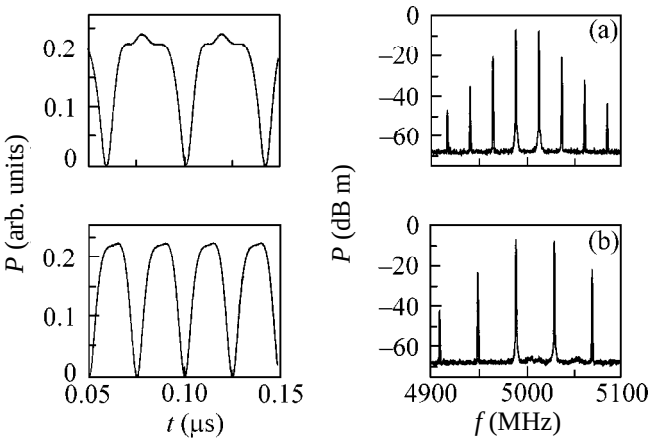

Fig. 3. Microwave signal envelope at the output of the setup (left) and the corresponding frequency spectra (right) for different detunings Δf between the input signals: (a) Δf = 24 MHz; (b) Δf = 40 MHz; $P_1 = P_2$ = 20 dB m; the remaining parameters are as in Fig. 2.

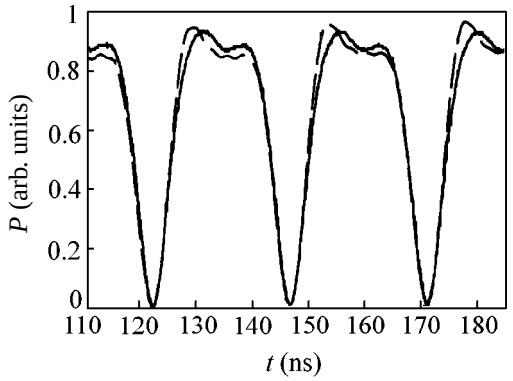

Fig. 4. Comparison of the experimental results with the results of numerical simulation. The solid line is for the experiment, and the dashed line is for the calculation. The computational parameters are the same as in the corresponding experiment: the thickness of the ferromagnetic film L = 13.9 μm; the saturation magnetization is 1750 G; the magnetic loss parameter ΔH = 0.5 Oe; the static magnetic field is 1090 Oe; and the frequencies of input signals are f_1 = 4995 MHz and f_2 = 5036 MHz. The calculations were carried out for the input powers $P_1 = P_2$ = 12 dB m.

The theoretical curve in Fig 4 is obtained for $P_1 = P_2$ = 12 dB m. The corresponding experimental value is $P_1 = P_2$ = 15 dB m, i.e., 3 dB m larger than in the theory. The most probable reason why the microwave power fed into the input of the experimental setup was greater than its calculated value might be the so-called "waveguide effect," as a result of which the excitation of spin waves propagating in ferromagnetic films of a

limited width becomes less efficient. To theoretically describe this effect, one should, strictly speaking, solve the two-dimensional problem of excitation and propagation of spin-wave packets in a film. However, simple estimates show that, for the value obtained by averaging the excited magnetization over the sample width in the presence of the waveguide effect to coincide with the same value in the case of a uniform distribution of magnetization, the input microwave power should be increased approximately twofold [13], which gives the desired 3 dB m. Therefore, the results of numerical simulation nicely explain the experiment.

Let us touch briefly on one more numerical result. The numerical computations suggest that at $P_1 = P_2$ the signal phase undergoes a 180° jump at the zero-amplitude point of each of the generated pulses. The calculations with different input powers bring about nonlinear evolution in the gray solitons undergoing phase jump less than 180°. The resulting modulation depth in the soliton profile is determined by the P_1/P_2 ratio. This phenomenon was also observed in the experiment.

The experimental results and their comparison with theory will be presented elsewhere in more detail.

This work was supported by the Russian Foundation for Basic Research (project no. 99-02-16370), the Deutsche Forschungsgemeinschaft (grant DFG 436 RUS 113/27/0), and the INTAS (grant no. 99-1812).

REFERENCES

1. M. Remoissenet, *Waves Called Solitons: Concepts and Experiments* (Springer-Verlag, Berlin, 1996).
2. *Optical Solitons—Theory and Experiment*, Ed. by J. R. Taylor (Cambridge Univ. Press, Cambridge, 1992).
3. B. A. Kalinikos, N. G. Kovshikov, and A. N. Slavin, Zh. Éksp. Teor. Fiz. **94** (2), 159 (1983) [Sov. Phys. JETP **67**, 303 (1983)].
4. M. Chen, M. A. Tsankov, J. M. Nash, and C. E. Patton, Phys. Rev. B **49**, 12773 (1994).
5. J. W. Boyle, S. A. Nikitov, A. D. Boardman, *et al.*, Phys. Rev. B **53**, 12173 (1996).
6. B. A. Kalinikos, N. G. Kovshikov, and C. E. Patton, Pis'ma Zh. Éksp. Teor. Fiz. **68**, 229 (1998) [JETP Lett. **68**, 243 (1998)].
7. Yu. S. Kivshar and B. Luther-Davies, *Dark Optical Solitons* (Phys. Rep., 1997).
8. M. Chen, M. A. Tsankov, J. M. Nash, and C. E. Patton, Phys. Rev. Lett. **70**, 1707 (1993).
9. A. N. Slavin, Yu. S. Kivshar, E. A. Ostrovskaya, and H. Benner, Phys. Rev. Lett. **82**, 2583 (1999).
10. B. A. Kalinikos, M. P. Kostylev, N. V. Kozhus, and A. N. Slavin, J. Phys.: Condens. Matter **2**, 9861 (1990).
11. V. S. L'vov, *Nonlinear Spin Waves* (Nauka, Moscow, 1987).
12. B. A. Kalinikos and M. P. Kostylev, Zh. Tekh. Fiz. **70** (2), 136 (2000) [Tech. Phys. **45**, 277 (2000)].
13. V. F. Dmitriev, B. A. Kalinikos, and N. G. Kovshikov, Zh. Tekh. Fiz. **56**, 2169 (1986) [Sov. Phys. Tech. Phys. **31**, 1300 (1986)].

Translated by V. Sakun

JETP Letters, Vol. 72, No. 4, 2000, p. 217. Translated from Pis'ma v Zhurnal Éksperimental'noĭ i Teoreticheskoĭ Fiziki, Vol. 72, No. 4, 2000, p. 312.

Summaries of the Projects of the Russian Foundation for Basic Research

PACS numbers: 01.30.-y

ATTENTION READERS

The paper of A.N. Nefedov *et al.* "Formation of Liquidlike and Crystalline Structures in Dusty Plasmas" opens a new heading in JETP Letters "Scientific Summaries." Under this heading will be published ordered reviews of a moderate size devoted to the results obtained within the framework of completed projects supported by the Russian Foundation for Basic Research. The editorial board intends to publish 10–12 reviews a year and hopes that this initiative will be supported by the scientific community.

0021-3640/00/7204-0217$20.00

JETP Letters, Vol. 72, No. 4, 2000, pp. 218–226. Translated from Pis'ma v Zhurnal Éksperimental'noĭ i Teoreticheskoĭ Fiziki, Vol. 72, No. 4, 2000, pp. 313–326.

Formation of Liquidlike and Crystalline Structures in Dusty Plasmas

A. P. Nefedov, O. F. Petrov, V. I. Molotkov, and V. E. Fortov

Institute for High Energy Densities, Russian Academy of Sciences, Izhorskaya ul. 13/19, Moscow, 127412 Russia

Received June 29, 2000

Under certain conditions in a dusty plasma, which is a low-temperature plasma with dust grains, the strong interaction between grains can give rise to gas–liquid–solid-state phase transitions. A study is made of ordered (liquidlike and crystalline) grain structures in various kinds of dusty plasmas: a thermal plasma at atmospheric pressure, a plasma of a dc glow discharge, and a UV radiation–driven plasma. The results of experimental observations of ordered dust structures are reported, and the characteristic features of the dust structures and the conditions for their appearance are discussed. © *2000 MAIK "Nauka/Interperiodica".*

PACS numbers: 52.25.Zb; 52.80.Hc; 64.70.-p

1. INTRODUCTION

The grains in a dusty plasma can be intrinsically charged either by electron and ion fluxes or as a result of photoemission, thermal emission, and secondary emission of electrons from the grain surface [1, 2]. The grains that emit electrons acquire a positive electric charge, in which case the electron density in a dusty plasma increases. In contrast, the grains that collect electrons acquire a negative charge, so that the electron density decreases.

Since the sizes of dust grains are relatively large (from a few hundredths of a micron to several tens of microns), the grains may acquire a very large charge Z_d (about $\sim 10^2$–10^5 elementary charges). As a result, the mean energy of the Coulomb interaction between grains, which is proportional to Z_d^2, can be much higher than the grain thermal energy; this circumstance reflects the highly nonideal nature of a dusty plasma, in which the charged grains play the role of multiply charged heavy ions [3]. Theoretical calculations of the equilibrium properties of such a plasma show that, under certain conditions, the strong electrostatic interaction between grains and the low energy of the grain thermal motion give rise to both gas–liquid–solid-state phase transitions and the formation of ordered spatial structures analogous to those in liquids or solids. In these processes, the electron and ion components behave as ideal gases, as in a Debye plasma. In contrast to conventional solids and atomic liquids, individual dust grains are large enough to efficiently scatter light and to be recorded by a video camera or even to be observed visually. Crystalline structures formed by charged grains in dusty plasmas are called Coulomb or plasma crystals [4].

The interaction between dust grains is traditionally described by the one-component plasma (OCP) model or by the model with a screened (Debye) potential [3, 4], which is also known as the Yukawa model. These models, which assume a classical quasineutral unbounded plasma, make it possible to describe phase transitions by numerically calculating the critical values of the Coulomb coupling parameter $\Gamma = (Z_d e)^2/\bar{r}kT_g$, where T_g is the plasma temperature, $\bar{r} = (4\pi n_d/3)^{-1/3}$ is the mean distance between the grains, and n_d is the grain number density.

In the OCP model, the dusty plasma is treated as an idealized system of ions against the uniform background of neutralizing dust grains, so that, on the whole, the plasma is electrically neutral. The interaction between grains is described by the Coulomb potential $U(r)$, and three-dimensional regular crystalline structures form when the parameter Γ is above the critical value $\Gamma_c = 171$. For small Γ values ($\Gamma < 4$), the plasma is in a "gaseous" state [2–4]. In the Yukawa model, the grain charge is assumed to be screened by plasma electrons and ions, in which case the interaction between grains is described by the Debye–Hückel potential. Taking into account the screening effect, which is described by the ratio $\kappa = \bar{r}/r_D$ (where r_D is the Debye radius), makes it possible to introduce the parameter $\Gamma_s = (Z_d e)^2 \exp(-\bar{r}/r_D)/\bar{r}\,kT_g = \Gamma \exp(-\bar{r}/r_D)$. As a result, in the Yukawa model, the plasma thermodynamics and, accordingly, the conditions for phase transitions, are described by the two parameters: Γ and κ. In the limit $\bar{r}/r_D \longrightarrow 0$, the Yukawa model passes over to the OCP model; and, in the limit $\bar{r}/r_D \longrightarrow \infty$, it passes over to the solid-sphere model.

In early experiments, crystalline structures were observed in plasmas with iron and aluminum micron-sized charged grains confined by alternating and static electric fields. More recently (see, e.g., [5, 6]), results

have been reported on the Coulomb crystallization of dust grains in a weakly ionized plasma of low-pressure RF discharges. In such plasmas, the electron energy is about several electron volts and the ion energy is close to the thermal energy of atoms (about 0.03 eV) [7].

In the absence of emission processes, the grains acquire a negative charge. This effect is attributed to the fluxes of background electron and ions onto the grain surface. It is generally assumed that the electron flux onto the grain surface is absorbed by the grain, while the incident ions knock the electrons out of the grain surface and recombine. Since the electrons are much more mobile than the ions, the electron fluxes are far more intense than the ion fluxes, so that the grains begin to be charged negatively, thereby repulsing the electrons and attracting the ions more and more efficiently. The grains continue to acquire a negative charge until the electron and ion fluxes onto the grain surface become equal to one another.

In experiments on RF discharges, the dust grains acquire a fairly large negative charge (about 10^4–10^5 electron charges), in which case a cloud of dust grains forms near the solid (electrode) surface with a negative potential, in the region where the gravitational and electrostatic forces are in equilibrium. A cloud several centimeters in diameter may contain several tens of horizontal layers of dust grains, the distance between the grains in the layers being several hundred microns.

In more recent experiments, attempts have been made to produce three-dimensional extended ordered structures in the bulk of a quasineutral dusty plasma (rather than in region near the electrode). The grains that formed these structures were charged via various mechanisms, in particular, photoemission and thermal emission. Thus, liquidlike ordered structures were observed to appear in a quasineutral thermal plasma with a temperature of about 1700 K at atmospheric pressure, and three-dimensional crystalline structures were produced in the positive column of a dc glow discharge. The formation of ordered structures in a plasma consisting of dust grains charged by UV radiation was also studied in microgravity experiments carried out aboard the Mir space station.

2. ORDERED DUST STRUCTURES IN A THERMAL PLASMA

Our experiments were carried out with low-temperature thermal atmospheric-pressure plasma flows in which the temperatures of the electrons, ions, and neutral particles were equal to each other and which contained suspended cerium dioxide (CeO_2) grains. The plasma temperature was varied in the range 1700–2200 K (atmospheric pressure) [8, 9]. The distinguishing feature of cerium dioxide is that its work function for emission of thermal electrons is low (~2.75 eV). As a result, the dust grains were charged not only by background electron and ion fluxes, but also via thermionic emission, which may give rise to a positive grain charge. In the course of experiments, the electron density varied from 10^9 to 10^{11} cm^{-3}.

Our measurements provided information about such plasma parameters as the densities of the electrons and positive ions, the plasma temperature, the dust density, and the mean diameter of the grains. The spatial dust structures were analyzed using the pair correlation function $g(r)$, which is defined as the probability for a grain to occur at a distance r from the test grain and, accordingly, characterizes the relative spatial positions of the grains, i.e., shows whether the grains form stochastic (liquidlike) or regular (crystalline) ordered structures. The correlation function in the plasma flow was measured with a time-of-flight laser counter based on the phenomenon of the scattering of a focused laser beam by individual dust grains moving through the measurement region. The radiation scattered by individual grains as they traversed the laser beam was collected by an objective and fed to a photodetector. The received pulsed signals were then processed in order to calculate the pair correlation function.

The results of measuring spatial dust structures were compared with the experimental data obtained for an air jet with CeO_2 grains at room temperature. Such a flow models a "gaseous" plasma, i.e., a plasma with a random (stochastic) spatial distribution of the dust grains.

Figure 1 shows representative pair correlation functions $g(r)$ for CeO_2 grains in an air jet at room temperature and in a thermal plasma. It is seen that the correlation functions for dust grains with the density $n_d = 2.0 \times 10^6$ cm^{-3} in an air jet (Fig. 1a) and in a thermal plasma with the temperature $T_g = 2170$ K (Fig. 1b) are essentially the same. Thus, we can conclude that, in this case, the interaction between grains in a thermal plasma is weak and ordered dust structures cannot form.

According to Fig. 1c, in a thermal plasma with a lower temperature ($T_g = 1700$ K) and higher grain density ($n_d = 5.0 \times 10^7$ cm^{-3}), the correlation function has the form characteristic of a liquidlike structure. In such a plasma, the ion density ($n_i \sim 10^9$ cm^{-3}) is about one order of magnitude lower than the electron density ($n_e \sim 5 \times 10^{10}$ cm^{-3}). The grain charge evaluated from the quasineutrality condition is positive and equals 10^3e. The experimentally obtained parameter values $\Gamma > 120$ and $\kappa = 1.6$ indicate a strong interaction between grains, thereby evidencing the appearance of liquidlike dust structures. That the experimentally observed structures were relatively slightly ordered (see Fig. 1c) is attributed to the finite plasma lifetime (about 7 ms), which is too short for the ordered structure to form completely.

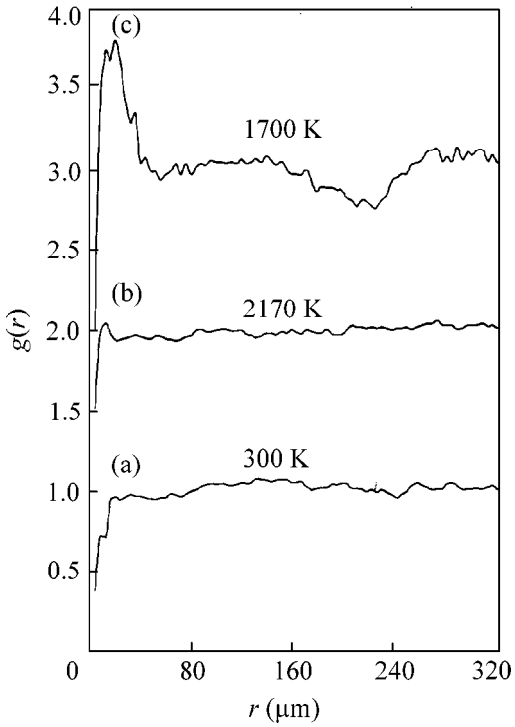

Fig. 1. Pair correlation function $g(r)$ for CeO_2 grains with the charge $Z_d = 500$ in an air jet at room temperature ($T_g \approx$ 300 K) and in plasmas with the temperatures $T_g = 2170$ and 1700 K.

3. MODELING OF THE DYNAMICS OF THE FORMATION OF ORDERED DUST STRUCTURES IN A THERMAL PLASMA

In order to interpret the experimental results, we numerically simulated the dynamics of the formation of ordered dust structures in a thermal plasma. We begin by analyzing the main physical processes that govern the formation of such structures. In our experiments, when stochastically distributed neutral dust particles enter the plasma, they are heated to the temperature of the surrounding gas, acquire an electric charge, and start to interact with each other. The simplest estimate for the thermalization time is

$$\tau_{th} = \left[\pi a^2 n_n \sqrt{\frac{8kT}{\pi m_n}} \frac{2m_n}{m_d}\right]^{-1}, \quad (1)$$

where m_n and n_n are the mass and density of the gas molecules and a and m_d are the radius and mass of a dust grain.

Under our experimental conditions (see table), the thermalization time $\tau_{th} \approx 5 \times 10^{-6}$ s is far shorter than the plasma lifetime $t_{ft} \sim 7$ ms; consequently, we can assume that the dust grains are heated practically instantaneously. This assumption is also justified by the results of investigating the grain dynamics by the correlation spectroscopy technique. Spectroscopy measurements indicate that the dust plasma component is in equilibrium with the surrounding gas (in which case we can also neglect anomalous heating of grains in a gas-discharge plasma).

The formation of ordered dust structures in a thermal plasma was modeled using the methods of molecular dynamics. For each dust grain, we solved the two-dimensional equation of motion

$$m_d \frac{d^2\mathbf{r}_k}{dt^2} = \sum_{j \neq k} \mathbf{\Phi}(r)\Big|_{r = |\mathbf{r}_k - \mathbf{r}_j|} \frac{\mathbf{r}_k - \mathbf{r}_j}{|\mathbf{r}_k - \mathbf{r}_j|} - m_d \nu_{dn} \frac{d\mathbf{r}_k}{dt} + \mathbf{F}_{br}. \quad (2)$$

into which we incorporated the interaction between grains; the friction force of the grain on the neutral gas particles; and the random (Brownian) force $\mathbf{F}_{br}$, which results from the impacts of the molecules of the surrounding gas. Under the assumption that the interaction between grains is described by the Debye potential, the force $\mathbf{\Phi}(r)$ can be written as

$$\mathbf{\Phi}(r) = -Z_d e \frac{\partial \varphi_D}{\partial r^2} = \frac{Z_d^2 e^2}{r^2}\left[1 + \frac{r}{\lambda_D}\right]\exp\left(-\frac{r}{\lambda_D}\right). \quad (3)$$

Parameter values used to simulate the formation of ordered dust structures in a thermal plasma

Parameter	Value	Parameter	Value
Plasma temperature	$T = 1700$ K	Grain charge	$Z_d = 500$
Neutral gas pressure	$P_n = 1$ atm	Mean intergrain distance	$l = 17$ μm
Electron plasma density	$n_e = 7 \times 10^{10}$ cm^{-3}	Screening length	$\lambda_D = 11$ μm
Ion plasma density	$n_i = 4 \times 10^{10}$ cm^{-3}	Dust–neutral-gas friction rate	$\nu_{dn} = 9.6 \times 10^4$ s^{-1}
Dust density	$n_d = 5 \times 10^7$ cm^{-3}	Coupling parameter	$\Gamma = 90$
Grain radius	$a = 0.4$ μm	Parameter κ	$\kappa = 2.5$
Grain mass	$m_d = 1.6 \times 10^{-12}$ g	Coupling parameter with allowance for screening	$\Gamma_s = 8$

The table lists the model parameters, which are close to those of our experiments. Now, we turn to the main simulation results. We found that, by the end of the relaxation process, the system evolves into a well-ordered state, which can be formally referred to as a liquidlike state. Figure 2 illustrates the evolution of the pair correlation function $g(r)$ calculated from the instantaneous positions of the grains. The profiles in Fig. 2e were evaluated by averaging the function $g(r)$ over time; the averaging procedure is justified, because, during the time interval $40 < t < 70$ ms, the system evolves into a steady state and the pair correlation function remains essentially unchanged. For comparison, Fig. 2 shows the correlation function that was obtained directly from experiments and corresponds to Fig. 1c.

Analyzing Fig. 2, we can qualitatively describe how the ordered dust structures form. First, the grains that occur at short distances from each other start to fly apart; as a result, a region arises in which the pair correlation function vanishes (Figs. 2a, 2b). This process is very fast, because the repulsive forces between the grains increase sharply as the distance between them decreases. Then, a pronounced first peak appears in the profile of the pair correlation function (Fig. 2c). As time elapses, the first peak becomes higher; this process is accompanied by the appearance of additional peaks (Fig. 2d). The steady-state correlation function (Fig. 2e) is characterized by several pronounced peaks. Such a function is typical of a closely ordered system. It is for this reason that the final state of the system was called a liquidlike state.

The time required for an ordered structure to form can be defined rather arbitrarily, depending on the correlation scale length in which we are interested. The larger the distance, the longer the time required for the pair correlation function at this distance to relax to the final state. Thus, in the case under analysis, the first three peaks appear in the profile of the correlation function on a time scale of about $t_f \approx 35$ ms. We can also introduce the time t_1 needed for the formation of the first peak in the pair correlation function. Physically, this is the time scale on which any short-scale correlation in the system comes into play. For the parameter values at hand, numerical calculations give $t_1 \approx 5$ ms.

A distinctive feature of our experiments is the finite plasma lifetime $t_{ft} \approx 7$ ms. According to our simulation results, this indicates that the formation of ordered dust structures revealed in the experiments was in progress; consequently, we experimentally determined unsteady pair correlation functions. Nevertheless, the plasma lifetime was long enough for short-scale correlations to come into play.

Figure 2 enables us to compare the pair correlation function obtained experimentally with the functions calculated numerically. We point out the following two circumstances. First, the experimental correlation function was found to have only one peak, which agrees well with the simulation results. In fact, Fig. 2d indicates that, at $t = 7$ ms, the first peak in the experimental function is already close to its final shape, while the higher order peaks are only beginning to form. The presence of only one peak provides conclusive evidence that the plasma lifetime is insufficiently long for an ordered structure to form completely. Second, the first peak in the experimental correlation function is far wider (by a factor of approximately five) than that in the function calculated numerically. This discrepancy may in principle be attributed to the specific features of the measurement technique using a time-of-flight laser counter [8, 9].

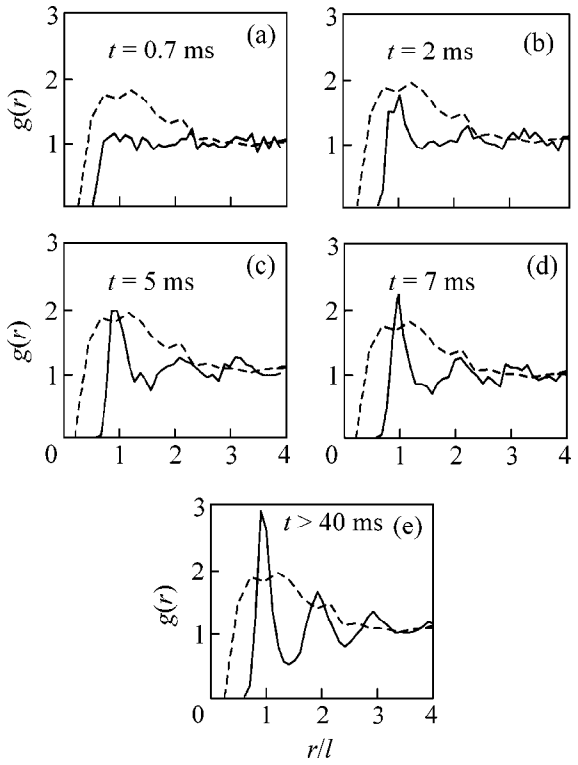

Fig. 2. Evolution of the pair correlation function. The solid curves plot the profiles calculated numerically at the times t = (a) 0.7, (b) 2, (c) 5, (d) 7, and (e) 40 ms. The dashed curves are for the experimentally obtained profile.

4. THREE-DIMENSIONAL CRYSTALLINE DUST STRUCTURES IN A DC GLOW DISCHARGE

In contrast to the thermal plasma, the plasma of a low-pressure glow discharge in a gas at room temperature is nonisothermal. We carried out a series of experiments with dc glow discharges in neon over the pressure range from fractions of a torr to several torr and for discharge currents from fractions of a milliampere to several milliamperes.

We observed ordered dust structures in the positive column of a glow discharge with standing strata—immobile dark regions alternating with bright zones with nonuniform luminosity, the characteristic spatial

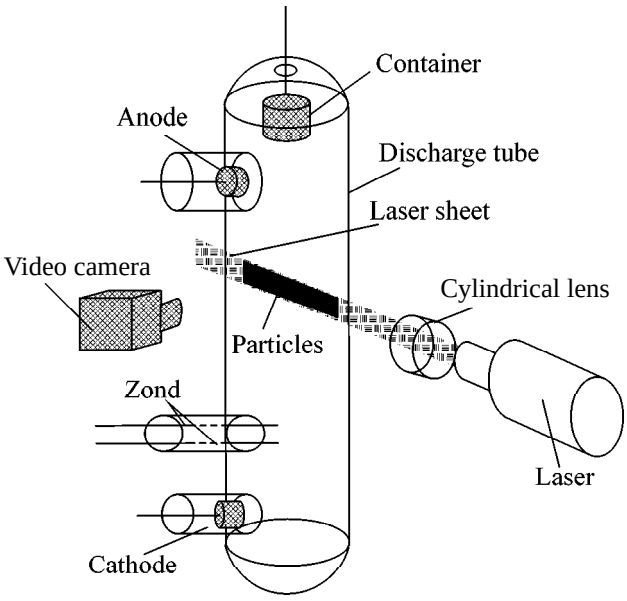

Fig. 3. Layout of the experimental device for studying ordered dust structures in a gas-discharge plasma.

scale of the strata being about several centimeters [10]. The electric field is relatively strong in the head of a stratum (i.e., in its bright part) and is weak outside the head. The floating potential of the discharge-tube wall is high. As a result, the head of each stratum acts as an electrostatic well capable of trapping highly dispersed grains in the positive column of a glow discharge in a vertically oriented tube, in which case the strong radial electric field does not allow the grains to escape from the well and reach the tube wall.

A schematic of the experimental device is shown in Fig. 3. The grains irradiated by a vertical or horizontal laser beam were recorded by a video camera (some of the grains were even observed visually). The formation of ordered structures can be described as follows. Micron-sized grains falling from the container into a glass tube enter the discharge plasma from above and acquire an electric charge when moving through the plasma. After the charged grains have fallen below their equilibrium positions, they stop falling down and move upward for several seconds; then, they form an ordered structure, which remains unchanged for an arbitrarily long time (as long as the discharge parameters remain unchanged) [11]. Experiments on the formation of ordered dust structures in the positive column of a glow discharge were carried out with several kinds of grains: grains in the form of hollow borosilicate glass microspheres 50–60 μm in diameter, polydisperse Al_2O_3 grains 3–5 μm in size, and monodisperse melamine-formaldehyde grains 1.87 μm in diameter.

The grains were seen to form a cloud at the center of a stratum. As a rule, we observed several clouds simultaneously in the neighboring strata. Glass microspheres formed clouds 5–10 mm in diameter, and the diameter of the clouds of Al_2O_3 grains amounted to 20 mm. A cloud of glass microspheres consisted of 10–20 plane horizontal layers; the number of layers in a cloud of Al_2O_3 grains was even larger. In the vertical direction, the grains in a cloud built chains. The distance between the vertical chains was 250–400 μm; and the distance between the grains in the horizontal direction was 350–600 μm, so that the grain density was about $n_d \sim 10^3$–10^4 cm^{-3} [12].

Figure 4a displays a portion of the horizontal cross section of a dust crystal formed by 1.87-μm-diameter monodisperse melamine-formaldehyde grains in a discharge plasma in a neon–hydrogen mixture at a pressure of 0.8 torr, the discharge current being 1.1 mA. The shape of the pair correlation function $g(r)$ for this ordered structure (see Fig. 4b) provides evidence for long-scale correlations between the grains, thereby indicating the crystalline nature of the structure.

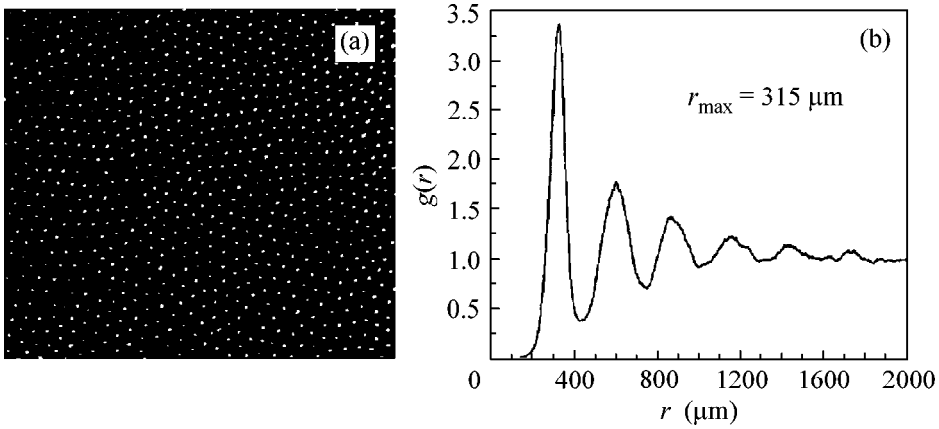

Fig. 4. (a) Image of a horizontal cross section of an ordered dust structure in a stratum of the positive column of a glow discharge and (b) pair correlation function for this structure.

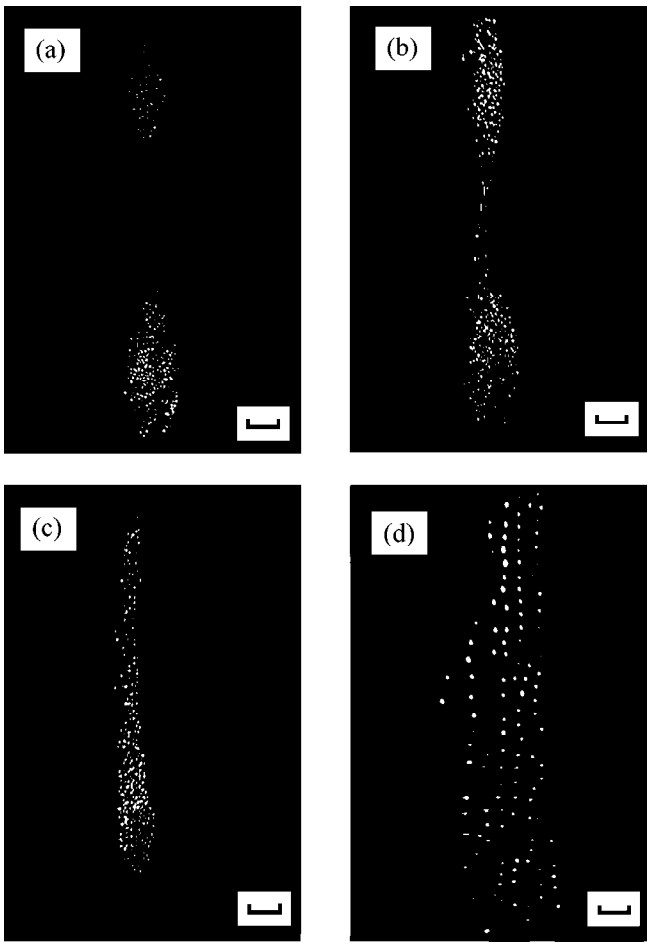

Fig. 5. Images of glass microspheres in a vertical cross section at different discharge currents and plasma pressures: (a) 0.5 mA and 0.47 torr, (b) 0.5 mA and 0.44 torr, and (c) 0.4 mA and 0.37 torr. Figure 5d is a magnified image of a part of the cylindrical structure shown in Fig. 5c. The scale in images (a)–(c) is 3 mm, and the scale in the magnified image (d) is 1 mm.

Varying the parameters of the discharge plasma (the plasma pressure and discharge current) made it possible to change the shape of a dust cloud. Thus, from Figs. 5a–5c, we can see that, as the discharge current and plasma pressure decrease, two neighboring elliptically shaped clouds merge into a cylindrical ordered dust structure, which extends to several tens of centimeters in the vertical direction. Figure 5d presents a magnified image of a part of the cylindrical structure.

On increasing the discharge current, we observed the evolution of crystalline structures, first, into liquidlike structures and, then, into gaseous structures. In a sense, we may speak of the "melting" of dust crystals. Thus, for Al_2O_3 grains at a plasma pressure of 0.3 torr and a discharge current of 0.4 mA (Fig. 6a), the correlation function has four pronounced peaks (Fig. 7a), thereby providing evidence for long-scale correlations between the grains and, accordingly, for the crystalline nature of the ordered structure. When the discharge current is increased by almost one order of magnitude (to 3.9 mA, see Fig. 6b), the shape of the correlation function implies the existence of only short-scale correlations between the grains; this indicates that the dust crystal "melts" and "evolves" into a liquidlike structure (Fig. 7b). We emphasize that, during this "phase transition," the distance between the grains (250 μm) remains almost unchanged [13].

Under certain conditions, we observed the effect of anomalous heating of the dust component in dc glow discharges, in which case the grains acquired very high energies (up to 50 eV). This effect can be explained as being due to the melting of dust crystals, which was observed when the plasma parameters changed. Under certain discharge conditions, increasing the number of small-sized grains gives rise to composite dust structures: in some regions, the grains are highly ordered (plasma crystals), and, in other regions, they experience convective and oscillatory motions (dust–plasma liquid) [14]. Most of the central region of the composite

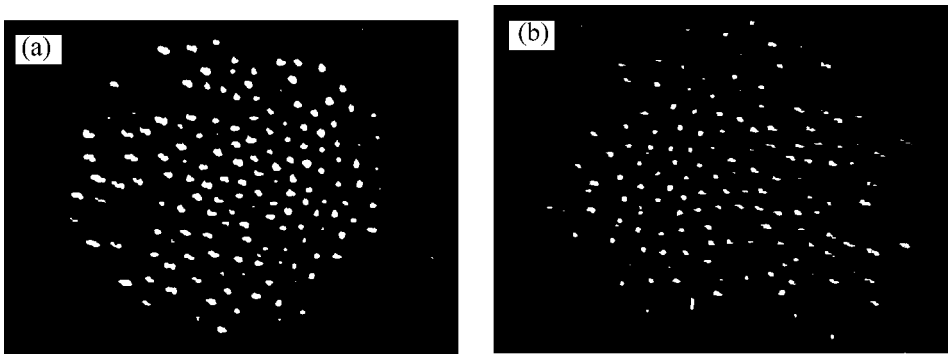

Fig. 6. Images of Al_2O_3 grains in a vertical cross section for a plasma pressure of 0.3 torr at different discharge currents: (a) 0.4 and (b) 3.85 mA. The scale is 1 mm.

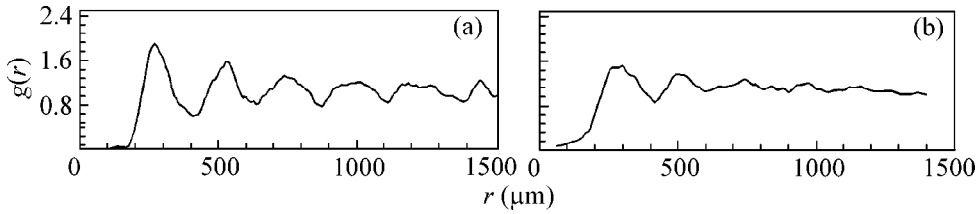

Fig. 7. Pair correlation function for Al_2O_3 grains in a vertical cross section at a neon pressure of 0.3 torr and discharge currents of (a) 0.4 and (b) 3.85 mA.

structure is occupied by a highly ordered dust–plasma crystal with a pronounced chainlike configuration of the grains. In the upper region of the structure, the grains experience convective motion, whose intensity decreases toward the center of the structure. In the lower region, the grains are observed to oscillate in the vertical direction (grain density waves) at a frequency of about 10 Hz and a wavelength of about 1 mm, the mean intergrain distance being 200 μm (Fig. 8). Such self-excited oscillations can be driven by the instability of dust acoustic waves; the nature of this instability requires a separate study [15].

Let us estimate the grain parameters under conditions typical of glow discharges: the electron thermal energy is $kT_e \sim 3$ eV, the ion thermal energy is 0.03 eV, and the electron density is approximately 10^9 cm^{-3}. In a glow discharge in neon, the floating potential of the grains amounts to $V_d \sim (kT_e/e) \sim 3$ V. The grain charge can be found from the relationship $Z_d = aV_d$. Consequently, the charge of glass microspheres 50–60 μm in size is estimated to be ~10^5 e.

The grain charge can also be deduced from the balance between the gravitational and electrostatic forces in a stratum, $Z_d = m_d g/eE_s$. At $E_s \sim 10$ V/cm, the charge of glass microspheres with the mass $m_d \sim 10^{-8}$ g is estimated to be $Z_d \sim 10^6$ e. This estimate is about one order of magnitude larger than what we have just obtained for typical discharge parameters. This discrepancy can be explained by noting that, in the region occupied by the stratum, there is a second peak (at 15 eV) in the profile of the electron energy distribution function, so that, inside the stratum, the grains acquire a negative charge until the grain floating potential becomes as high as $V_d \sim (kT_e/e) \sim 15$–30 V, which corresponds to the floating potential of the discharge-tube wall. As a result, the

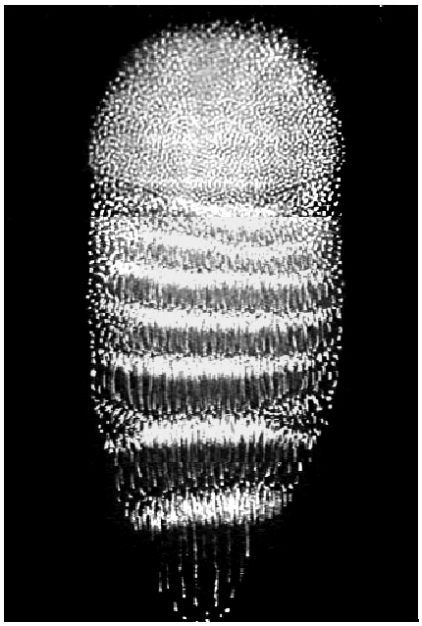

Fig. 8. Image of an ordered dust structure of monodisperse grains 1.87 μm in diameter at a discharge current of 5 mA and a plasma pressure of 0.3 torr. The vertical dimension of the frame is 10.6 mm.

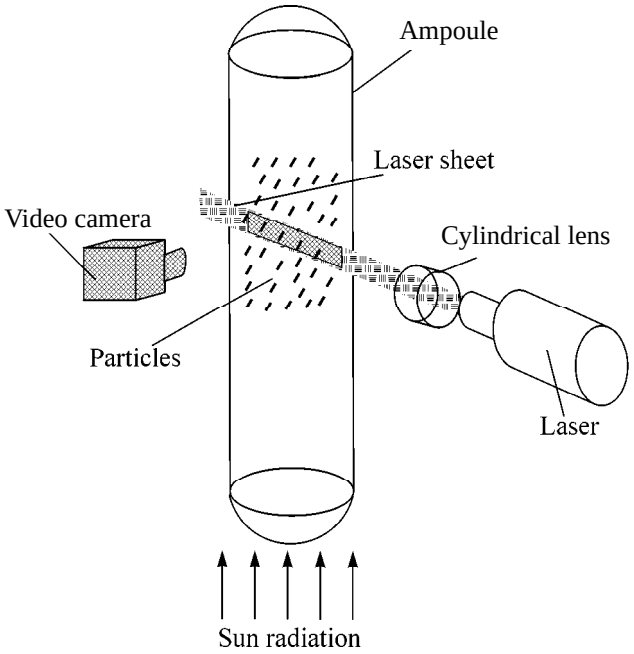

Fig. 9. Layout of the experimental device in space experiments.

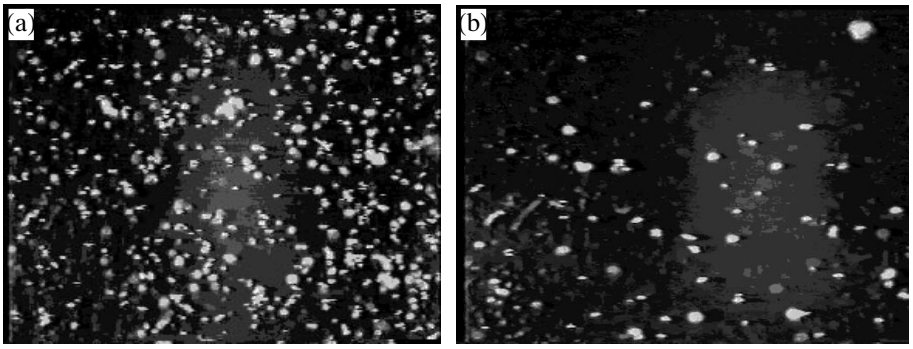

Fig. 10. Sequence of states of an ensemble of bronze grains in an ampoule at a pressure of 40 torr (a) 20 and (b) 110 s after shaking the ampoule.

charges of glass microspheres and Al_2O_3 grains are approximately equal to ~10^6 and 10^5 *e*, respectively.

5. PLASMA DRIVEN BY UV RADIATION UNDER MICROGRAVITY CONDITIONS

A dusty plasma with positively charged grains can also be produced by irradiating the neutral grains in a buffer gas by a flux of photons with energy above the work function for photoelectronic emission from the grain surface. The conditions in such a plasma may be favorable for the appearance of ordered crystalline structures. Since, for most substances, the characteristic work function for photoelectronic emission is lower than 6 eV, the fluxes of photons with energies lower than, or on the order of, 12 eV can be used to charge the grains positively without ionizing the buffer gas (such as helium and argon).

Ordered structures of the grains charged by solar radiation have been studied in microgravity experiments aboard the Mir space station [16]. Investigation of the formation of ordered dust structures in such experiments provided fundamentally new information that cannot be obtained under terrestrial conditions. Note also that intense fluxes of UV radiation in space can charge dust grains via photoemission, in which case, grains several microns in size acquire a positive charge of about ~10^2–10^4 *e*.

Space experiments were performed with glass ampoules filled with neon at different pressures (0.01 and 40 torr) and containing spherical bronze grains coated with cesium (Fig. 9). Before the experiment, the ampoule was placed in front of the window of the Mir station. The grains were irradiated by a planar laser beam ("laser sheet") with a width less than 200 μm and were recorded by a video camera.

Since the grains were deposited on the ampoule wall, the experiments were carried out as follows: first, the ampoule underwent an external dynamic action (it was shaken up); then, the grains relaxed to the initial state (they were again deposited on the wall). Figure 10 illustrates the evolution of an ensemble of grains in an ampoule at a pressure of 40 torr under the action of solar radiation. Experimental observations revealed that, initially, the grains moved in a random fashion. Then, the grain motion usually became ordered; at a high pressure, the grain motion along certain trajectories in an ampoule was found to be more intense. In some experiments, the grains were observed to experience not only translational, but also oscillatory motion. When processing the measured data on grain trajectories, the grain velocity was found to vary periodically in all the experiments. Such velocity variations may be attributed either to the fluctuations of the grain charge or to the dynamic action of microaccelerations aboard the Mir space station.

Experiments on the Mir station revealed another interesting effect—the formation of agglomerates in which the number of grains varied from three or four to several hundred and which could be detached from the ampoule wall by slightly shaking up the ampoule. The agglomerates primarily appeared several seconds after the ampoule was shaken up, and thereafter they decayed under the action of solar radiation. Presumably, the agglomeration of grains in the ampoule is explained by the fact that, in the initial stage of irradiation, some of the grains were charged positively (via photoelectronic emission) and others were charged negatively (by the fluxes of the emitted electrons).

According to the estimates obtained when analyzing the grain dynamics, the grains may acquire a charge as large as several units of 10^4 elementary charges, the coupling parameter being $\Gamma \sim 10^4$. Although the grain charge and coupling parameter were both large, no strong correlations among the grains were observed: the grains formed only liquidlike structures.

6. CONCLUSION

Our experimental study of strongly interacting dust grains in a thermal plasma at atmospheric pressure and in the positive column of a dc glow discharge demonstrates the possibility of the formation of ordered dust structures (including crystalline structures) in dusty

plasmas with specific parameters (e.g., in a thermal plasma, which characteristically occupies a fairly large region and in which the dust structures are essentially three-dimensional). The ordered dust structures appear in a quasineutral plasma region rather than in an electrode sheath. That the experimental pair correlation function has only one maximum is explained by the finite lifetime of the thermal plasma: the correlation function was measured over the time interval during which the formation of an ordered structure was still in progress.

In a stratum of a dc glow discharge, we observed various kinds of ordered structures of micron-sized grains: from liquidlike structures with short-scale correlations, to crystalline structures (dust–plasma crystals) with long-scale correlations. The ordered structures differ in shape; in the inner region of the structure, the grains can experience convective motion.

A comparative analysis of the results from experimental and theoretical studies of an ensemble of dust grains charged by solar radiation via photoemission under microgravity conditions confirm the conclusion that the grains may form extended liquidlike ordered structures even in a plasma in which the agglomeration processes are very intense.

The results of our investigations may have some important applications. Ordered structures in dusty plasmas can be successfully used to solve both theoretical and practical problems. One of the most important theoretical problems in plasma physics is that of studying strongly nonideal multicomponent plasmas. The results of experiments with crystalline dust structures can be conveniently used to develop and validate analytic models of such plasmas. It is also important to investigate the lattice dislocations in crystals, the thermodynamics of crystal lattices having dislocations and dislocation-free lattices, the interaction of laser light with crystals, oscillations and waves in ordered structures, and related resonance phenomena. In solid state physics, the results of these investigations can be used to model atomic and molecular crystals. In the physics of critical phenomena, the study of phase transitions in dusty plasmas can provide new insights into the condensation processes. The possibility of creating small systems consisting of several dust grains and an analysis of their stochastic motion and their response to external fields can be very useful for investigating the dynamic processes in such systems.

Among microelectronics-related applications, we can mention the problem of removing particles in manufacturing integrated circuits and the problem of modeling small crystals (nanocrystals) in studying plasma methods for film deposition. Commercial applications of our results may include the following issues: the creation of coatings through the UV radiation–controlled deposition of grains suspended in a plasma onto a substrate for the purpose of fabricating new artificial materials with the desired properties (including porous and composite materials), the production of granules with multilayer coatings from substances with different properties, etc.

This work was supported in part by the Russian Foundation for Basic Research, project nos. 95-02-06456, 97-02-17565, and 98-02-16828.

REFERENCES

1. M. S. Sodha and S. Guha, Adv. Plasma Phys. **4**, 219 (1971).
2. V. E. Fortov and I. T. Yakubov, *Nonideal Plasma* (Énergoatomizdat, Moscow, 1994).
3. S. Ichimaru, Rev. Mod. Phys. **54**, 1017 (1982).
4. H. Ikezi, Phys. Fluids **29**, 1764 (1986).
5. J. H. Chu and Lin I, Phys. Rev. Lett. **72**, 4009 (1994).
6. H. Thomas, G. E. Morfill, V. Demmel, *et al.*, Phys. Rev. Lett. **73**, 652 (1994).
7. Yu. P. Raĭzer, M. N. Shneĭder, and N. A. Yatsenko, *High-Frequency Capacitive Discharge* (Nauka, Moscow, 1995).
8. V. E. Fortov, A. P. Nefedov, O. F. Petrov, *et al.*, Pis'ma Zh. Éksp. Teor. Fiz. **63**, 176 (1996) [JETP Lett. **63**, 187 (1996)].
9. V. E. Fortov, A. P. Nefedov, O. F. Petrov, *et al.*, Phys. Rev. E **54**, R2236 (1996).
10. Yu. P. Raizer, *Gas Discharge Physics* (Nauka, Moscow, 1987; Springer-Verlag, Berlin, 1991).
11. V. E. Fortov, A. P. Nefedov, V. M. Torchinskiĭ, *et al.*, Pis'ma Zh. Éksp. Teor. Fiz. **64**, 86 (1996) [JETP Lett. **64**, 92 (1996)].
12. V. E. Fortov, A. P. Nefedov, V. M. Torchinsky, *et al.*, Phys. Lett. A **229**, 317 (1997).
13. A. P. Nefedov, O. F. Petrov, and V. E. Fortov, Usp. Fiz. Nauk **167**, 1215 (1997) [Phys. Usp. **40**, 1163 (1997)].
14. V. E. Fortov, V. I. Molotkov, A. P. Nefedov, and O. F. Petrov, Phys. Plasmas **6**, 1759 (1999).
15. V. I. Molotkov, A. P. Nefedov, V. M. Torchinskiĭ, *et al.*, Zh. Éksp. Teor. Fiz. **116**, 902 (1999) [JETP **89**, 477 (1999)].
16. V. E. Fortov, A. P. Nefedov, O. S. Vaulina, *et al.*, Zh. Éksp. Teor. Fiz. **114**, 2004 (1998) [JETP **87**, 1087 (1998)].

Translated by O. Khadin